

FROM THE INSIDE OUT

COLLOIDAL CDSE/CDS SEMICONDUCTOR NANORODS: A STUDY ON THE
INFLUENCE OF THEIR STRUCTURES, SURFACE LIGANDS, AND INTERACTIONS
WITH REDOX-ACTIVE (POLY)DOPAMINE

DISSERTATION

ZUR ERLANGUNG DES AKADEMISCHEN GRADES

DOCTOR RERUM NATURALIUM (DR. RER. NAT)

VORGELEGT DEM RAT DER CHEMISCH-
GEOWISSENSCHAFTLICHEN FAKULTÄT DER FRIEDRICH-
SCHILLER-UNIVERSITÄT JENA

VON MASTER OF SCIENCE BEI LIU

GEBOREN AM 09.01.1990 IN HEILONGJIANG, CHINA



FRIEDRICH-SCHILLER-
UNIVERSITÄT
JENA

Gutachter:

1. Prof. Dr. Benjamin Dietzek, Institut für Physikalische Chemie,
Friedrich-Schiller-Universität Jena
2. Prof. Dr. Wolfgang Weigand, Institut für Anorganische und
Analytische Chemie, Friedrich-Schiller-Universität Jena

Tag der öffentlichen Verteidigung: 02. Dec 2020

TABLE OF CONTENT

TABLE OF CONTENT.....	III
LIST OF ABBREVIATIONS.....	V
LIST OF FIGURES AND TABLES.....	VII
CONFERENCE CONTRIBUTIONS & LIST OF PUBLICATIONS.....	XI
CHAPTER 1. INTRODUCTION.....	1
1.1 Motivation.....	1
1.2 A brief introduction to quantum confined semiconductor nanocrystals.....	1
1.3 The quantum confinement effects and bandgap.....	2
1.4 Surface passivation.....	5
1.4.1 Organic Layer Passivation.....	6
1.4.2 Inorganic Layer Passivation.....	6
1.4.3 Non-epitaxial growth.....	9
1.5 A brief introduction to the synthesis of quantum dots and NRs.....	9
1.5.1 Quantum dots (including the core/shell quantum dots).....	9
1.5.2 NRs and the dot-in-rod NRs.....	10
1.6 Quasi-Type II band alignment in CdSe/CdS dot-in-rod NRs and the potential application in hydrogen evolution reaction (HER).....	11
1.7 The outlines of this thesis.....	13
CHAPTER 2. EXPERIMENTAL SECTION.....	15
2.1 Synthesis protocols.....	15
2.1.1 Synthesis of the seeds (CdSe quantum dots).....	15
2.1.2 Synthesis of dot-in-rod TOPO-NRs.....	16
2.1.3 Ligand exchange with 11-mercaptopundecanoic acid (MUA).....	17
2.1.4 Ligand exchange with poly(ethylene glycol) 2-mercaptoethyl methyl ether (HS-PEG-OCH ₃).....	17
2.1.5 Synthesis of and ligand exchange with dihydrolipoic acid–poly(ethylene glycol) ester (DHLA-PEG).....	17
2.1.6 Synthesis of and ligand exchange with dihydrolipoic acid (DHLA).....	19
2.1.7 Ligand exchange with hyperbranched poly(ethylene imine) (PEI).....	19
2.2 Methods and instruments.....	19
2.2.1 Transmission electron microscopy (TEM).....	19
2.2.2 Steady-state absorption and photoluminescence spectroscopy.....	20
2.2.3 Fourier transform infrared spectroscopy (FTIR).....	22
2.2.4 Pump-probe transient absorption spectroscopy.....	23
2.2.5 Time-resolved emission spectroscopy.....	26
CHAPTER 3 CdSe/CdS DOT-IN-ROD AND INSIDE-OUT NRS.....	29
3.1 Characterization of the inside-out structure.....	30

3.2	Steady-state measurements and discussion.....	31
3.1.1	Steady-state absorption measurements and discussion.....	31
3.1.2	Steady-state emission measurements and discussion.....	34
3.2	Transient absorption measurements and discussion.....	37
3.2.1	Transient absorption measurements of the dot-in-rod NRs and discussion.....	37
3.2.2	Transient absorption measurements of the inside-out NRs and discussion.....	40
3.3.3	Further measurements on the inside-out NRs and discussion.....	44
3.3	Conclusion.....	48
CHAPTER 4	THE PHASE TRANSFER OF THE DOT-IN-ROD NRS.....	51
4.1	Characterization of NRs.....	53
4.1.1	The determination of size distribution of TOPO-NRs.....	53
4.1.2	Infrared spectroscopy investigation on NRs and discussion.....	53
4.2	Steady-state measurements on the NRs and discussion.....	61
4.3	pH stability of NRs and discussion.....	66
4.4	Time-resolved investigation on NRs and discussion.....	70
4.4.1	Time-resolved emission lifetime on NRs and discussion.....	70
4.4.2	Transient absorption measurements on NRs and discussion.....	72
4.5	Conclusion.....	75
CHAPTER 5	THE INTERACTION BETWEEN CdSe/CdS DOT-IN-ROD NRS AND DOPAMINE / POLYDOPAMINE.....	77
5.1	The interaction between MUA-NRs with dopamine molecules.....	78
5.2	The interaction between MUA-NRs with polydopamine.....	85
5.3	The interaction between HS-PEG-OCH ₃ -NRs with dopamine molecules.....	89
5.4	Conclusion.....	94
CHAPTER 6	SUMMARY.....	95
CHAPTER 7	ZUSAMMENFASSUNG.....	99
	BIBLIOGRAPHY.....	103
	ACKNOWLEDGEMENT.....	123
	APPENDIX.....	125
	SELBSTSTAENDIGKEITSERKLAERUNG.....	137

LIST OF ABBREVIATIONS

0D	zero-dimensional
1D	one-dimensional
2D	two-dimensional
3D	three-dimensional
ATR	attenuated total reflectance
CB	conduction band
COSY	correlation spectroscopy
DAS	decay associated spectrum
DDC	dicyclohexylcarbodiimide
DHLA	dihydrolipoic acid
DHLA-PEG	dihydrolipoic acid–poly(ethylene glycol) ester
DMAP	4-(dimethylamino)-pyridine
EDS	energy dispersive spectroscopy
EMA	effective mass approximation
FTIR	Fourier transform infrared spectroscopy
HER	hydrogen evolution reaction
¹ H-NMR	proton nuclear magnetic resonance
HS-PEG-OCH ₃	poly(ethylene glycol) 2-mercaptoethyl methyl ether
IR	Infrared Spectroscopy
IRF	instrument response function
LA	lipoic acid
LA-PEG	lipoic acid–poly(ethylene glycol) ester
MAA	mercaptoalkanoic acids
MUA	11-mercaptoundecanoic acid
MWCO	molecular weight cut-off
NRs	nanorods
OD	optical density
ODPA	octadecylphosphonic acid
PBS	phosphate-buffered saline
PEI	poly(ethylene imine)
PL	photoluminescence
PLQY	photoluminescence quantum yield

PMTs	photomultiplier tubes
P-MUA-NRs	polydopamine coated MUA-NRs
PPA	propylphosphonic acid
SD	standard deviation
SHG	second harmonic generation
SILAR	successive ion layer adsorption and reaction
TA	transient absorption
TEM	transmission electron microscopy
TOP	trioctylphosphine
TOPO	tri-n-octyl phosphine oxide
UV	ultraviolet
VB	valence band
Vis	visible

LIST OF FIGURES AND TABLES

In the main text

- Figure 1.1. The electronic structure changes of semiconductor material from its atoms to bulky material, together with its quantum confined nanocrystals
- Figure 1.2. The schematic illustration of surface passivation on a quantum dot by organic ligands and inorganic layer and the energy diagram of the energy difference between the core and shell
- Figure 1.3. Different types of core/shell nanocrystals based on the band alignment
- Figure 1.4. The “hot injection” method of CdSe quantum dots synthesis
- Figure 1.5. The “seeded growth” method of CdSe/CdS dot-in-rod NRs synthesis
- Figure 1.6. Schematic illustration of a triadic nanorod: a CdSe@CdS nanorod with a Pt nanoparticle at one tip
- Figure 1.7. Schematic outline of this thesis’ structure
- Figure 2.1. The synthesis setup of CdSe quantum dots by the “hot-injection” method
- Figure 2.2. The ¹H-NMR spectrum of DHLA-PEG (upper) and LA-PEG (bottom) in CD₂Cl₂
- Figure 2.3. The illustration of the UV-Vis absorption spectrometer setup using a double beam method
- Figure 2.4. The illustration of the photoluminescence spectrometer setup in a 90° geometry
- Figure 2.5. The illustration of the vibration modes in FTIR
- Figure 2.6. The illustration of the FTIR setup in ATR mode
- Figure 2.7. The illustration of the pump probe transient absorption setup
- Figure 2.8. The illustration of the detecting system of the transient absorption setup
- Figure 2.9. The illustration of the time-resolved emission spectroscopy setup
- Figure 2.10. The illustration of the working principle of the streak camera.
- Figure 3.1. Illustration of the dot-in-rod and inside-out NRs with their possible mechanisms of hole removal
- Figure 3.2. The EDS and TEM images of the inside-out NRs
- Figure 3.3. The absorption spectra of the dot-in-rod and inside-out NRs in toluene
- Figure 3.4. The absorption spectra of the dot-in-rod and inside-out NRs in toluene with their 1st and 2nd derivatives
- Figure 3.5. The multi-Gaussian peaks fit of absorption spectra of the dot-in-rod and inside-out NRs
- Figure 3.6. The absorption and emission spectra of the dot-in-rod and inside-out NRs
- Figure 3.7. The multi-Gaussian peaks fit of emission spectra of the dot-in-rod and inside-out NRs in toluene
- Figure 3.8. The energy band diagrams of the dot-in-rod and inside-out NRs
- Figure 3.9. The TA spectral of the dot-in-rod NRs in toluene together with the absorption and emission spectra of the dot-in-rod NRs and the kinetics of CdS and CdSe
- Figure 3.10. The global fit of dot-in-rod NRs kinetics
- Figure 3.11. The TA spectral of the inside-out NRs in toluene together with the absorption and emission spectra of the inside-out NRs and the kinetics of CdS and CdSe
- Figure 3.12. The illustration of the carrier dynamics in the inside-out NRs upon excitation

- Figure 3.13. The global fit of the first TA measurement on the inside-out NRs and the DAS of global fit of CdS and CdSe
- Figure 3.14. The TA spectral of the inside-out NRs of each TA measurement
- Figure 3.15. The absorption spectra of the samples for transient absorption measurements in toluene
- Figure 3.16. The single kinetics of all three times measurements
- Figure 4.1. Chemical structures of the ligands used in this chapter
- Figure 4.2. The TEM images of two batches of TOPO-NRs
- Figure 4.3. The IR spectra of TOPO and TOPO-NRs
- Figure 4.4. The IR spectra of MUA and MUA-NRs
- Figure 4.5. The IR spectra of HS-PEG-OCH₃ and HS-PEG-OCH₃-NRs
- Figure 4.6. The IR spectra of DHLA and DHLA-NRs
- Figure 4.7. The IR spectra of DHLA-PEG and DHLA-PEG-NRs
- Figure 4.8. The IR spectra of PEI and PEI-NRs
- Figure 4.9. Steady-state spectroscopy on NRs #2 capped with different ligands
- Figure 4.10. Gaussian fits of the absorption spectrum of TOPO-NRs
- Figure 4.11. Multi-Gaussian peaks fit of the emission spectra of TOPO-NRs and DHLA-PEG-NRs
- Figure 4.12. The peak position and integral area of the three Gaussian peaks introduced in the multi-Gaussian peaks fit of the emission spectra of NRs with different ligands
- Figure 4.13. The time-lapse absorption spectrum of HS-PEG-OCH₃-NRs in different pH values and the time-lapse emission spectrum of HS-PEG-OCH₃-NRs in the same conditions
- Figure 4.14. The time-lapse absorption spectrum of DHLA-PEG-NRs in different pH values and the time-lapse emission spectrum of DHLA-PEG-NRs in the same conditions
- Figure 4.15. The time-lapse absorption spectrum of PEI-NRs in different pH values and the time-lapse emission spectrum of PEI-NRs in the same conditions
- Figure 4.16. The emission lifetime of NRs with different ligands
- Figure 4.17. The global fit of TOPO-NRs kinetics
- Figure 4.18. The illustration of the influence of surface defects on the carrier dynamics.
- Figure 5.1. Illustration of possible interactions between NRs and dopamine
- Figure 5.2. The absorption and emission spectrum of MUA-NRs in water
- Figure 5.3. The emission spectra of MUA-NRs in pH 9 PBS buffer in the absence of oxygen with different amounts of dopamine added
- Figure 5.4. The quenching efficiency of MUA-NRs in different pH values in the presence and absence of oxygen
- Figure 5.5. Stern-Volmer plots of MUA-NRs emission quenching in different pH values in the presence and absence of oxygen
- Figure 5.6. Stern-Volmer plots of MUA-NRs emission quenching in pH 8 PBS buffer in the presence and absence of oxygen with the associated fitting
- Figure 5.7. The emission lifetime plots of MUA-NRs in pH 9 buffer in the presence of oxygen with different concentrations of dopamine

-
- Figure 5.8. Stern-Volmer plots of time components with different concentrations of the quencher in pH 9 buffer in the presence of oxygen
- Figure 5.9. TEM images of P-MUA-NRs at different sample positions
- Figure 5.10. Absorption and emission spectra of MUA-NRs and P-MUA-NRs in water
- Figure 5.11. Relative PLQY of P-MUA-NRs in buffers with different pH values
- Figure 5.12. The TA spectra of MUA-NRs and P-MUA-NRs at different delay times in water
- Figure 5.13. The kinetics of P-MUA-NRs and MUA-NRs at 460 nm (CdS) and 560 nm (CdSe)
- Figure 5.14. The emission spectra of HS-PEG-OCH₃-NRs in different pH value buffer in the absence and presence of oxygen with different amounts of dopamine added
- Figure 5.15. The quenching efficiency of HS-PEG-OCH₃-NRs in different pH values in the presence and absence of oxygen
- Figure 5.16. The illustration of the influence of pH and oxygen in the quenching experiment between HS-PEG-OCH₃-NRs and dopamine
- Figure 5.17. Stern-Volmer plots of HS-PEG-OCH₃-NRs emission quenching in different pH values in the presence and absence of oxygen.
- Figure 5.18. The illustration of hole transfer mechanism between HS-PEG-OCH₃-NRs and dopamine
- Table 3.1. Fitting parameters for the TA kinetics of the dot-in-rod NRs
- Table 3.2. Fitting parameters for the TA kinetics of the inside-out NRs
- Table 3.3. The detailed fit parameters of global kinetic fit for measurements on inside-out NRs at different times
- Table 3.4. The detailed fit parameters of the single kinetics fit of the CdSe part at the bleach signal minimum on the inside-out NRs at different times
- Table 4.1. IR-frequencies of TOPO and TOPO-NRs
- Table 4.2. IR-frequencies on MUA and MUA-NRs
- Table 4.3. IR-frequencies on HS-PEG-OCH₃ and HS-PEG-OCH₃-NRs
- Table 4.4. IR-frequencies of DHLA and DHLA-NRs
- Table 4.5. IR-frequencies of DHLA-PEG and DHLA-PEG-NRs
- Table 4.6. IR-frequencies on PEI and PEI-NRs
- Table 4.7. Steady-state absorption and emission spectroscopy on NRs #2 with different surface ligands
- Table 4.8. Fitting results of the emission lifetime of NRs with different surface ligands
- Table 4.9. Transient absorption spectroscopy on NRs with different surface ligands.
- Table 5.1. Time components of emission lifetime obtained with mono- or bi-exponential fit
- Table 5.2. Detailed fitting parameters in 460 nm (CdS) and 560 nm (CdSe) kinetics

In the Appendix

- Table A1. Detailed fitting parameters of multi-Gaussian peaks fit on the dot-in-rod and inside-out NRs absorption spectra
- Table A2. Detailed fitting parameters of multi-Gaussian peaks fit on the dot-in-rod and inside-out NRs emission spectra
- Table A3. Fitting results of the absorption spectra of NRs with different surface ligands by seven Gaussians
- Table A4. Fitting results of the emission spectra of NRs with different surface ligands by three Gaussians

- Figure A1. The global fit of the second TA measurement on the inside-out NRs and the DAS of global fit of CdS and CdSe
- Figure A2. The global fit of the third TA measurement on the inside-out NRs and the DAS of global fit of CdS and CdSe
- Figure A3. Gaussian fits of the absorption spectrum of MUA-NRs
- Figure A4. Gaussian fits of the absorption spectrum of HS-PEG-OCH₃-NRs
- Figure A5. Gaussian fits of the absorption spectrum of DHLA-NRs
- Figure A6. Gaussian fits of the absorption spectrum of DHLA-PEG-NRs
- Figure A7. Gaussian fits of the absorption spectrum of PEI-NRs
- Figure A8. Multi-Gaussian peaks fit of the emission spectra of NRs with different ligands
- Figure A9. The global fit of MUA-NRs kinetics and the DAS of global fit of CdS and CdSe parts
- Figure A10. The global fit of HS-PEG-OCH₃-NRs kinetics and the DAS of global fit of CdS and CdSe parts
- Figure A11. The global fit of DHLA-NRs kinetics and the DAS of global fit of CdS and CdSe parts
- Figure A12. The global fit of DHLA-PEG-NRs kinetics and the DAS of global fit of CdS and CdSe parts
- Figure A13. The global fit of PEI-NRs kinetics and the DAS of global fit of CdS and CdSe parts

CONFERENCE CONTRIBUTIONS

Poster presentation. **Bei, L.**; Micheel, M.; Maria, W. Towards Luminescent Water-Dispersible CdSe@CdS Nanorods with High pH-Stability. 2019 nanoGe Fall Meeting - Berlin, Germany.

LIST OF PUBLICATIONS

1. Micheel, M.; **Liu, B.**; Waechtler, M., Influence of Ligands on Charge-Carrier Trapping and Relaxation in Water-Soluble CdSe@CdS Nanorods. Catalysts, DOI: 10.3390/catal10101143.
2. **Liu, B.**; Chen, Z.; Lin, L.; Han, Y.; Pang, J.; Jiang, Z., Synthesis and characterization of poly(arylene ether ketone)s with 3,6-diphenyl-9H-carbazole pendants using C–N coupling reaction. High Performance Polymers 2016, 29 (5), 575-584.
3. Xie, Y.; **Liu, B.**; Chen, Z.; Han, X.; Liu, B.; Zhang, H.; Pang, J.; Jiang, Z., Graft fluorinated poly(arylene ether ketone)s containing highly dense sulfonic-acid-functionalized pendants for proton exchange membranes by C–N coupling. Polymer 2017, 131, 84-94.
4. Lin, L.; Chen, Z.; Zhang, Z.; Feng, S.; **Liu, B.**; Zhang, H.; Pang, J.; Jiang, Z., New comb-shaped ionomers based on hydrophobic poly(aryl ether ketone) backbone bearing hydrophilic high concentration sulfonated micro-cluster. Polymer 2016, 96, 188-197.

CHAPTER 1.

Introduction

1.1 Motivation

The energy crisis and the air pollution produced by burning fossil fuels have attracted worldwide attentions for decades.¹⁻⁹ The CO₂ emission produced by burning gas, coal and oil have great impacts on the Green House Effect.¹⁰ It has already been reported by New York Times that the climate change caused by Green House Effect already caused starving on the polar bears because the seeking of food is so difficult when icebergs are melted. The climate change will not only cause starving on polar bears but also on human because the climate change will also have bad influence on the food supply and agriculture.¹¹ By using hydrogen as the energy source, significant improvement could happen in the low-carbon future.¹²⁻¹⁴ Electricity generated by hydrogen would lead to nearly zero-carbon-emission energy storage and transportation.^{14, 15} A new energy system with reduced fossil fuel dependence would be established,¹⁶ with the versatility to operate across the transport,¹⁷ heat,^{18, 19} industry²⁰ and electricity divisions.^{21, 22} Together, these account for two-thirds of global CO₂ emissions.²³

The dot-in-rod CdSe/CdS nanorods, one of quantum confined semiconductor nanocrystals, has been proven to be suitable photosensitizers for photo driven hydrogen generation reaction (HER) due to their high extinction coefficient at visible light range, especially at blue light range.²⁴ These structures have attracted attentions from researchers all over the world, including myself. So, in this thesis, a study on their structures, surface ligands, and interactions with redox-active molecules (or polymers) will be presented.

1.2 A brief introduction to quantum confined semiconductor nanocrystals

The main research object of this thesis, the dot-in-rod CdSe/CdS nanorods (NRs), is one of the various quantum confined semiconductor nanocrystals. Quantum confined semiconductor nanocrystals are a group of semiconductor nanocrystals of which the electronic structure is modulated by their physical morphology and dimension. To be more precise, at least one of the dimensions locates in the range of 1 – 100 nm. The quantum confined semiconductor nanocrystals attracted attention all over the world in the past decades due to their unique physical and optical properties like quantum confined effect, tunable photoluminescence, and nonlinear optical properties.²⁵⁻²⁷

The quantum confined semiconductor nanocrystals can be classified by their morphology of the nanocrystals. The whole family includes the zero-dimensional (0D) spherical nanostructures, which are also called quantum dots and quantum confined in 3 dimensions, one dimensional (1D) elongated

nanostructures also known as NRs and nanowires which are quantum confined in 2 dimensions (2D), two-dimensional plate-like nanostructures typically referring to nanosheets or nanoplates, and three-dimensional (3D) nanostructures like tetrapods, nanoflowers, and many others.²⁸

The quantum confinement effect is observed in semiconductor nanocrystals when the size of the particle is comparable to the wavelength of an electron. The confinement of an exciton in nanocrystals strongly depends on the material dimension, namely the Bohr radius r_{Bohr} . The effective bandgap energy of quantum confined nanocrystals increases with the decrease of the size of the structures.²⁹

The surface effect is another crucial property of quantum confined semiconductor nanocrystal. The surface of a crystallized material is always imperfect. Therefore, surface defects are generated at the defective lattice position.³⁰ Compared with a bulky semiconductor material, of which the exciton is mostly localized far away from the material surface, the exciton in quantum confined semiconductor nanocrystals is much easier to be influenced by the surface defects of the nanocrystals. Also, as the size of a quantum confined semiconductor nanocrystal is getting smaller, the surface-to-volume ratio is increasing. Taking CdSe quantum dots as an example, the ratio between surface atoms and total atoms dramatically increases as the size of CdSe quantum dots decreases.³¹ Both of these facts indicate that the surface effect in a quantum confined semiconductor nanocrystals is much more pronounced than that in a bulk material. The surface state (electronic quantum states associated with the surface) will significantly influence the optical properties of the nanocrystals, namely optical absorption, photoluminescent (PL) and photoluminescent quantum yield (PLQY), and degrading due to aging.³² So, surface passivation is introduced to improve the surface defects of the quantum confined semiconductor nanocrystals while facilitating the solubility of the nanocrystals.

By adjusting the semiconducting materials and the morphology and dimension of the structure, the spectral active region could be tuned, ranging from ultraviolet (UV) to visible (Vis) spectra region due to the changing of the effective bandgap energy. For the research object of this thesis, namely CdSe/CdS dot-in-rod NRs, by adjusting the size of the CdSe core (dot) and the CdS rod in the NRs would lead to the quasi Type II band alignment. Upon excitation, the electron features mobility on the conduction band (CB) shared by the CdS shell and CdSe core, and the hole localizes at the CdSe core.³³

Combining all these properties mentioned above, quantum confined semiconductor nanocrystals are already widely used in the application of light-emitting diodes,³⁴⁻³⁷ sensors,³⁸⁻⁴⁰ biological compatibility,⁴¹⁻⁴⁵ and photocatalysts.⁴⁶⁻⁴⁸

1.3 The quantum confinement effects and bandgap

Materials can be built larger and larger, starting from atoms with discrete orbitals to molecules, then to small clusters (made up with several atom but still with discrete orbitals), and end up with the bulk limit

(see Figure 1.1). At a bulky level, the electronic structure of the material is pictured by energy bands with the related density of states. The bandgap is introduced here to describe the energy difference between the highest occupied band, namely the valence band (VB), and the lowest unoccupied band called the conduction band (CB). Generally, the quantum confinement effects refer to the unique properties in nanocrystals that the bandgap enlarges when the size of the nanocrystals decreases. As also shown in Figure 1.1, the effective bandgap of a larger quantum confined nanocrystals in size is smaller compared to the one with a smaller size.⁴⁹

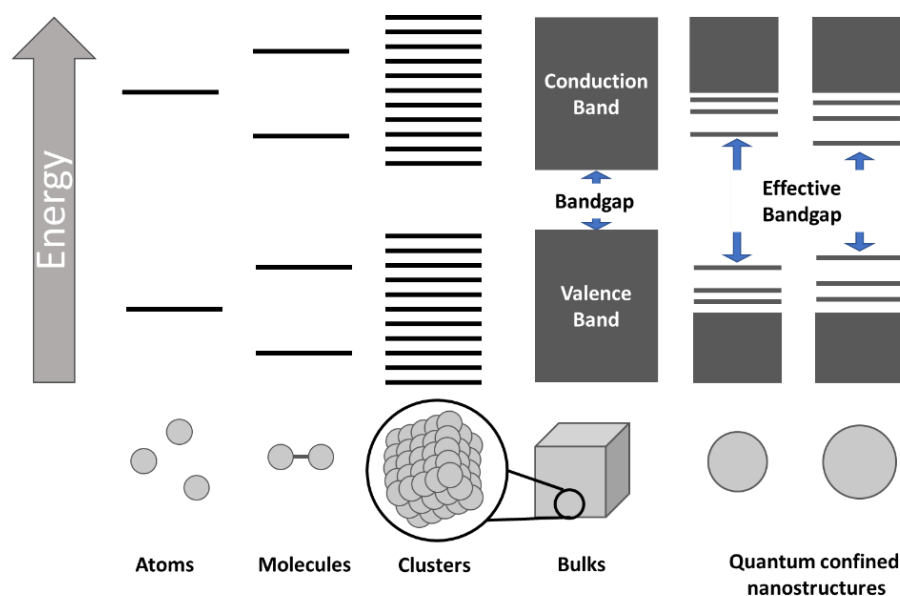


Figure 1.1. The electronic structure changes of semiconductor material from its atoms to its bulk material, together with its quantum confined nanocrystals.

With the bandgap energy excited, an electron and a hole can stay at a relatively far distance with nearly negligible Coulombic attraction. When the distance between carriers gets smaller, the electron and the hole may bound together and form an exciton, also known as an electron-hole pair. The distance between an exciton is called the exciton Bohr radius r_{Bohr} . If m_e and m_h refer to the effective masses of the electron and the hole, the r_{Bohr} for bulk semiconductor could be given by Equation 1.1.⁵⁰

$$r_{Bohr} = \frac{h^2 \epsilon}{4\pi^2 e^2} \left(\frac{1}{m_e} + \frac{1}{m_h} \right) \quad (1.1)$$

where h is the Planck's constant, ϵ is the dielectric constant of the material, and e is the charge of an electron. If the radius of semiconductor nanocrystals is approaching the r_{Bohr} , the movement of the exciton is spatially confined in the dimension of the semiconductor nanocrystals. As a result, the excitonic transition energy becomes higher, and this is the explanation for the experimental blue shift observed in the absorption and photoluminescence spectra of quantum confined semiconductor nanocrystals. This effect is much more pronounced when the dimension of the material is very small,

i.e., the radius of a quantum dot in the nanometer scale.⁵¹ The effective mass approximation (EMA) model is introduced here to explain the motion of excitons.

This EMA method is by far the most widely used model to explain the quantum confinement effect in nanocrystals, which is originated from the “Particle-in-Box Model” in quantum mechanics. In 1982, *Efros* and *Efros* first proposed this idea,⁵² and later *Brus* gave the theoretical calculation in 1984 and 1986.^{53, 54} In this model, the 0D quantum dot is considered as a particle in a potential well with an infinite potential barrier at the surface of the quantum dot. The particle is free to occupy any position in the box, and the equation used to describe the relationship between its energy ($E_{confinement}$) and the radius of the quantum dot (R) is given as:⁵³

$$E_{confinement} = \frac{h^2}{8R^2} \left(\frac{1}{m_e} + \frac{1}{m_h} \right) \quad (1.2)$$

Where h is the Planck’s constant, m_e and m_h refer to the effective masses of the electron and the hole. To simplify the calculation of the energy of the first excited electronic state (E) in a quantum confined quantum dot, this energy is separated by the different contribution sources. According to the EMA model, there are three primary energy sources: 1. the energy of bandgap generated by the energy difference between the CB and VB of the bulk material ($E_{bandgap}$), 2. the energy of the quantum confinement effect ($E_{confinement}$) which is already introduced above, and 3. the energy of the Coulombic attraction inside the exciton ($E_{Coulomb}$). Then the energy of the first excited electronic state (E) can be summed by Equation 1.3, and the energy shift of the bandgap (ΔE) can be expressed by Equation 1.4:

$$E = E_{bandgap} + E_{confinement} + E_{Coulomb} \quad (1.3)$$

$$\Delta E = E - E_{bandgap} = E_{confinement} + E_{Coulomb} \quad (1.4)$$

Then Equation 1.4 could be rewritten as Equation 1.5:⁵³⁻⁵⁷

$$\Delta E = \frac{h^2}{8R^2} \left(\frac{1}{m_e} + \frac{1}{m_h} \right) + \left(-\frac{1.78e^2}{\epsilon R} \right) \quad (1.5)$$

Where h is the Plank constant, R is the radius of the quantum dot, m_e and m_h refer to the effective masses of the electron and the hole, ϵ is the dielectric constant of the material, and e is the charge of an electron. Compared to the result of the Coulombic attraction, the quantum confinement effect is in domination. So, the energy shift of the bandgap ΔE increases as the quantum dot radius (R) decreases. For the same semiconductor material, by tuning the size of the quantum dots, varying bandgap energy could be obtained. Additionally, the emission energies of quantum dots (ΔE_F) could be obtained by Equation 1.6:^{54, 58}

$$\Delta E_F = E_{bandgap} + \frac{h^2}{8R^2} \left(\frac{1}{m_e} + \frac{1}{m_h} \right) \quad (1.6)$$

When the radius of a quantum dot (R) increases, the emission energy of the quantum dot (ΔE_F) decreases. In the case of CdSe quantum dots, almost all visible light range could be covered by tuning the size of the CdSe quantum dots resulting in different emission energies of quantum dots (ΔE_F).⁵⁹

1.4 Surface passivation

Surface defects introduced in section 1.1 in the quantum confined semiconductor nanocrystals play a role in the trapping of the electron, hole, or excitons.⁶⁰⁻⁶³ The trapping will further reduce the radiative recombination processes and then quench the PLQY.⁶⁴⁻⁶⁷ To improve the photostability of quantum confined semiconductor nanocrystals, surface passivation plays an important role here.⁶⁸ Theoretically, if all unsatisfied valences on the surface are well passivated, the nanocrystal would show no surface defects or surface states. Therefore, all states near the band edge are quantum confined, and only several discrete transitions are observable and represent discrete excitonic transitions like the 1S transition, as shown in Figure 1.2B. But in reality, not all surface defects could be well passivated. To decrease the surface states by surface passivation is very important in terms of improving the optical properties of quantum confined nanocrystals.⁶⁹ And the most common way to achieve this is by shielding an organic (surface ligands) or inorganic (also known as core/shell structure) layer on the nanocrystals. Worth mentioning here, the colloidal nanocrystals are always capped with organic layers, despite the passivation of inorganic layers.

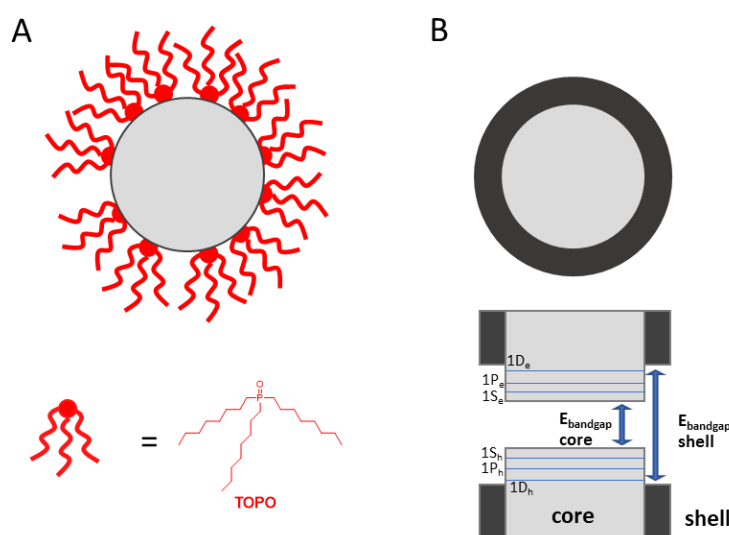


Figure 1.2. The schematic illustration of surface passivation on a quantum dot by (A) organic ligands (tri-n-octyl phosphine oxide (TOPO) in the figure) and (B) inorganic layer and the energy diagram of the energy difference between the core and shell together with the discrete transitions marked as 1S_e–1S_h, 1P_e–1P_h, and 1D_e–1D_h.

1.4.1 Organic Layer Passivation

The colloidal quantum confined semiconductor nanocrystals were first achieved by *Brus* and published in the 1980s by obtaining a colloidal suspension of CdS.⁷⁰ From then on, lots of affords were made by researchers all over the world to find the appropriate organic capping ligands.^{69, 71, 72} Phosphines⁷³ (for example, in Figure 1.2(A), tri-*n*-octyl phosphine oxide known as TOPO), and mercaptans (molecules with thiol group) are the state-of-the-art ligands used for colloidal stable nanocrystals in non-polar and polar solvents, respectively. Nanocrystals with organic ligands gain advantages in colloidal stability in either polar or non-polar solvent, then show great potential in water splitting,⁷⁴⁻⁷⁷ bio-sensing,^{42, 78-80} and other applications compared to those quantum nanocrystals that cannot be dissolved or dispersed in solvents. However, the organic ligands need to be handled with care. Organic ligands are usually disordered in structure and larger in volume compared to the surface sites on the nanocrystals.⁸¹ This will result in a low coverage rate, and some non-passivated surface sites will always be presented. For example, the coverage rate of TOPO capped on CdSe quantum dots with 3 nm diameter was reported to be only around 30 – 50%.^{82, 83} Another benchmark of organic surface passivation is ligands with amine groups.^{84, 85} The theoretical coverage of primary amines is close to 100%, much higher than the coverage rate of TOPO.⁸⁶ NRs capped with poly(ethylene imine) (PEI) showed impressive photocatalytic QY (~ 6.3%).⁷⁶ It has been suggested that the linear surface ligands leave gaps for oxygen to approach the surface of nanocrystals resulting in oxidation and decreased the PLQY.^{87, 88} Therefore, the surface of a nanoparticle would be more safely protected by a branched structure ligand.⁸⁹ However, as a fact, the bonding between the capping ligands and surface sites is usually weak resulting in detachment when irradiated under UV light source or washing with violent centrifugation.⁹⁰

1.4.2 Inorganic Layer Passivation

Aside from the organic layer passivation, another method is to use inorganic layers, namely a core/shell nanostructure (Figure 1.2(B)). Depending on the relationship between the bandgap of the core and the shell (also called the band alignment), the core/shell structures can be classified into different groups in Figure 1.3: Type I, inverted Type I, Type II and quasi Type II. The quasi Type II band alignment is mostly used in the design of quantum dots and NRs systems where the electron needs to be able to delocalize on the shared conduction band of both the core and shell, while the hole will be localized at the core.^{91, 92} This will generate a long-lived PL lifetime, which is an advantage for photocatalyst and will be mainly discussed in section 1.5. But before that, the Type I, inverted Type I and Type II need to be introduced. There are also other types of band

alignments like the Type III (broken gaps), but they are less related to the topic of this thesis and will not be introduced here.

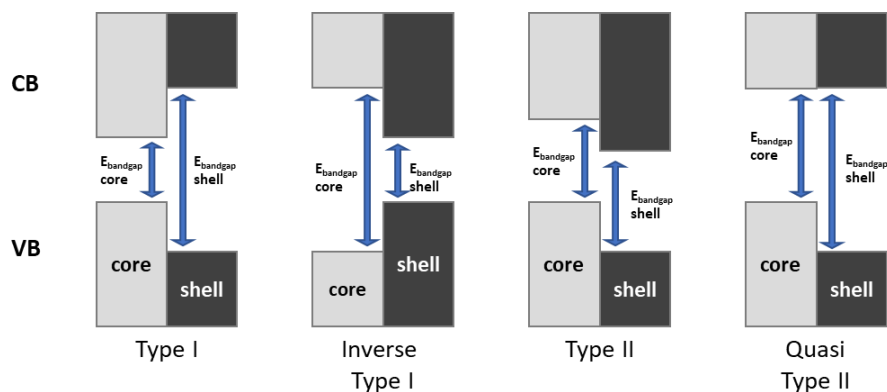


Figure 1.3. Different types of the core/shell nanocrystals based on the band alignment.

1.4.2.1 Type I band alignment

The photoluminescence of nanocrystals is found to be more photostable with a large bandgap material grown epitaxially due to the exciton confinement at the core generated by the energetic barrier, as shown in Figure 1.3. This kind of band alignment is called Type I.⁹³⁻⁹⁵ Coherency strains are usually discovered in the mismatched part between the core and the shell, which is introduced by the epitaxial growth when the shell material is adapting the lattice parameters of the core material. The mismatch is always presented in the percentage explained by the ratio of the difference between two different lattice parameters. The strain results in a redshift in the absorption and emission spectra of the nanocrystals in some cases.⁹⁶ By using CdSe as the material of the core, lots of potential materials were introduced to be grown epitaxially as the shell on the core. Among all of the potential materials, ZnS,^{64, 97} ZnSe,^{98, 99} and CdS¹⁰⁰ stand out because of their larger bandgap (> 1.76 eV, the bandgap of CdSe) and low lattice mismatch ($< 12\%$, the threshold of dislocations between core and shell).⁹³ The lattice mismatch is 10.6% between CdSe and ZnS,¹⁰¹ which is larger than that between CdSe and ZnSe at 6.3%,⁹⁸ while the smallest mismatch is only 3.9% between CdSe and CdS. Both ZnS and ZnSe are quiet good materials to act as the shell in terms of exciton confinement and PLQY. Moreover, the CdS seems to be a better material due to the smallest mismatch and lower strains resulting in higher PLQYs with longer PL lifetimes.^{93, 102, 103}

1.4.2.2 Inverted Type I band alignment

Inverted core/shell nanocrystal structure is another way to cap inorganic layers on the nanocrystals. The word “inverted” means that the bandgap of the shell material is

smaller than the bandgap of the core material (Figure 1.3). The inverted core/shell semiconductor nanocrystals include but not limit to CdS/CdSe,¹⁰⁴ ZnSe/CdSe,¹⁰⁵ and CdS/HgS.¹⁰⁶ Taking ZnSe/CdSe quantum dots as an example, the VB of ZnSe is lower than that of CdSe, and the CB of ZnSe is higher than that of CdSe. This kind of band structure directly results in the localization of the electron and hole in the CdSe shell region. This is an advantage when dealing with electron and/or hole removal process in the applications of solar cells¹⁰⁷ or electrodes.¹⁰⁸ Similar to Type I band alignment, the PL wavelength of the inverted Type I band aligned nanocrystals could be tuned by the shell thickness.¹⁰⁵ However, due to the localization of the electron and hole at the shell, increased interaction with surface trap states results in poor photostability.¹⁰⁹

1.4.2.3 Type II band alignment

Like Type I and inverted Type I band alignment, Type II band alignment has a characteristic relationship between the band structure of the core and shell. In this case, the VB edge of the core is in the range of the bandgap of the shell, while the CB edge of the shell is in the range of the bandgap of the core (Figure 1.3). Upon excitation, the electron is confined at the shell while the hole is confined at the core.¹¹⁰ The first reported Type II semiconductor quantum dots were the CdTe/CdSe and CdSe/ZnTe core/shell quantum dots by Bawendi group. Long photoluminescence (PL) lifetime was observed due to the separated localization of the electron and hole at the shell and the core, respectively.¹¹¹ Later, by altering the precursors to TOP:Te and TOP:Se (TOP:X refers to X element dissolved in tri-n-octyl phosphine), CdTe/CdSe quantum dots with improved photoluminescence quantum yield (PLQY) up to 40% were synthesized. With relatively high PLQY and long-lived lifetime, Type II band alignment nanocrystals show great potential in photocatalyst where these properties favor the catalytic efficiency and solar cells where these properties facilitate the high photon-to-current conversion efficiency.¹¹²⁻¹¹⁴

1.4.2.4 Quasi-Type II band alignment

Peng et al. first reported on the achievement of -0.3 eV (Type II) to 0.3 eV (Type I) conduction band potential offset between the core and shell in the CdSe/CdS core/shell quantum dots by tuning the size of the CdSe core.⁹³ This indicates the possibility of achieving a nearly negligible conduction band potential offset by tuning the core size and opened the door for achieving Quasi-Type II band alignment. It is now generally agreed that the electronic structure is tunable from Type I to Quasi-Type II depending on the core size, rod diameter and sometimes interfacial strain.¹¹⁵⁻¹¹⁹ The quasi Type II band alignment is mostly used in the design of NRs systems where the electron needs

to be able to delocalize on the shared conduction band of both the core and shell, while the hole will be localized at the core. The recombination process is much longer compared to Type I band alignment due to the spatial separated electron and hole. This would favor the charge separation resulting in better catalytic performance.²⁴

1.4.3 Non-epitaxial growth

Most of the semiconductor nanocrystals contain toxic elements like Cd, Se, and Te. When such materials are used in biological applications, non-epitaxial growth of the shell is promising in terms of preventing the leaking of toxic ions. Non-epitaxial growth includes both organic and inorganic coating. A silica shell was reported to be good shell material in terms of preventing the leaking of Cd²⁺ from CdTe quantum dots.¹²⁰ Also, recent results showed that non-toxic polymer coating on semiconductor nanocrystals also reduced the toxic level of the material when used *in vivo*.^{79, 121}

1.5 A brief introduction to the synthesis of quantum dots and NRs

In this section, the basic synthesis methods are introduced on the quantum dots (and the core/shell quantum dots) and NRs (and the dot-in-rod NRs). The “hot injection” method is used in this thesis for CdSe quantum dots synthesis due to the simplicity of operation and high quality of quantum dots product in terms of narrow size distribution and high PLQY.⁷³ And the “seeded growth” method is used in this thesis for the synthesis of the CdSe/CdS dot-in-rod NRs due to the similarity in operation and high quality of NRs product compared to the “hot injection” method.

1.5.1 Quantum dots (including the core/shell quantum dots)

Semiconductor quantum dots are a group of sphere shape nanocrystals with a diameter ranging in 1 – 100 nm. The composition of semiconductor quantum dots includes CdSe, CdS, ZnSe, ZnS, CdTe, PbS, InP, and so on.¹²²⁻¹²⁶ The history of the application of quantum dots is far longer than we expected and may date back to 4000 years ago that ancient Egyptian cosmetics already introduced PbS nanoparticles to darken the hairs.¹²⁷ These PbS nanoparticles had a size of 5 nm, which was quite similar to the PbS quantum dots synthesized with modern synthesis methods.^{128, 129} Since the band alignment of quantum nanocrystals are already introduced in section 1.3.2, the introduction of quantum dots in this part shall only focus on its morphology and synthesis methods. The synthesis method of quantum dots can be classified as physical methods and chemical methods.¹³⁰ The most common physical method is to break down bulk semiconductors, but the obtained quantum dots are without surface ligands resulting in non-dispersible quantum dots in any solutions.^{131, 132} The chemical methods are much better in terms of obtaining colloidal

quantum dots suspension. The state-of-the-art chemical method is the “hot-injection” method, as shown in Figure 1.4, which is proposed by Bawendi group in their first published paper reporting quantum dots synthesis in organic solvents.⁷³ The precursor was injected into the reaction mixture at high temperature to form nuclei, and then the growth of the core happened at a relatively low temperature. This method successfully separates the nucleation and growth processes of the quantum dots resulting in narrow size distribution and high quality in crystallization.⁷³ For the synthesis of core/shell quantum dots, successive ion layer adsorption and reaction (SILAR) and the “seeded growth” method are the main methods.^{133, 134} SILAR is to inject the precursor containing shell material cation or anion one after another into the seed precursor in order to control the number of shell layers while the “seeded growth” method is to inject the shell material anion precursor into the precursor mixture of the shell material cation followed by the injection of the seed at high temperature.

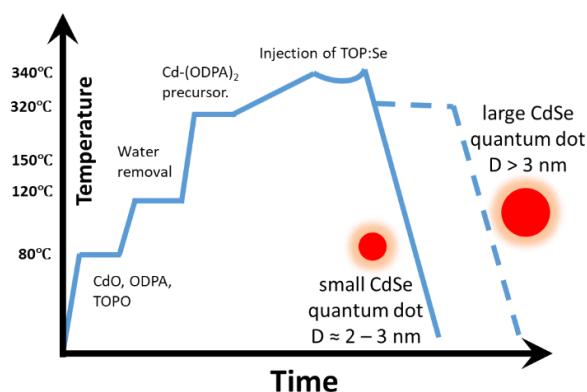


Figure 1.4. The “hot injection” method of CdSe quantum dots synthesis. CdO, octadecylphosphonic acid (ODPA) and TOPO were melted at 80 °C and heated up to 120 °C in vacuum to remove water. Mixture were heated up to 320 °C to form the Cd-(ODPA)₂ and then heated up to 340 °C followed by a quick injection of TOP:Se (Se dissolved in trioctylphosphine). The size of the CdSe quantum dots could be tuned by varying the reaction time. Longer reaction time results in bigger quantum dots and shorter reaction time results in smaller quantum dots. In this thesis, the reaction is cooled down immediately after the injection results in CdSe quantum dots with diameter of 2.2 nm.

1.5.2 NRs and the dot-in-rod NRs

Both SILAR and “seeded growth” methods are facing the anisotropy growth of the shell when the reaction is kinetically overdriven by a very high monomer concentration (monomer is adopted from *Ref.* 105 as the small particle after short time of shell growth).^{135, 136} This seems to be a huge problem for core/shell quantum dots but miraculously opens a new door for the synthesis of different shapes of the nanocrystals. CdSe NRs were first obtained by taking the benefit of the anisotropic wurtzite CdSe.^{135, 136} By adding phosphonic acids, the specific binding of the ligands

to crystal facets results in the decrease of the number of nucleus and the increase of the monomer concentration further resulting in exclusive growth along the c-axis.¹³⁷ From then on, various semiconductor NRs have been synthesized, such as CdS and PbSe.¹³⁸ There are some unachievable properties (for example, band alignment) for single component NRs. Therefore, hetero-nanorods with different components of materials have been synthesized. The “seeded growth” method, as shown in Figure 1.5, is until now one of the most studied methods to achieve dot-in-rod NRs since 2007.^{134, 139} The band alignment of the dot-in-rod NRs is quite similar to the band alignment of the core/shell quantum dots. The main research object of this thesis is the Quasi-Type II NRs and more information will be introduced in the next section.

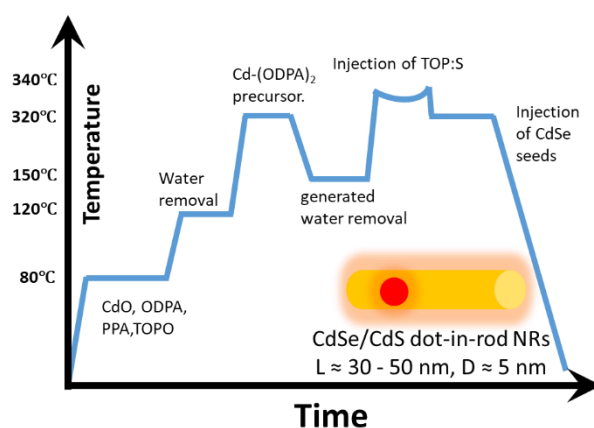


Figure 1.5. The “seeded growth” method of CdSe/CdS dot-in-rod NRs synthesis. CdO, ODPA, propylphosphonic acid (PPA) and TOPO are melted at 80 °C and heat up to 120 °C in vacuum to remove water. After purging N₂, reaction mixture is heated up to 320 °C to form the Cd-(ODPA)₂ and then cooled down to 120 °C to remove the generated water in vacuum. After purging with N₂, the reaction mixture is again heated up to 340 °C followed by a quick injection of TOP:S and CdSe seed. The length of the CdSe/CdS dot-in-rod NRs could be tuned by varying the reaction time and the amount of CdO. Longer reaction time and higher amount of CdO results in longer NRs and shorter reaction time and lower amount of CdO results in shorter NRs. In this thesis, the reaction is cooled down 10 min after the injection of the seeds results in NRs with length of 30 nm and diameter of 5 nm.

1.6 Quasi-Type II band alignment in CdSe/CdS dot-in-rod NRs and the potential application in hydrogen evolution reaction (HER)

The focus of this thesis is CdSe/CdS dot-in-rod NRs, which have been proven to be synthesized as Type I and quasi Type II band alignment structures. These different band alignments are achieved by tuning the size of the CdSe core in the dot-in-rod NRs.¹¹⁵ Because the tips of NRs are often associated with high-energy crystal faces,¹⁴⁰ selective growth of metal nanocrystals (such as platinum and gold)^{140, 141}

at the tip have been readily achieved. This results in an integrated triadic semiconductor/metal NRs heterostructures consisting of well-positioned light-absorbing, charge separating, and catalytic components, which can be used as the ideal materials for solar-to-fuel conversion.²⁴ In Figure 1.4, the basic working principle is illustrated. Upon photoexcitation, electrons are transferred to the Pt tip for the catalytic reduction of 2H^+ to H_2 , while holes are transferred to the CdSe core and then removed by external electron donors, such as phenothiazine,¹⁴² SO_3^{2-} , triethylamine (TEA), and EDTA^+ .¹⁴³

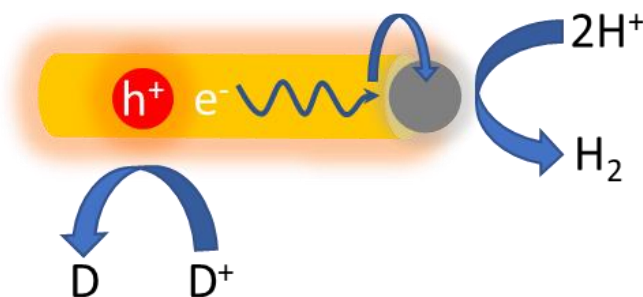


Figure 1.6. Schematic illustration of a triadic nanorod: a CdSe/CdS nanorod with a Pt nanoparticle at one tip. D is an external sacrificial electron donor.

The removal of hole is a key efficiency limiting step in the photocatalytic HER.¹⁴³⁻¹⁴⁶ *Zamkov et al.* reported that H_2 generation performances from MUA capped-ZnSe/CdS–Pt NRs was ~ 300 -fold higher than MUA capped-ZnTe/CdS–Pt NRs due to favored hole transfer for the ZnSe core. *Berr et al.* reported highest H_2 generation QYs (averaged over 4 hours of irradiation) for CdS–Pt NRs with SO_3^{2-} (1.7%) in their experiments. Based on this results, *Wu et al.* further investigated H_2 generation efficiencies of the CdSe/CdS dot-in-rod NRs in the presence of different electron donors and found that MeOH exhibited higher efficiency in heterostructure NRs while SO_3^{2-} showed worked better in CdS–Pt NRs.¹⁴⁷ However, the removal of the holes is achieved by an excess of the sacrificial electron donors, which results in a low energy gain.²⁴ And if the holes are not removed or consumed, it will lead to the oxidation of the NRs.¹⁴⁸ The surface ligand of NRs is also important in terms of hole transfer. MUA is reported to not only endow NRs with water dispersibility but also reduce the PL lifetime of ZnSe/CdS dot-in-rod NRs from 42.0 to 1.9 ns compared to the native non-polar ligands due to ultrafast hole transfer to MUA.¹⁴⁴ And surface ligands also alter the surface states of NRs due to surface passivation of surface dangling sites further influencing the optical and catalytic performance which was introduced in section 1.3.1.

Research works on this structure are mainly focused on these aspects: 1. easier hole removal. The dot-in-rod structure favors the electron motion across the rod, but the hole is selectively localized in the dot away from the interface of this structure. This will introduce difficulties when removing the residual hole. This could be achieved by using small band gap material as the shell material to make the hole localization at the surface of the NRs. 2. phase transfer with high stability. For most HERs, NRs should

be soluble or dispersible in water or other polar solvents. However, with the state-of-the-art “seeded growth” synthesis method, NRs are capped with TOPO as surface ligands, which only make NRs dispersible in non-polar solvents such as toluene, hexane. The phase transfer of the NRs while keeping their electronic structure and the high photoluminescence is a hot topic. 3. the control over HERs by designing a switch. By intercepting the electron to the catalytic center, it is possible to switch on and off of the HERs. A matrix made up of redox-active polymer would make it possible to achieve this aim. These aspects are also the topics that will be focused in this thesis.

1.7 The outlines of this thesis

This thesis is mainly focused on the structure comparison between CdSe/CdS dot-in-rod NRs and CdS/CdSe nanobells, synthesis and characterization of CdSe/CdS dot-in-rod NRs with different water-soluble surface ligands and their influence on the exciton dynamics, and the interaction between CdSe/CdS dot-in-rod NRs and redox-active molecules (and polymers). So, in this thesis, the NRs will be investigated from the inside out. The aim of this thesis is to make contribution to finding new photosensitizers with better hole removal capability by investigating CdSe/CdS NRs with CdSe shell, improving the catalytic efficiency of HER by improving the understanding of the influence introduced by different surface ligands on the dot-in-rod NRs, and achieving a switchable system for HER by gaining knowledge on the switchable photoluminescence systems using the dot-in-rod NRs and dopamine (or polydopamine). Ultimately, I sincerely wish my work may make a tiny contribution to the development of zero-carbon-emission energy systems and reducing energy crisis.

Chapter 2 introduces the basic methods used in the investigation of the research object together with the synthesis procedures of related materials.

Chapter 3 introduces and discusses on the properties of CdS/CdSe nanobells (namely, the CdSe/CdS inside-out NRs in chapter 3) using CdSe/CdS dot-in-rod NRs as the reference. The features of the CdSe/CdS inside-out NRs are probed by steady-state measurements and transient absorption measurements to reveal the influence of different nanostructures on the surface states and carriers' dynamics.

Chapter 4 deals with the CdSe/CdS dot-in-rod NRs and their phase transfer into water. The dot-in-rod NRs with six different surface ligands will be investigated in this chapter in terms of the steady-state measurements and time-resolved measurements to understand the influence of surface ligands on the surface states and carriers' dynamics. The pH stability is also investigated to match ligands with potential applications.

Chapter 5 discusses the interaction between CdSe/CdS dot-in-rod NRs and the redox-active molecules, namely dopamine, as well as the redox-active polymer, namely polydopamine. The interaction is probed

by steady-state quenching experiments and time-resolved PL quenching experiments to reveal the quenching mechanism of either electron transfer or hole transfer of the dot-in-rod NRs.

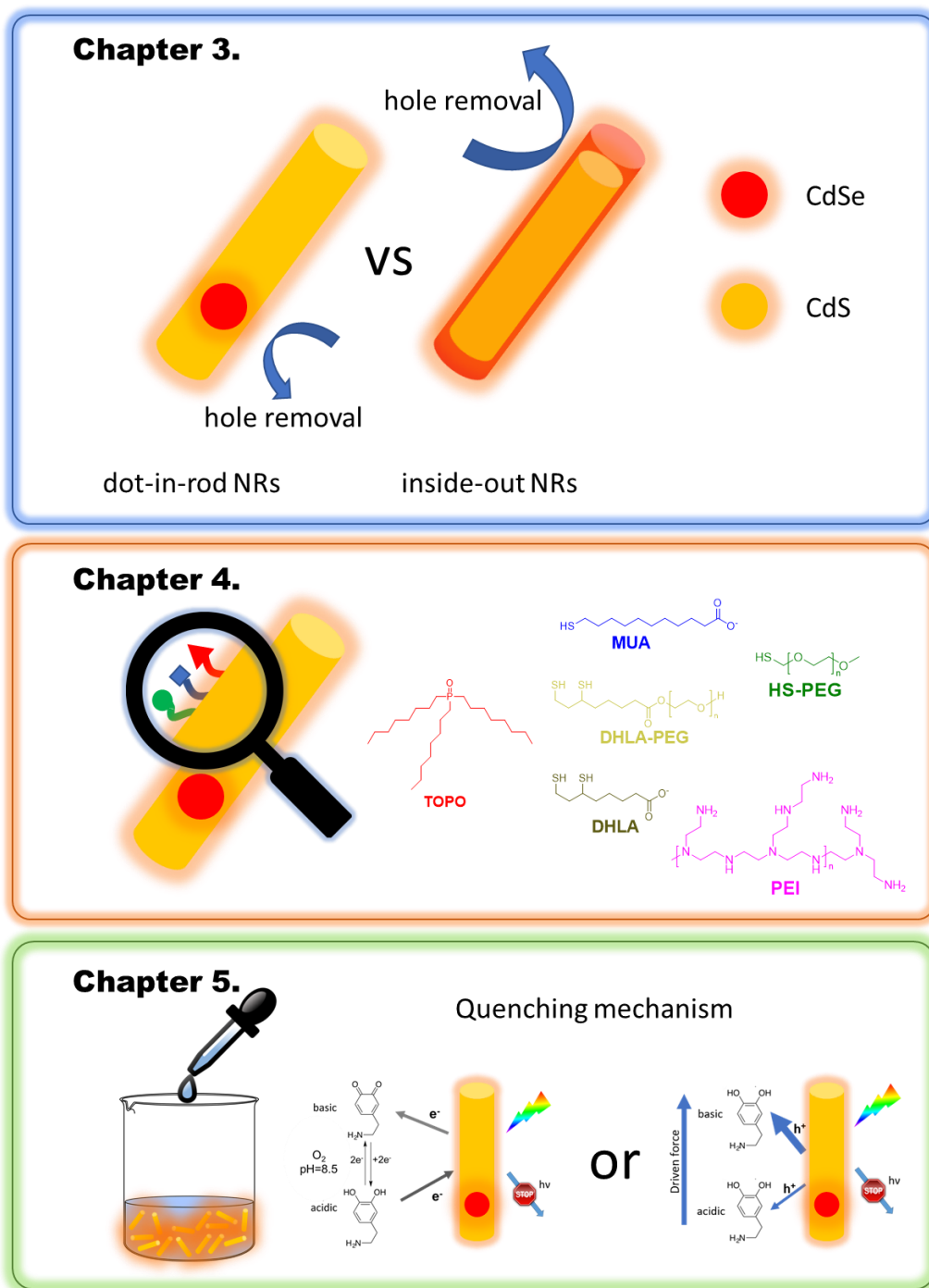


Figure 1.7. Schematic outline of this thesis' structure. In chapter 3, the dot-in-rod NRs and inside-out NRs are investigated with regards to the influence of structures on their carrier dynamics. In chapter 4, phase transfer of the dot-in-rod NRs are investigated especially on the influence of surface states introduced by different surface ligands. In chapter 5, the quenching mechanisms are investigated between the dot-in-rod NRs and dopamine / polydopamine.

CHAPTER 2.

Experimental Section

This chapter mainly talks about the synthesis of the CdSe/CdS dot-in-rod NRs together with the ligand exchange protocols and all methods introduced to probe the properties of the research objects in this thesis. The “synthesis protocols” part includes the synthesis of CdSe quantum dots and CdSe/CdS dot-in-rod NRs, synthesis and characterization of ligands, and the ligand exchange protocols. The “methods” part contains the basic information on the introduced instruments in this thesis.

2.1 Synthesis protocols

All chemicals and solvents were purchased from Sigma-Aldrich (now known as Merck KGaA), except octadecylphosphonic acid (ODPA) was purchased from Carl Roth, and all solvents were of spectroscopic grade. All chemicals and solvents were used without any further purification. Water was deionized and degassed before use except for the measurements taken under the air atmosphere where water was only deionized. In this thesis, the CdSe quantum dots were capped with TOPO and CdSe/CdS NRs were capped with several different surface ligands, then “ligands name” referred to the pure ligands, and “Ligand-NRs” referred to NRs with the related ligand. For example, TOPO (trioctylphosphine oxide) refers to the pure TOPO ligand, and TOPO-NRs refers to the TOPO capped NRs.

6.1.1 Synthesis of the seeds (CdSe quantum dots)

Synthesis of the CdSe seed was adopted from a reported procedure.¹³⁹ The synthesis setup was illustrated in Figure 2.1. A 25-mL-three-neck-flask was filled with 3.00 g (TOPO), 0.28 g octadecyl-phosphonic acid (ODPA), 0.06 g CdO. The synthesis was conducted under constant stirring and an inert atmosphere if not indicated otherwise. The flask was heated up to 80 °C to melt the chemicals and evacuated to get rid of the water content in the chemicals. Once no more gas emerged from the solution, the flask was heated to 120 °C and kept evacuated for 30 min. After that, the flask was purged with N₂. The flask was then heated to 320 °C, upon which the solution turned colorless due to the complexation of Cd-(ODPA)₂. Then, the flask was heated up to 340 °C. Next, 0.058 g CdSe dissolved in 0.36 g trioctylphosphine (TOP) was injected. After the injection, the heating was immediately stopped, and the flask was cooled down by N₂ airflow to accelerate the cooling speed. After the temperature of the mixture was cooled down to 90 °C, 5 mL of toluene was injected into the mixture to stop the solidification of the mixture. The seeds were cleaned by centrifugation with 10 mL toluene in 10 mL methanol for five times and then dissolved in toluene. The characterization of the seeds was performed by transmission electron

microscopy (TEM) and an empirical literature-known formula¹⁴⁹ (displayed in Equation 2.1) with a diameter of 2.2 nm. D is the diameter and λ is the wavelength (nm) of the first excitonic absorption peak of the CdSe seeds.

$$D = (1.61 \times 10^{-9})\lambda^4 - (2.66 \times 10^{-6})\lambda^3 + (1.62 \times 10^{-3})\lambda^2 - (0.43)\lambda + 41.57 \quad (2.1)$$

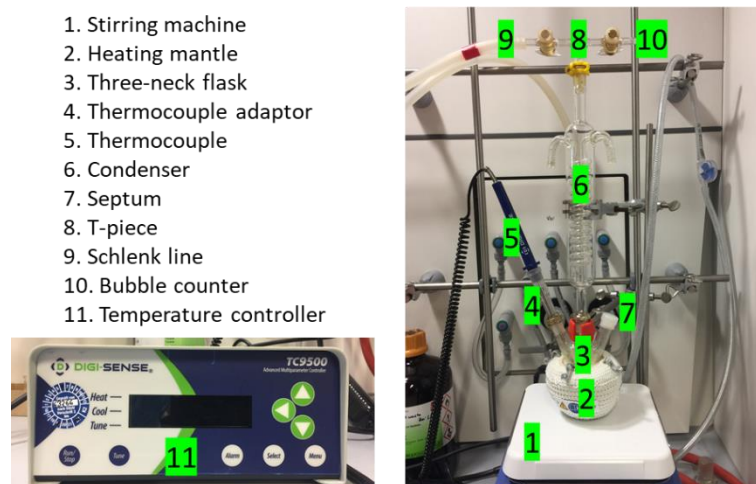


Figure 2.1. The synthesis setup of CdSe quantum dots by the “hot-injection” method. All parts were labeled with numbers and descriptions.

6.1.2 Synthesis of dot-in-rod TOPO-NRs

The synthesis of TOPO-NRs was adopted from a literature-known procedure.¹³⁴ The same synthesis setup was used in the NRs synthesis as the setup showed in Figure 2.1. A 25-mL-three-neck-flask was filled with 3.35 g TOPO, 1.08 g ODPA, 0.207 g CdO and 0.06 g n-propylphosphonic acid (PPA). The synthesis was conducted under constant stirring and an inert atmosphere if not noted otherwise. The flask was heated up to 80 °C until the reaction mixture melted and evacuated to remove residual water from the mixture. Once gas formation stopped, the flask was heated to 120 °C and kept evacuated for 30 min. After that, the flask was flooded with N₂. The flask was then heated to 320 °C, upon which the solution turned colorless due to the complexation of Cd-(ODPA)₂, and then cooled down to 120 °C. Next, a vacuum was applied until gas formation in the reaction mixture stopped (at least 2 hours) to remove water, which was a side product of Cd-(ODPA)₂ complexation. Then, the flask was flooded with N₂ again and heated up to 340 °C. Next, 1.5 g TOP and 0.05 g sulfur dissolved in 0.60 g TOP were injected. After 20 s, 2 mg of CdSe seeds (diameter = 2.2 nm) dissolved in 0.5 g TOP were injected. The reaction was stirred for 10 min until the color of the solution turned from red to orange. 5 mL of toluene was injected into the mixture once the temperature dropped below the flashing point of toluene to stop the solidification of the mixture. The rods were cleaned by 5000 rpm

centrifugation with 6 ml n-hexane, 2 ml nonanoic acid, and 2 ml octylamine in 10 ml methanol five times. The size of the rods was selected by centrifugation at 4200 rpm for 30 min with 10 ml toluene and 8 ml isopropanol. The NRs were then dispersed in toluene to form TOPO-NRs suspension for further investigation.

6.1.3 Ligand exchange with 11-mercaptoundecanoic acid (MUA)

The ligand exchange procedures of MUA were adopted from the paper published by *Amirav et al.* with slight modification.¹⁵⁰ 250 mg MUA was dissolved in 25 ml methanol, and tetramethylammonium hydroxide pentahydrate was added until the solution reached pH 11 (c. 200 mg). 20 mg TOPO-NRs (dried under vacuum from its toluene solution) were added into this mixture and stirred for 2 h. When the NRs were fully dispersed, c. 35 mL of toluene was added as non-solvent until NRs precipitated. The mixture was then centrifuged at 6000 rpm for 20 min, and the precipitate was dispersed in degassed deionized water to obtain MUA-NRs suspension.

6.1.4 Ligand exchange with poly(ethylene glycol) 2-mercaptoethyl methyl ether (HS-PEG-OCH₃)

The ligand exchange procedures of HS-PEG-OCH₃ was adopted from the ligand exchange protocol of MUA (see above). 50 mg HS-PEG-OCH₃ ($M_n \approx 800 \text{ g mol}^{-1}$, equal to roughly 18 repeating units) was dissolved in 5 ml methanol, and tetramethylammonium hydroxide pentahydrate was added until the solution reached pH 11 (c. 40 mg). 4 mg dry TOPO-NRs were added into this mixture and stirred for 2 h at room temperature. Because of the amphiphilic property of HS-PEG-OCH₃, the capped NRs exhibited good solubility in both polar and non-polar solvents. So, the mixture was then transferred into a Vivaspin 20 centrifugal concentrator with Molecular weight cut-off (MWCO) at 10kDa and then centrifuged at 6000 rpm for 20 min. The precipitate was then redispersed in 5 mL methanol and centrifuged again under the same conditions. This step was repeated three times in total. The precipitate was dispersed in degassed deionized water to get HS-PEG-OCH₃-NRs suspension.

6.1.5 Synthesis of and ligand exchange with dihydrolipoic acid–poly(ethylene glycol) ester (DHLA-PEG)

Synthesis and ligand exchange of DHLA-PEG followed a literature-known protocol¹⁵¹ by *Uyeda et al.* In short, poly(ethylene glycol) (PEG) (100 mmol, $M_n \approx 400 \text{ g mol}^{-1}$, equal to roughly nine repeating units) was attached to lipoic acid (LA) (10 mmol) using a dicyclohexylcarbodiimide (DCC) (11 mmol)-mediated esterification reaction with 4-(dimethylamino)-pyridine (DMAP) (3 mmol) as a catalyst to obtain LA-PEG. The solvent was dichloromethane (100 mL). The

precipitate that formed was filtered over a plug of Celite, and the residual organic mixture was washed with brine (75 mL) three times to wash away excess PEG. The combined organic extracts were dried over MgSO_4 , filtered, and evaporated. The crude product was purified by chromatography (ethyl acetate/methanol 95:5) and evaporated to obtain LA-PEG as a yellow oil. The reduction reaction was performed by adding NaBH_4 (2.2 mmol) into LA-PEG (2 mmol) in a 1:4 ethanol/water solution. To get pure DHLA-PEG, column chromatography (ethyl acetate/methanol 90:10) was applied. The product structure was confirmed by the assignment of protons in the proton nuclear magnetic resonance ($^1\text{H-NMR}$) and $^1\text{H} - ^1\text{H}$ correlation spectroscopy (COSY). $^1\text{H-NMR}$ of DHLA-PEG (upper) and LA-PEG (bottom) was displayed in Figure 2.2 with assignments of all protons.

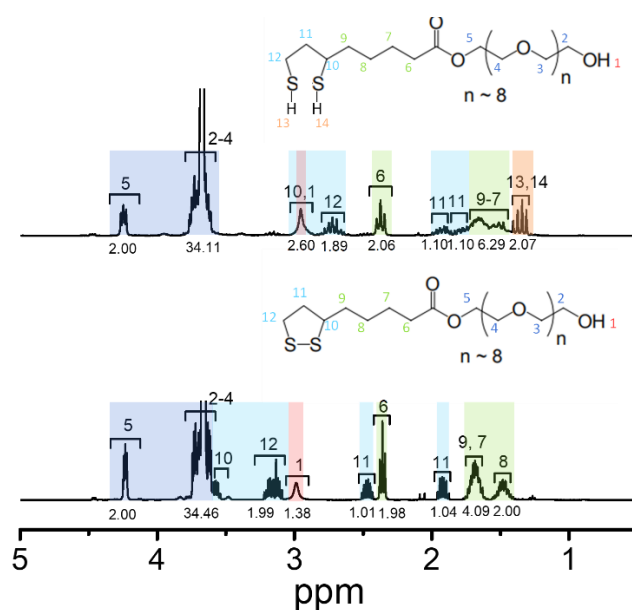


Figure 2.2. The $^1\text{H-NMR}$ spectrum of DHLA-PEG (upper) and LA-PEG (bottom) in CD_2Cl_2 .

For the ligand exchange, 50 mg DHLA-PEG was dissolved in 5 mL methanol, and 4 mg dry TOPO-NRs were added. The mixture was heated at $50\text{ }^\circ\text{C}$ for 4 hours under constant stirring. Because of the hydrolysis of the $-\text{COOR}$ group in DHLA-PEG, the ligand exchange could not be performed in a basic environment as the same as the ligand exchange of MUA. As DHLA-PEG-NRs were dispersible in both polar and unipolar solvents, the sample was purified using a centrifugal concentrator. The mixture was placed in a Vivaspin 20 centrifugal concentrator and centrifuged at 6000 rpm for 15 min. This step was repeated three times with methanol to purify the DHLA-PEG-NRs. The precipitate was then dispersed in degassed deionized water to get DHLA-PEG-NRs suspension.

6.1.6 Synthesis of and ligand exchange with dihydrolipoic acid (DHLA)

Synthesis and ligand exchange of DHLA followed the above-mentioned literature-known protocol¹⁵¹ by *Uyeda et al.* In short, LA was reduced by NaBH₄, followed by column chromatography to get pure DHLA.

The ligand exchange was carried out with a similar protocol as the HS-PEG-OCH₃ ligand exchange. 50 mg DHLA was dissolved in 5 ml methanol, and tetramethylammonium hydroxide pentahydrate was added until the solution reached pH 11 (c. 40 mg). 4 mg dry TOPO-NRs (dried under vacuum from its toluene solution) were added into this mixture and stirred for 2 h. The mixture was then transferred into a Vivaspin 20 centrifugal concentrator and then centrifuged at 6000 rpm for 20 min. The precipitate was then redispersed in 5 mL methanol and centrifuged again under the same conditions. The cleaning step was repeated three times in total. The precipitate was then dispersed in degassed deionized water to form DHLA-NRs suspension.

6.1.7 Ligand exchange with hyperbranched poly(ethylene imine) (PEI)

The ligand exchange protocol was adapted from a protocol by *Thomas et al.* for TOPO-capped CdSe@ZnS quantum dots.¹⁵² 4 mg TOPO-NRs and 50 mg hyperbranched PEI ($M_n = 25000 \text{ g mol}^{-1}$) were dispersed in 5 mL CHCl₃. The mixture was stirred for 4 h, followed by adding 10 mL cyclohexane to precipitate the NRs. The precipitate was collected by centrifugation at 6000 rpm for 15 min and dispersed in degassed deionized water to get PEI-NRs suspension.

2.2 Methods and instruments

2.2.1 Transmission electron microscopy (TEM)

To characterize the morphology and calculate the size and distribution of synthesized quantum dots and NRs, transmission electron microscopy was used. The TEM images were taken by a JEOL JEM-1400 transmission electron microscope (JEOL Ltd., Japan) with a beam source of lanthanum hexaboride (LaB₆). The length of the NRs was determined by measuring all the NRs that appeared in the TEM images clear enough to be counted as individuals. All measures were marked with red lines in the images. Then the average length and the standard deviation (SD) were calculated to give the distribution of the length of the NRs. The width of the NRs was determined in the same way as the length of the NRs.

2.2.2 Steady-state absorption and photoluminescence spectroscopy

To probe the transitions from the electronic ground state in the research object in this thesis, steady-state absorption spectroscopy was introduced. Absorption spectra were recorded in a quartz cell ($d = 1$ cm) using a JASCO V780 UV-Visible spectrophotometer (JASCO Germany GmbH, Germany). All measurements were performed in a wavelength range from 200 nm to 800 nm (some absorption plots in this thesis may be displayed in a different range for better comparison). The measurements were carried out using a double beam method (in Figure 2.3), so a cuvette with a pure solvent was always measured as a reference.

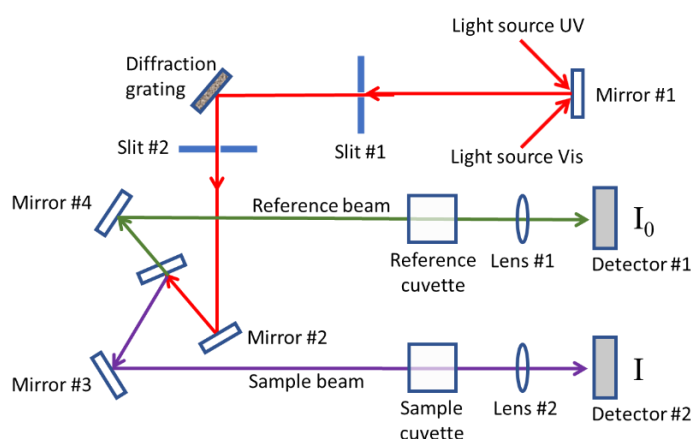


Figure 2.3. The illustration of the UV-Vis absorption spectrometer setup using a double beam method.¹⁵³

In a double-beam absorption spectrometer, the light sources (both UV and Vis light sources) were reflected by a diffraction grating to generate a single wavelength beam due to the principles of diffraction gratings.¹⁵⁴ Then the beam was split into two beams, namely the reference beam and the sample beam. Before measurements, the background scan was carried out with both cuvettes filled with solvents. This step would measure the incident spectral intensity ($I_0(\lambda)$). Then the reference beam went through the reference cuvette with pure solvent, and the intensity of the beam was recorded as the reference intensity which should be the same value as $I_0(\lambda)$. The sample beam went through the sample cuvette, and the intensity of the beam was recorded as the transmitted spectral intensity ($I(\lambda)$). Then the absorbance (A) at a specific wavelength λ of the sample could be expressed by the Lambert-Beer law as Equation 2.2:¹⁵⁵

$$A(\lambda) = \log\left(\frac{I_0(\lambda)}{I(\lambda)}\right) = \varepsilon(\lambda) \cdot c \cdot l \quad (2.2)$$

here $\varepsilon(\lambda)$ is the wavelength-dependent molar extinction coefficient, and c is the concentration of the sample. The length of the beam pathway in the sample solution is l and $l = 1$ cm in all steady-state absorption measurements.

Photoluminescence spectroscopy was introduced in this thesis to probe the radiative decay processes of the investigation target. In this thesis, fluorescence was the only emissive pathway occurring. Emission spectra were recorded in a quartz cell ($l = 1$ cm) using an FLS980 photoluminescence spectrometer (Edinburgh Instruments Ltd, the United Kingdom) in a 90° geometry. As illustrated in Figure 2.4, the light source was an ozone-free Xenon arc lamp, and the light beam was focused on a monochromator to generate the excitation beam. An excitation wavelength of 400 nm was generated and used to excite the sample. The photoluminescence emission intensity (I_F) and the excitation light source intensity (I_0) were recorded by photomultiplier tubes (PMTs). The emission spectra were recorded in a wavelength range of 420 nm to 700 nm. The optical density (OD) of the dispersions was usually set to 0.05 to avoid inner filter effects and reabsorption of emission. (However, due to the separated absorption and emission regions in CdSe/CdS dot-in-rod NRs, the OD was not necessarily to be set so low.) The photoluminescence emission intensity (I_F) at a given excitation wavelength λ_{ex} can be expressed in Equation 2.3.¹⁵⁶

$$I_F = I_0 \cdot \Phi \cdot (1 - e^{-2.303\epsilon cl}) \quad (2.3)$$

where Φ and ϵ are the PLQY and molar extinction coefficient of the sample at λ_{ex} , respectively. For the sample that optical density is less than 0.05, Equation 2.3 could be rewritten as Equation 2.4.¹⁵⁶

$$I_F = I_0 \cdot \Phi \cdot (2.303\epsilon cl) \quad (2.4)$$

Emission spectra were recorded with a function of constant wavelength. For certain data evaluation methods in this thesis (multi-Gaussian peaks fit, Stokes shift calculation...), emission spectra in energy scale were plotted. For these cases, the emission intensity ($I_F(\lambda)$) should be multiplied by λ^2/hc to keep the integrals of the spectra, where h is the Planck's constant and c is the speed of light.¹⁵⁷ To keep the calculate easy, the emission spectra were only multiplied by λ^2 when followed by normalization.

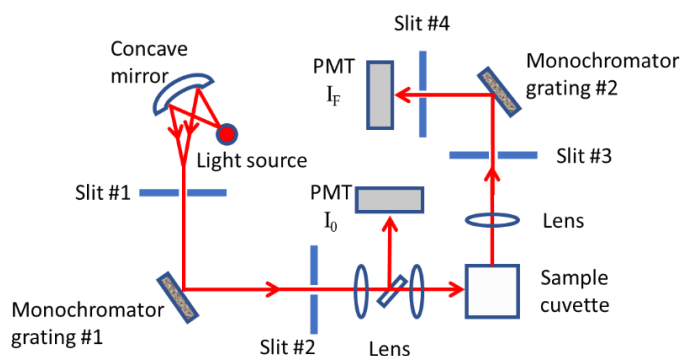


Figure 2.4. The illustration of the photoluminescence spectrometer setup in a 90° geometry.¹⁵⁸

PLQY (Φ) is a crucial property of the NRs. In principle, it describes the ratio of emitted (N_{em}) to absorbed (N_{abs}) photons. Moreover, it also describes the relationship between emissive rate constant (k_r) and non-emissive rate constants (k_{nr}).¹⁵⁶

$$\Phi = \frac{N_{em}}{N_{abs}} = \frac{k_r}{k_r + k_{nr}} \quad (2.5)$$

There are two methods to determine the PLQY of a sample. One is the absolute PLQY measurement using an integrating sphere.¹⁵⁹ By using an integrating sphere, much of the optical anisotropy is eliminated by multiple reflections on the inner surface of the integrating sphere.¹⁶⁰ The emission spectra of the sample and the solvent are measured separately to get the scattering and emission signals of the sample and solvent. Because all photons enter the integrating sphere are collected by the detector, the scattering signals of the solvent are actually the excitation and the difference between the scattering signals of the solvent and the sample ($S_{sol} - S_s$) are the absorbance of the sample. Equation 2.6 explains the calculation of absolute PLQY.¹⁵⁹

$$\Phi = \frac{E_s - E_{sol}}{S_{sol} - S_s} \quad (2.6)$$

The E_s and E_{sol} refer to the integrated emission intensity of the sample and solvent, respectively. S_s and S_{sol} refer to the integrated scattering intensity of the sample and solvent, respectively. The other method is the relative PLQY measurement using a suited standard (a known absolute PLQY with similar emission peak position as the sample at the same excitation wavelength). The relative PLQY is given as Equation 2.7, where Φ_{ref} is the known PLQY of the reference standard, I_s and I_{ref} are the spectrally integrated emission intensity of the sample and reference standard, respectively. A_s and A_{ref} are the absorbance of the sample and reference standard at the excitation wavelength, and n_s and n_{ref} are the refractive index of the solvents of the sample and reference standard, respectively.^{161, 162}

$$\Phi = \Phi_{ref} \cdot \frac{I_s}{I_{ref}} \cdot \frac{A_{ref}}{A_s} \cdot \left(\frac{n_s}{n_{ref}} \right)^2 \quad (2.7)$$

Both methods were used in this thesis, and all PLQY data displayed in this thesis will be marked with the related method.

2.2.3 Fourier transform infrared spectroscopy (FTIR)

FTIR was introduced in this thesis to monitor the ligand exchange of NRs qualitatively. In principle, infrared radiation is sent through the sample, with radiation absorbed and passed. The absorbed radiation is converted into rotational and vibrational energy by the sample. The detector

record signal as a spectrum of the molecular vibrations shown in Figure 2.5, including symmetric stretching, asymmetric stretching, rocking, scissoring, wagging, and twisting.

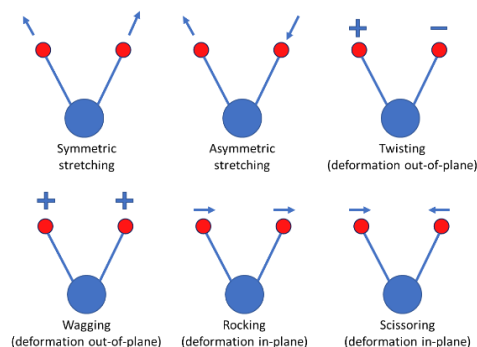


Figure 2.5. The illustration of the vibration modes in FTIR.¹⁶³

IR spectra were recorded using a Bruker Tensor 27 system equipped with a mid-IR source (4000 to 600 cm^{-1}) with attenuated total reflectance (ATR) mode, as shown in Figure 2.6. The sample was placed directly on a CaF_2 substrate (1 cm \cdot 1 cm). After drying the sample in vacuum, the substrate was rotated, and then the sample side was placed on the small crystal spot of the detector. Then the arm was rotated over and turned down to press the sample down onto the crystal face to get better contact. The IR beam penetrates about 60 μm into the sample. The background of the CaF_2 substrate was always scanned before the measurements of the samples.

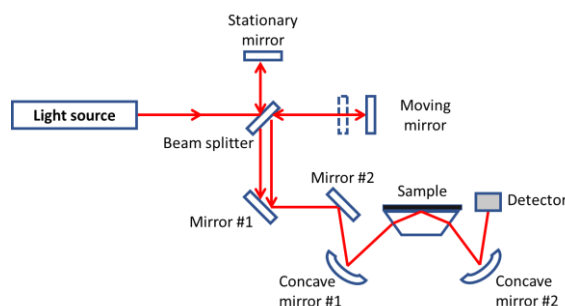


Figure 2.6. The illustration of the FTIR setup in ATR mode.¹⁶⁴

2.2.4 Pump-probe transient absorption spectroscopy

The pump-probe transient absorption (TA) measurements were conducted in this thesis to probe the fast excited state processes, together with the deactivation processes of these excited states. The experimental instruments were displayed in Figure 2.7. The 780 nm fundamental generated from a Ti:Sapphire amplifier (Legend-Elite, Coherent Inc., the USA) with a repetition rate of 1 kHz (pulse duration \approx 30 fs) was split into two beams with a beam splitter. One portion of the beam was used to generate the pump beam by the second harmonic generation (SHG) of 390 nm using a bariumborate (BBO) crystal.¹⁶⁵ The other portion of the 800 nm fundamental was used

for probe beam generation. This portion of the fundamental was focused on a constantly rotating CaF₂ crystal to generate white light. A filter was placed before the CaF₂ crystal to lower the intensity of the fundamental in case of overheating. The CaF₂ crystal holder needs to be rotating during the white light generation to prevent the crystal from degrading. A spherical mirror is placed before the supercontinuum generation to fine-tune the white-light properties. The probe beam was then split into two parts. One part was focused by a concave mirror and used to probe the sample, while the other part was used to act as the reference beam in the data collection step.

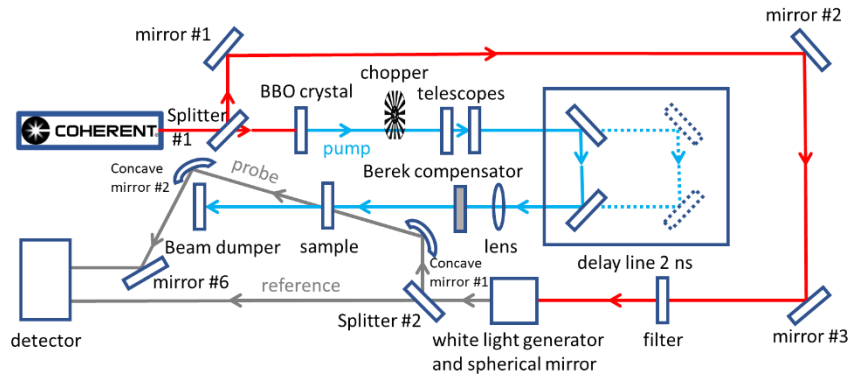


Figure 2.7. The illustration of the pump probe transient absorption setup.

The relative angle between the pump and probe beam was set to the magic angle (54.7°) to avoid artifacts in the signal because of the rotational diffusion. A Berek compensator was placed in the pump path to achieve this. The pump and probe beams were focused at the sample placed in a 1 mm inert cuvette where measurements were performed without oxygen with a small angle so that the pump beam could be blocked while the probe beam and the reference beam were recollimated and sent parallelly to the detection system (Pascher Instruments, AB, Sweden) consisting of a spectrograph (Acton, Princeton Instruments, the USA) with a double-stripe diode array detector. The readout rate of the detector was the same as the laser repetition rate.

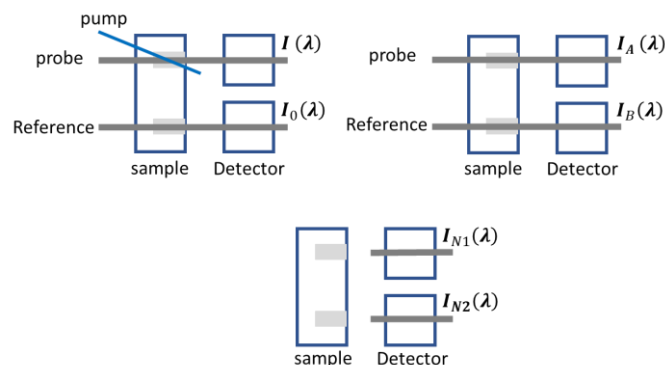


Figure 2.8. The illustration of the detecting system of the transient absorption setup. $I(\lambda)$ and $I_0(\lambda)$ refer to pump-on signal and reference signal. $I_A(\lambda)$ and $I_B(\lambda)$ refer to pump-off signal and reference signal.

$I_{N1}(\lambda)$ and $I_{N2}(\lambda)$ refer to background noise signal measured without beam signal.

The basic principle of this pump-probe TA spectroscopy is explained briefly in Equation 2.8. The differential optical density (ΔAbs) can be calculated by the optical density of the sample with the pump ($Abs_{pump-on}$) minus the optical density of the sample without the pump ($Abs_{pump-off}$).

$$\Delta Abs = Abs_{pump-on} - Abs_{pump-off} \quad (2.8)$$

However, when the ΔA is calculated in a practical measurement, more signals need to be measured. The setup introduced in this thesis used a two-pulse method with a mechanical chopper that cut off every second laser pulse. As displayed in Figure 2.8, when the sample was pumped, the probe beam intensity was recorded as $I(\lambda, \Delta t)$ and the reference beam was recorded as $I_0(\lambda, \Delta t)$. When the sample was unpumped, the probe beam intensity and the reference beam intensity were recorded as $I_A(\lambda, \Delta t)$ and $I_B(\lambda, \Delta t)$, respectively. Additionally, signal intensities were recorded when the probe and reference beam was blocked as $I_{N1}(\lambda)$ and $I_{N2}(\lambda)$, respectively, and substrated as the ambient noise. The measurements with different delay times between the pump and probe beam were achieved by moving the optical delay stage (~ 2 ns) in the pump beam path. The wavelength and delay time dependant differential absorbance $Abs(\lambda, \Delta t)$ could then be expressed as Equation 2.9.¹⁶⁶

$$Abs(\lambda, \Delta t) = \log \left(\frac{I_0(\lambda, \Delta t) - I_{N2}(\lambda)}{I(\lambda, \Delta t) - I_{N1}(\lambda)} \cdot \frac{I_B(\lambda, \Delta t) - I_{N2}(\lambda)}{I_A(\lambda, \Delta t) - I_{N1}(\lambda)} \right) \quad (2.9)$$

To obtain a TA dataset, the sample was measured for at least eight scans (one scan refers to the measurement from ~ -50 ps to ~ 2 ns). The obtained dataset was a 2D matrix with one dimension of time and one dimension of wavelength. The investigation of the temporal evolution at chosen wavelengths $\Delta Abs_\lambda(t)$ delivered the kinetic information of the excited charges. The inspection of $\Delta Abs_t(\lambda)$ revealed the spectral information at chosen delay times. For the main investigation target in this thesis, the kinetic information of NRs at a given wavelength was fitted by applying a sum of exponential functions in Equation 2.10:

$$\Delta Abs_\lambda(\Delta t) = \sum_i A_{fi} e^{\frac{-\Delta t}{\tau_{fi}}} + \sum_i A_i e^{\frac{-\Delta t}{\tau_i}} + constant \quad (2.10)$$

A_{fi} and τ_{fi} refer to the amplitude and time constant of signal formation processes. A_i and τ_i refer to the amplitude and time constant of signal decay processes. For the research objects NRs in this thesis, the formation signals owned positive amplitudes indicating the electron population on the CB while the decay signals exhibited negative amplitudes referring to the electron depopulation on the CB. The instrument response function (IRF) was negligible because during the data analysis, the first 100 fs data was not regarded due to the coherent artefact signals as a result when two short pulses interact in a medium with polarizability.¹⁶⁷ The pulse duration was determined to be 81 fs by cross-correlation measurement of the pump and probe. Global analysis

methods were introduced to give a better quantitative description of the obtained 2D time-resolved datasets. The global analysis in this thesis was always applied at the ground state bleach of the associated material, centered at the minimum signal wavelength with ± 5 nm range using Equation 2.8 but sharing the time constants (τ_{fi} , τ_i) when global fitting. After obtaining the kinetic profile defined time constant (τ_{fi} , τ_i), the amplitudes of each time constant were plotted with the errors against the wavelength, namely the decay associated spectrum (DAS). The absorption spectra were taken before and after TA measurement to make sure there was no degrading during the measurement.

2.2.5 Time-resolved emission spectroscopy

Time-resolved emission spectroscopy probes the emissive states of the research object. In this thesis, the emission decay profiles were measured using a Hamamatsu streak scope C4334 (Hamamatsu Photonics, Japan) in photon counting mode. The time window was 20 or 50 ns. As shown in Figure 2.9, the sample was held in a 1 cm cuvette with OD ≈ 0.3 at 400 nm and excited with a frequency-doubled output of a Ti:Sapphire laser (Tsunami, Newport Corporation, the USA) at around 380 nm at a repetition rate of 400 kHz after passing a pulse selector (model 3980, Newport Corporation, the USA). The emissions from the sample were detected by a Chromex 250IS 3 imaging spectrograph (Chromex is now part of Bruker Optik GmbH, Germany). Data were processed with the HPDTA software delivered with the system to get the two-dimensional (time and wavelength) emission decay profiles.¹⁶⁸ Then, the spectrally integrated single kinetic profile was fitted either mono- or bi-exponential decay with the program DecayFit.¹⁶⁹ The IRF of this system was determined by a piece of glass.

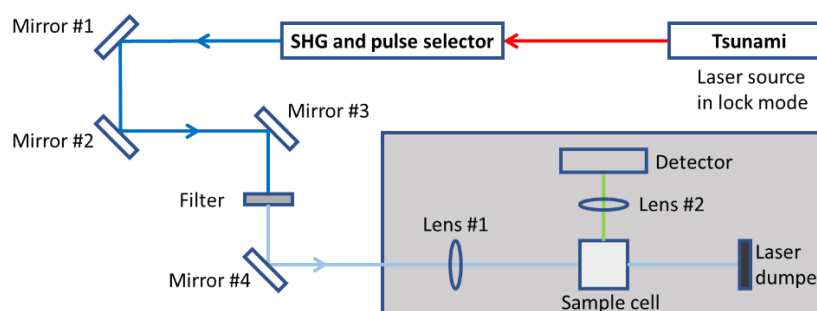


Figure 2.9. The illustration of the time-resolved emission spectroscopy setup. The detector, spectrograph and streak camera were included in the “Detector” in the illustration.

The working principle of the streak camera detector was illustrated in Figure 2.10. The light being measured went through a slit and was formed by the lens into a slit image on the photocathode of the streak tube. The incident light on the photocathode is converted into a number of electrons proportional to the intensity of the light. The electrons then went through a pair of accelerating

electrodes, where they were accelerated and bombarded against a phosphor screen. High voltage was applied to the sweep electrodes at a timing synchronized to the incident light. The electrons were swept from top to bottom at this stage. During the high-speed sweep, the electrons, which arrived at slightly different times, were deflected in slightly different angles in the vertical direction and then entered the micro-channel plate. After the electrons passed the micro-channel plate, they were multiplied thousands of times. They arrived at the phosphor screen finally and were converted again into light. On the phosphor screen, the phosphor image corresponding to the optical pulse which was the earliest to arrive was placed in the most upper position, the rest were placed in the order of the arriving time. The vertical direction on the phosphor screen served as the time axis. The brightness of the phosphor images was proportional to the intensity of the respective incident optical pulses. The position in the horizontal direction of the phosphor image corresponded to the horizontal location of the incident light. In this way, the streak camera could be used to convert changes in the temporal and spatial light intensity of the light being measured into an image showing the brightness distribution on the phosphor screen.

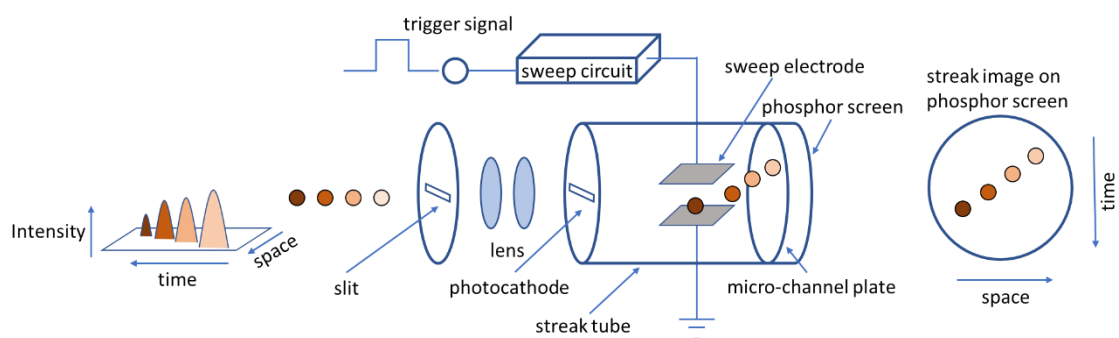


Figure 2.10. The illustration of the working principle of the streak camera.

CHAPTER 3.

CdSe/CdS dot-in-rod and inside-out NRs

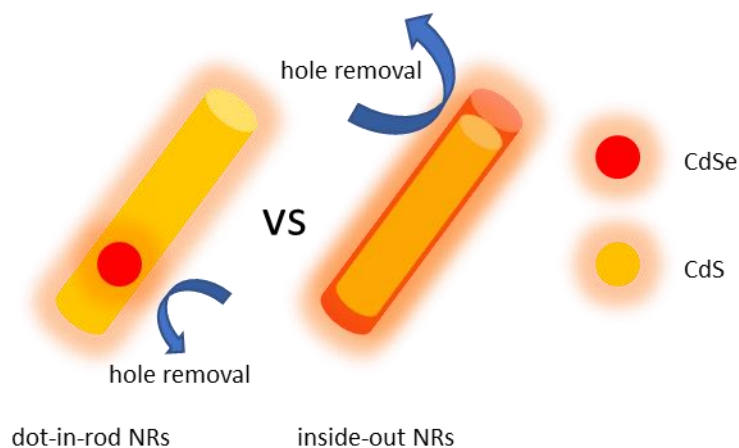


Figure 3.1. Illustration of the dot-in-rod and inside-out NRs with their possible mechanisms of hole removal.

The CdSe/CdS dot-in-rod NRs has been successfully synthesized by the “seeded-growth” method since the reports in 2007.^{134, 139} The dot-in-rod NRs can be quasi-Type II aligned with core size less than 2.8 nm¹¹⁵ and have naturally separated electrons and holes across the heterostructure interface, prolonging their intrinsic lifetime of charge separation state by reducing radiative recombination rate.²⁴ For typical quasi-type II aligned dot-in-rod NRs, upon light excitation, the generated electron will move to the conduction band shared by both CdSe core and CdS rod where the electron wave function spreads along the rod while the hole will be localized on the valences band of the CdSe core. With an external electron donor, the hole will be able to be removed to prevent the NRs from being oxidized in order to reduce the photooxidation of these NRs. However, as the holes are confined deeply in the core part, the nature and location of the holes in the dot-in-rod NRs build up limitations for the holes to be removed easily by external electron donors in the colloidal solution. In previous reported work, the dot-in-rod CdSe/CdS NRs were etched to expose the CdSe component to the surface to investigate the hole transfer rate, and the results showed that the rate was increased 3-fold upon etching.¹⁷⁰ Alternative morphologies were also introduced to expose hole trapping domains to the environment where the holes could be potentially removed by the electron donors.¹⁴⁷ So, in addition to the “seeded growth” of the dot-in-rod NRs, the high energy tip surfaces of wurtzite NRs can be readily modified with another material to produce various nanobarbell structures. In 2006, *Bawendi* and co-workers synthesized type II CdSe/CdTe nanobarbells by growing CdTe dots at the tips of pre-formed CdSe NRs.¹⁷¹ Later, *Zamkov* and co-workers applied similar procedures and prepared type II CdS/ZnSe nanobarbells.¹⁷² Unlike the

dot-in-rod NRs, in these nanobarbells NRs, both hole trapping and electron trapping domains are exposed to the surrounding medium, which may facilitate the extraction of both electrons and holes.

In this respect, in cooperation with Prof. *Lilac Amirav*, Technion, Haifa, we started to explore a new type of structure, which can be regarded as, compared to the CdSe/CdS dot-in-rod NRs as an inverted structure, which meant that the CdS were used as the core and CdSe were introduced as the shell. In the *Amirav* group a series of structures with a novel CdSe/CdS inverted structure (CdS rod as the core, CdSe as the shell, namely the inside-out NRs) was synthesized.¹⁷³ In this chapter, the optical properties and the charge carrier dynamics of the inside-out NRs will be investigated along with their counterparts, the dot-in-rod NRs. The steady-state measurements will be introduced first to investigate the ground state electronic structure of the inside-out NRs, followed by the time-resolved measurements which will investigate the recombination dynamics of the excited inside-out structures.

3.1 Characterization of the inside-out structure

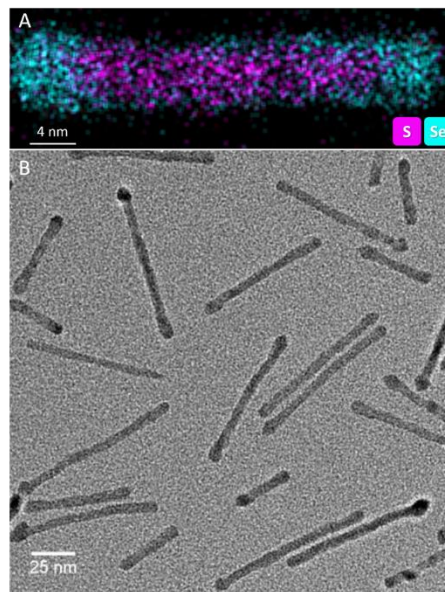


Figure 3.2. The (A) EDS and (B) TEM images of the inside-out NRs. The elements of S and Se was marked as fake colors, respectively magenta and cyan in the EDS image. (Images were taken by our cooperation partners in Israel and displayed here with their permission.)

Due to the inverted nature compared to the CdSe/CdS dot-in-rod NRs, these novel NRs was named as the CdSe/CdS inside-out NRs in this chapter. (In this chapter, the materials were always CdSe and CdS, so only “dot-in-rod NRs” and “inside-out NRs” were used for short.) The aim of this novel inside-out NRs was to lead holes to be localized on the outer CdSe surface of the rods in order for the holes to be removed easier than the dot-in-rod NRs where holes would be localized in the core part of the rods after light excitation. In this chapter, basic optical properties in comparison to the dot-in-rod NRs were studied applying steady-state absorption and photoluminescence spectroscopy. And transient

absorption spectroscopy was introduced to investigate the exciton dynamics of the inside-out NRs. The inside-out NRs were characterized by TEM and energy dispersive spectroscopy (EDS), as shown in Figure 3.2. The length of this inside-out NRs was 58.4 nm, provided by our partners. And the diameter was about 5.5 ± 0.5 nm in the middle part of the rods but slightly bigger at two ends as 7.3 ± 0.8 nm. (The width was determined by us using software ImageJ v1.52a.)

The EDS analysis revealed the distribution of CdS and CdSe in the structures, as shown in Figure 3.2. The part of the element S was mainly in the center of the rod indicating that CdS part was in the center of this structure while the element Se was distributed mainly on the two ends and the outside surface of the rod indicating CdSe part was concentrated at two ends forming bulbs and also covered outside the CdS part as thin shell. This would result in a large size distribution of CdSe composite in this novel inside-out NRs. And this would be discussed in the next section.

3.2 Steady-state measurements and discussion

3.1.1 Steady-state absorption measurements and discussion

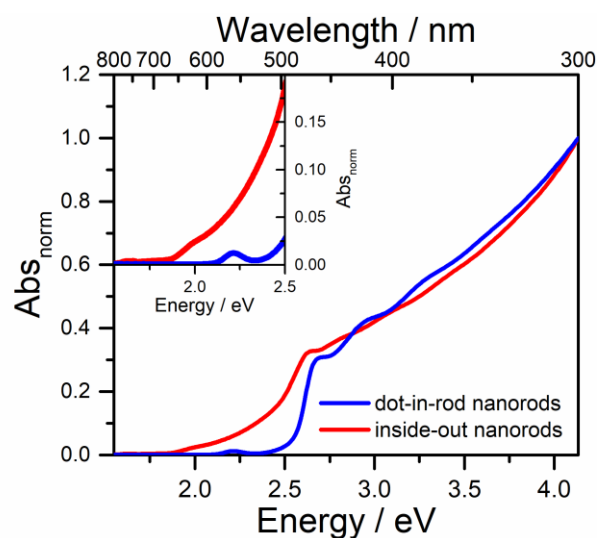


Figure 3.3. The absorption spectra of the dot-in-rod and inside-out NRs in toluene normalized as 1 at 4.13 eV (300 nm). Inset was the CdSe part of both NRs.

To explore the electronic structure of a novel nanostructure, steady-state UV/Vis absorption would always be the first option. By comparing with the state-of-the-art dot-in-rod NRs, the general behaviors of this novel inside-out NRs could be obtained. In Figure 3.3, the normalized absorption spectra of the dot-in-rod and inside-out NRs were displayed. The inside-out NRs showed an absorption feature at similar position as the dot-in-rod NRs at 2.69 eV (460 nm), which could be related to the CdS first excitonic absorption peak stemming from the CdS rod

shaped part of the structures. However, unlike the small peak at around 2.21 eV (565 nm) related to the first excitonic absorption peak of the CdSe core in the dot-in-rod NRs, the absorption of the CdSe shell in the inside-out NRs tailed from around 2.58 eV (480 nm) to 1.77 eV (700 nm). And the long tail feature compared to dot-in-rod NRs was consistent with reported results when CdS quantum dots and CdS NRs were coated with CdSe shell.^{91, 174} No defined peak as for the dot-in-rod NRs for the CdSe core was presented in the inside-out NRs reflecting the less defined structure of the CdSe shell with a large size distribution of shell thicknesses or particle sizes.

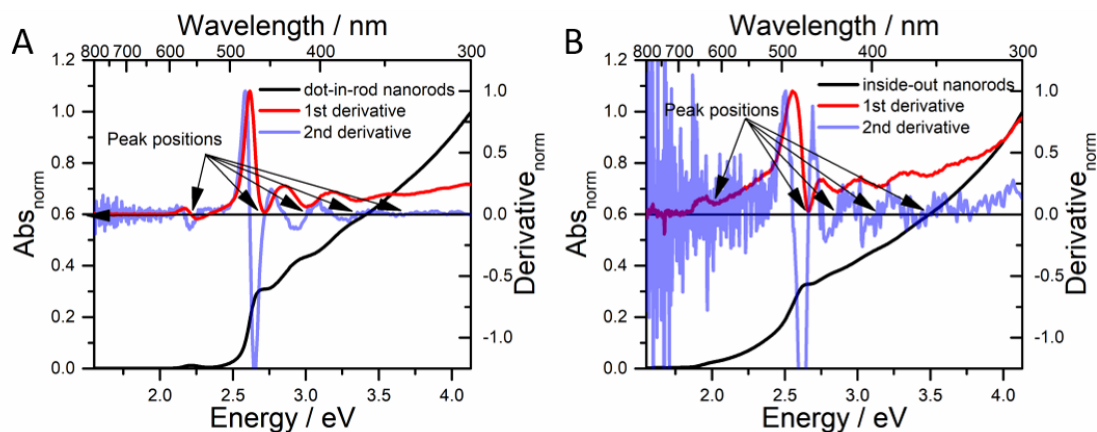


Figure 3.4. The absorption spectra of the (A) dot-in-rod and (B) inside-out NRs in toluene with their 1st and 2nd derivatives. The absorption spectra were normalized as 1 at 4.13 eV (300 nm). The 1st and 2nd derivatives were normalized as 1 at the peak around 2.65 eV for better illustration.

In order to obtain a possible correlation with the exciton energy levels of the dot-in-rod and inside-out NRs and their absorption spectra, each absorption spectrum was fitted with a sum of Gaussian peaks, with each peak corresponding to the absorption of a particular exciton level. The spectral position of the maxima of the Gaussian curve was extracted from the 1st and 2nd derivatives of the corresponding absorption spectrum, as shown in Figure 3.4. The normalized absorption spectrum of the dot-in-rod NRs was displayed in Figure 3.4A, together with its 1st and 2nd derivatives. For individual peak, as the small peak at around 2.20 eV, which corresponded as the first excitonic absorption peak of the CdSe core, the position where the 1st derivative is zero and the 2nd derivative is below zero meant the local maximum, also can be called as a peak, is here. For stacked multiple peaks, as the absorption spectrum from 2.50 eV to 4.13 eV, the curve was always increasing, meant that there would be no zero points in the 1st derivative but only local minimum. Then the peak position was determined by where the 2nd derivative was zero while changing from negative to positive. With the help of these peak position values as the initial fitting parameters, the multiple Gaussian peaks fit then could be performed. (An additional peak 6 was introduced to complete the fit of the whole spectra in displayed scale.) With the knowledge

above, the initial fitting parameters were also determined from the absorption spectrum of the inside-out NRs with its 1st and 2nd derivatives in Figure 3.4B.

The results of this fitting procedure, including the experimental absorption spectra of both NRs and the absorption spectra of the samples reconstructed from a sum of multiple Gaussian peaks as named the cumulative curve, were shown in Figure 3.5. The absorption spectrum showed no peaks before 2.00 eV for the dot-in-rod NRs, so the fitting range of the dot-in-rod NRs was determined from 2.00 eV to 4.13 eV. The absorption spectrum of the inside-out NRs showed tailing to 1.50 eV, so the fitting range of the inside-out NRs was from 1.50 eV to 4.13 eV. Together with the detailed fitting parameters in Table A1 (in the Appendix at the end of this thesis), both fits showed adjusted R-square larger than 0.9999. (There should be a peak at around 2.47 eV, which refers to the slightly bigger part of the interface between the core and the shell in the dot-in-rod NRs.¹⁴⁵ This peak makes little sense in this comparison method and is negligible in this chapter.) The CdSe part showed its 1S transition in Figure 3.5C and 3.5D at 2.22 eV and 2.10 eV as peak 1 for the dot-in-rod and inside-out NRs, respectively. The red shift of the absorption band of CdSe 1S transition in the inside-out NRs compared to the same transition related absorption band in the dot-in-rod NRs reflected a decrease in the quantum confinement energy due to a larger CdSe volume or less defined structure compared to the CdSe core in the dot-in-rod NRs. However, due to the potential large distribution of CdSe part in the inside-out NRs, the corresponding absorption peak at 2.10 eV, unlike the one in the dot-in-rod NRs, could not be nicely described by only one Gaussian peak. Although the first excitonic absorption peak of CdSe appears at 2.20 eV and 2.10 eV respectively for the dot-in-rod and inside-out NRs were nicely assigned, the other excitonic levels of CdSe would also make contributions at higher energy scale. For the dot-in-rod NRs, the contribution of CdSe in absorbance above 2.50 eV was less than 1% and it was negligible.¹⁷⁵ But for the inside-out NRs, the contribution of CdSe shell in absorbance above 2.50 eV was much larger due to large volume of CdSe, so the contribution of CdSe above 2.50 eV is not negligible in this case. The peak 2 to 6 in Figure 3.5A reflected the different exciton levels (2.67 eV, 2.84 eV, 3.17 eV, 3.57 eV and 4.46 eV) of the CdS part in the dot-in-rod NRs¹⁴⁵ while the peak 2 to 6 in Figure 3.5B did not reflect the exciton levels of either only CdS or only CdSe but reflected the combination of different exciton levels (2.61 eV, 2.76 eV, 2.80 eV, 3.48 eV, 4.92 eV) contributed by both CdSe part and CdS part in the inside-out NRs because of the contribution of CdSe part in higher energy range in much more pronounced comparing to the dot-in-rod NRs.

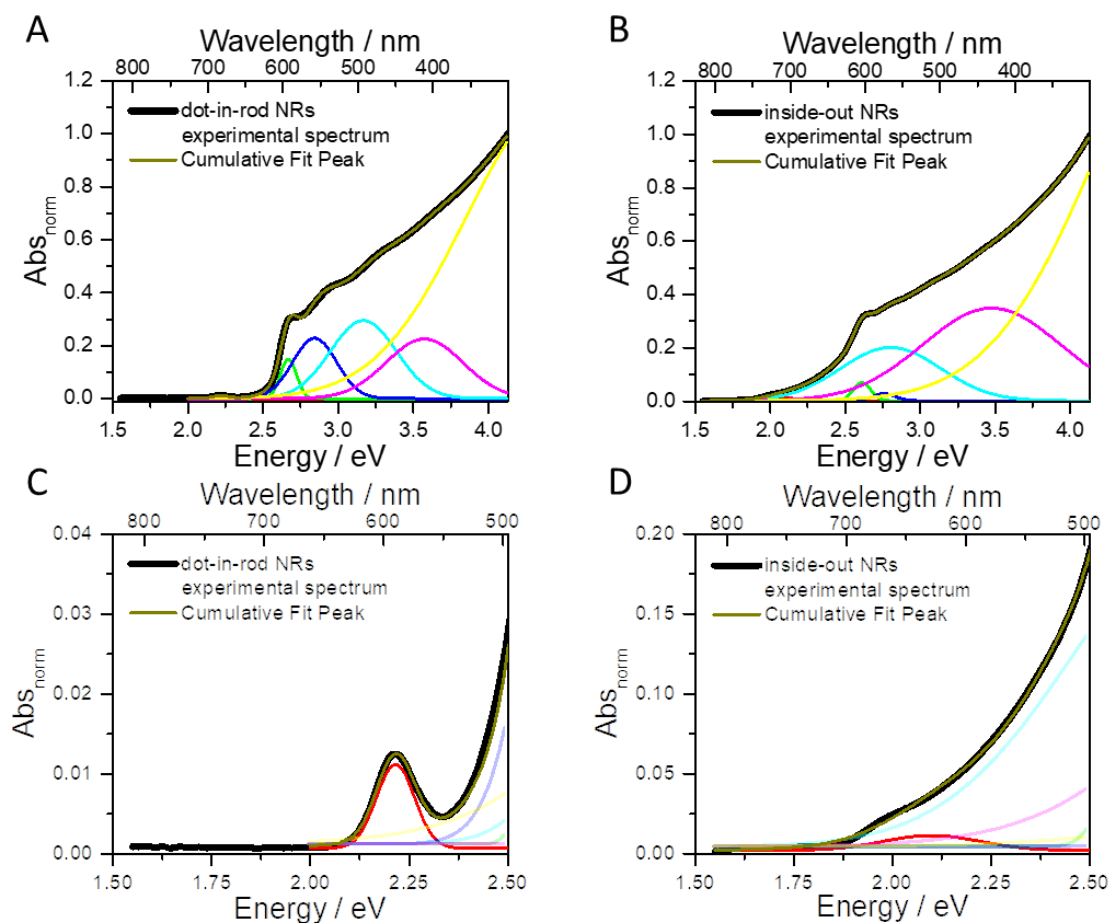


Figure 3.5. The multi-Gaussian peaks fit of the absorption spectra of (A) the dot-in-rod and (B) inside-out NRs in toluene normalized as 1 at 4.13 eV (300 nm) including details on the CdSe part absorption peak fit of (C) the dot-in-rod and (D) inside-out NRs.

3.1.2 Steady-state emission measurements and discussion

From the lowest excitonic state photoluminescence was observed. Excited at 400 nm, the inside-out NRs showed an emission peak at around 1.91 eV (650 nm) related to the band gap emission of CdSe, comparing to the dot-in-rod NRs where the band gap emission peak showed at 2.18 eV (570 nm), as shown in Figure 3.6. This agreed with the first excitonic absorption peak position of CdSe part in the absorption spectra. This also agreed with the results from multi-Gaussian peaks fit of the absorption spectra, the Gaussian peak referred to the first excitonic absorption peak of CdSe part in the inside-out structure was red shifted to around 2.10 eV compared to the CdSe part at 2.22 eV in the dot-in-rod structure. The emission peak of the inside-out NRs was closer to the bulk band gap of CdSe 1.74 eV indicating a larger CdSe volume in the inside-out NRs¹⁷⁶ which agreed with the confinement argument in section above.

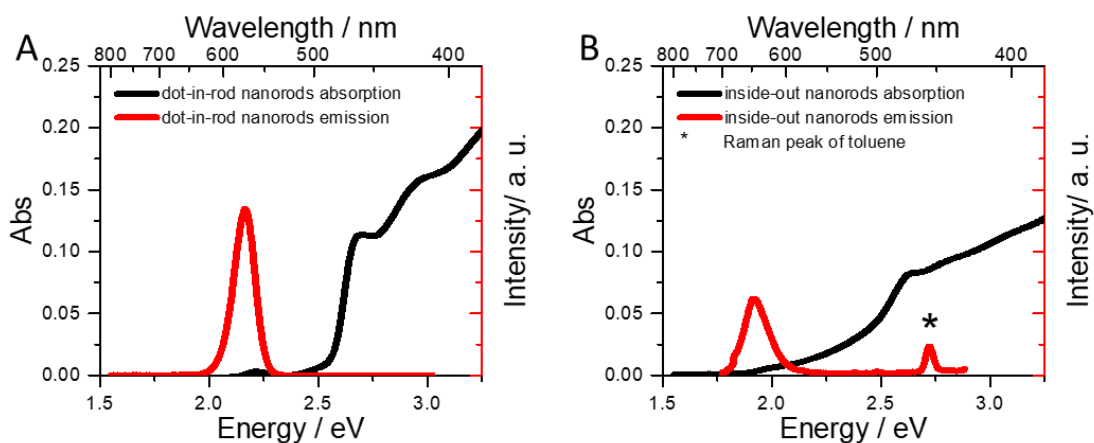


Figure 3.6. The absorption and emission spectra of the (A) dot-in-rod and (B) inside-out NRs in toluene with an excitation wavelength of 400 nm. The sharp peak marked with an asterisk referred to the Raman band of toluene.

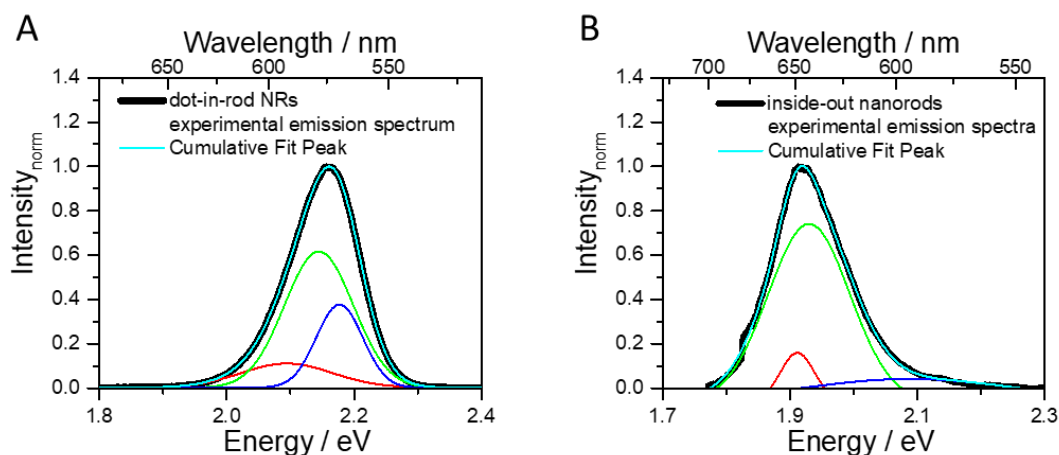


Figure 3.7. The multi-Gaussian peaks fit of the emission spectra of (A) the dot-in-rod and (B) inside-out NRs in toluene. Emission spectra were normalized as 1 at emission intensity maximum.

The line width of these emission peaks was determined by the width of half-maximum which was 0.14 eV for the inside-out NRs and 0.11 eV for the dot-in-rod NRs. Apparently, the dot-in-rod NRs had a narrower size distribution of CdSe part resulting in a narrower emission peak. To further probe this, similar multi-Gaussian peaks fit was introduced here on the emission spectra of both NRs in Figure 3.7 and associated fitting parameters were displayed in Table A2 in the Appendix. Only three Gaussian peaks were needed for the emission spectrum of the dot-in-rod NRs to reach the adjusted R-square 0.9998 and also three Gaussian peaks were needed for the emission spectrum of the inside-out NRs to reach 0.9989.

In order to understand the emission features of the dot-in-rod and inside-out NRs, a short background should be introduced. The surface states of CdSe/CdS nanocrystals could be

classified into two species. One is hole trap states caused by the unpassivated Se and S site or surface ligands.¹⁷⁷⁻¹⁸¹ The another is the shallow electron trap states associated with the surface Cd ions or surface ligands.¹⁸²⁻¹⁸⁴ Base on the reported assignments of different peaks^{185, 186}, the blue peak (2.17 eV) in Figure 3.7A could be referred to the intrinsic emission of the dot-in-rod NRs and the green peak (2.12 eV) could be explained by the shallow electron trap related emission, as shown in Figure 3.7A. (The word “shallow” and “deep” in this thesis referred to the energetic position to the band edge. Typically, carriers in the traps with shallow potential (potential depths ~ 25 meV) can delocalize again at room temperature and contribute to the band-edge PL, while the carriers trapped in deep potentials hardly delocalize.¹⁸⁶ These traps further refer to the radiative and non-radiative recombination processes, respectively. Worth mentioning, both of shallow and deep trap could be existed at the same time, which means that even observable trap state related emission peak could be seen in the spectrum, the deep trap could still exist. It was the same the other way around, if related emission peak were not presented, either deep trap or perfect surface passivation could happen. But since there was nearly no way to perfectly passivate semiconductor nanocrystals, the deep trap resulting in non-radiative recombination process would always be a more reasonable explanation in this case.) There was a broad weak red peak at lower energy range referring to the shallow hole trap related emission because the Se site on the CdSe core was probably not 100% passivated with CdS shell in the dot-in-rod NRs due to stacking faults.¹⁸⁷ And the hole trap state on the CdS shell was unobservable here because they were not deep enough to compete with the hole localization processed. (Similar peak assignments could also be applied on the CdSe quantum dots which was used as the core. Data were not shown here.)

When looking at Figure 3.7B, the blue peak (2.09 eV) referred to the intrinsic emission of the CdSe part in the inside-out NRs which was broad and weak due to large size distribution of the CdSe part while the green peak (1.93 eV) and red peak (1.91 eV) referred to the shallow electron trap related emission and shallow hole trap related emission, respectively. The shallow hole trap related emission (red peaks) showed very distinguished intensity and width indicating the surface states strongly influenced these emission properties which meant the hole trap was more pronounced in the inside-out NRs. This could be explained by using CdSe material as shell resulting in large amount of exposed Se sites. As mentioned above, in the dot-in-rod NRs, the hole trap state in CdS shell was not deep enough to have strong influence on the emission properties comparing to the inside-out NRs.

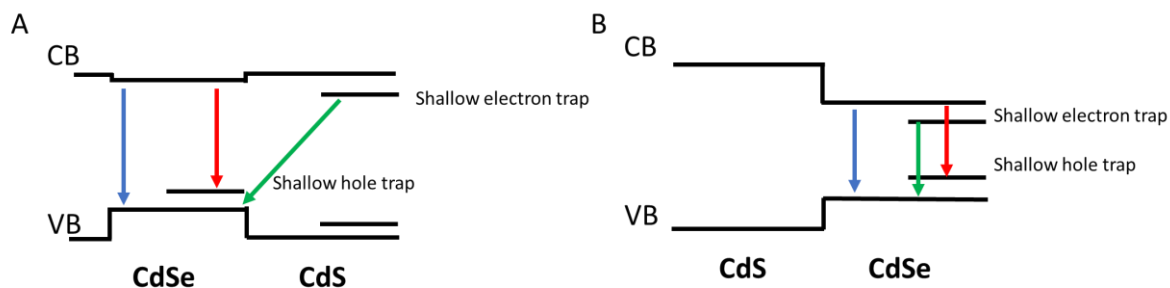


Figure 3.8. The proposed energy band diagrams of (A) the dot-in-rod and (B) inside-out NRs. The color of the recombination processes refer to the assignment of different Gaussian peak deconstructed from the emission peak.

The electron shallow trap related emission in both structures (the green peaks) shared almost the same width 0.13 eV and 0.14 eV, respectively, and nearly identical intensity indicating electron trap states were comparable between the inside-out NRs and dot-in-rod NRs. This could be explained by the passivation of TOPO which attached on the Cd site with similar coverage ratio on both NRs. The intrinsic emission peak (blue in Figure 3.7B) in the inside-out NRs was much broader than that in the dot-in-rod NRs (blue in Figure 3.7A). This would be another strong indication of the larger size distribution of CdSe part in the inside-out structure. Based on the discussion above, the proposed energy diagrams of both NRs were displayed in Figure 3.8.

The absolute PLQY of the in dot-in-rod NRs and inside-out NRs were calculated as 0.60 ± 0.02 and 0.02 ± 0.02 , respectively. This could be also explained by the more pronounced surface defects in the shell of the inside-out NRs due to surface states resulting in non-radiative recombination process. The Stokes shift (determined by the difference between the first excitonic absorption peak of CdSe part and intrinsic emission peak in both nanostructures¹⁸⁸) was 0.09 eV for the inside-out NRs and 0.04 eV for the dot-in-rod NRs due to energy loss through electron vibrational relaxation.

3.2 Transient absorption measurements and discussion

3.2.1 Transient absorption measurements of the dot-in-rod NRs and discussion

The ultrafast electron behaviors were investigated by ultrafast transient absorption spectroscopy. Before the data interpretation and discussion of the inside-out NRs, the behaviors of the dot-in-rod NRs should be introduced. The power density of the pump pulse at the sample position was adjusted to 0.1 W cm^{-2} , low enough to ensure measurements in the 1-exciton-per-nanorod and below regime.³³ The TA spectra and kinetic information of the dot-in-rod NRs were displayed in Figure 3.9. The ground state bleach of the CdS part (B1) centered at 458 nm (2.71 eV)

corresponded to the first excitonic absorption peak of CdS at 2.67 eV and the ground state bleach of the CdSe part (B2) centered at 556 nm (2.23 eV) related to the first excitonic absorption peak of CdSe at 2.22 eV and also the emission peak of the dot-in-rod NRs.^{24, 92} The kinetic information of B1 (single kinetic at 458 nm) and B2 (single kinetic at 556 nm) are displayed in Figure 3.9B and both kinetics showed signal formation and decay section, and could be described using Equation 2.8 introduced in chapter 2.

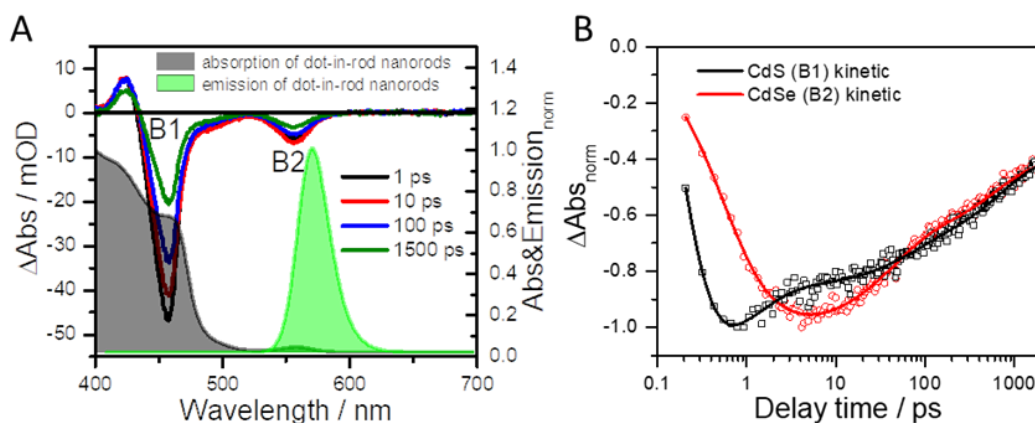


Figure 3.9. (A) The TA spectra of the dot-in-rod NRs in toluene excited at 390 nm probed with white light together with the absorption and emission spectra (excited at 400 nm) of the dot-in-rod NRs and (B) the single kinetics of CdS and CdSe normalized to -1 at the kinetical minimum, 458 nm and 556 nm, respectively.

Detailed information on the time components could be obtained by single kinetic and global fit which were also introduced in chapter 2. The time components displayed in this chapter were all obtained from global fit if not otherwise indicated. The kinetic of B1 showed one fast signal formation time component around 0.2 ps referred to cooling, the second time component was a fast decay component around 1.3 ps indicated an electron depopulation process on the CdS CB associated with the electron movement from the CB of CdS to the CB of CdSe.⁹² The third and fourth time components were part of the decay signal related to the recombination processes and were around 52 ps and 683 ps, respectively. The end of this kinetic was not decayed to zero at the end of the measurement indicating there were still further processes (like slow recombination processes) at the end of the 1700 ps delay time. The kinetic of B2 also showed a fast signal formation time component around 0.6 ps referred to the cooling of the hot electron. Unlike the second time component in the B1 kinetic, the second time component in the B2 kinetic was in the signal formation and around 2.1 ps. This indicated an electron population process on the CB of CdSe which could be explained by the same process of electron movement on CB appeared in the B1 kinetic. Furthermore, this process could be explained by the Coulombic interaction introduced by hole localization at the CdSe core. The third and fourth time components were both part of the decay signal associated with recombination processes. And these recombination

processes were not finished at the end of the delay time since the signals were not decayed to 0 at the end of the delay time. This could be quantified by the single kinetics of the B1 and B2 in Figure 3.9B, the ΔAbs_{norm} value at the end of delay time was around -0.4 due to more slow recombination processes. Details on the global fit and DAS could be found in Figure 3.10 and Table 3.1.

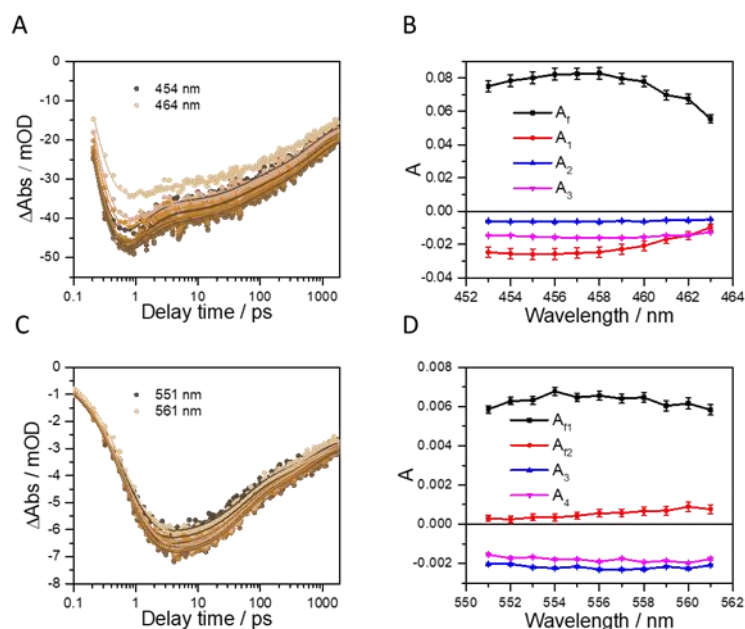


Figure 3.10. The global fit of the kinetics in the dot-in-rod NRs, (A) 10 nm scale centered at CdS bleach signal minimum 458 nm and (C) 10 nm scale centered at CdSe bleach signal minimum 556 nm. The DAS of global fit of (B) CdS and (D) CdSe parts, respectively.

Table 3.1. Fitting parameters of the TA kinetics of the dot-in-rod NRs (global fit of 10 nm scale centered at each bleach signal minimum and single kinetic fit displayed in Figure 3.9B). * The offset and amplitudes with associated errors of the global fit were displayed in DAS in Figure 3.10.

	Global fit*		Single kinetic fit	
	CdS	CdSe	CdS	CdSe
Adj. R-Square	0.981	0.988	0.980	0.989
y_0	–	–	-0.40 ± 0.02	-0.41 ± 0.01
τ_{f1} (ps)	0.2 ± 0.1	0.6 ± 0.1	0.2 ± 0.1	0.5 ± 0.1
A_{f1}	–	–	2.57 ± 0.42	0.81 ± 0.12
τ_{f2} (ps)	–	2.1 ± 0.5	–	1.8 ± 0.7
A_{f2}	–	–	–	0.24 ± 0.14
τ_1 (ps)	1.3 ± 0.1	–	1.3 ± 0.3	–

A ₁	–	–	-0.25 ± 0.04	–
τ_2 (ps)	52 ± 3	50 ± 1.3	58 ± 11	41 ± 3
A ₂	–	–	-0.14 ± 0.02	-0.31 ± 0.01
τ_3 (ps)	683 ± 32	683 ± 35	731 ± 125	611 ± 79
A ₃	–	–	-0.32 ± 0.01	-0.28 ± 0.01

3.2.2 Transient absorption measurements of the inside-out NRs and discussion

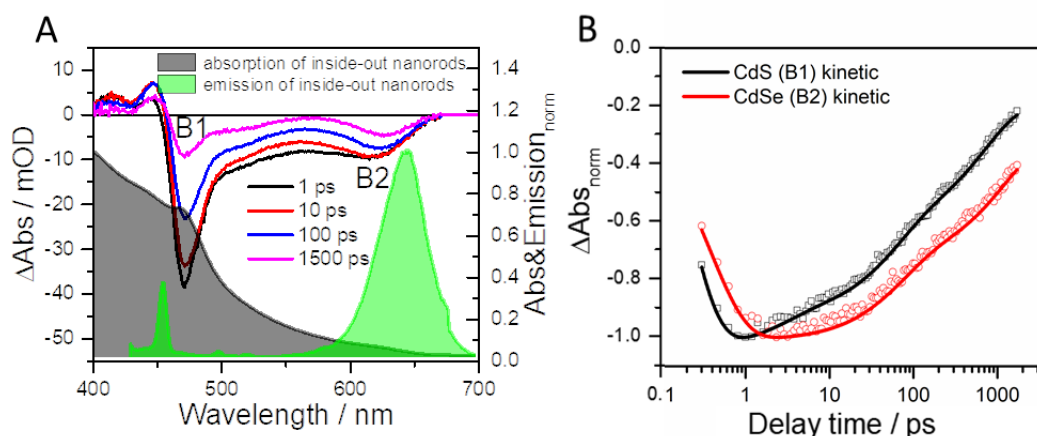


Figure 3.11. (A) The TA spectral of the inside-out NRs in toluene excited at 390 nm probed with white light together with the absorption and emission spectra (excited at 400 nm) of the inside-out NRs and (B) the kinetics of CdS and CdSe bands normalized to -1 at the kinetical minimum, 470 nm and 620 nm, respectively.

With above mentioned data interpretation of the dot-in-rod NRs, the details of electron motion in the inside-out NRs could be compared. The optical density of the sample for this measurement was 0.26 at 400 nm. The transient absorption spectra at different delay times were showed in Figure 3.11A. Upon 390 nm excitation, a strong instantaneous bleach (B1) for the levels associated with the CdS part was observed centered at around 470 nm (2.64 eV), followed by a much slower build-up of a bleach (B2) centered at around 620 nm (2.00 eV) due to carrier relaxation into the CdSe part. These features were also in agreement with the shift in steady-state absorption measurements. As also mentioned in the discussion of steady-state results, the inside-out NRs had both large size distribution of CdS and CdSe resulted in much wider ground state bleach of B1 and B2 compared to the ground state bleach in the dot-in-rod NRs. The B2 minimum clearly red shifted from 1 ps to 1500 ps which could be due to the non-radiative energy loss caused by trap state, unlike the dot-in-rod NRs where the CdSe core was passivated with CdS shell strongly reduced the trap state.

The kinetics at different band were extracted by a single kinetic at the signal minimum of each bleach and a global fit of 10 nm scale centered at the bleach signal minimum, the single kinetic was displayed in Figure 3.11B, both kinetics followed the same basic shape, which was a fast signal formation and an incomplete signal decay ended up with -0.2 and -0.4 in ΔAbs_{norm} for B1 and B2, respectively. And the data discussed next were obtained by global fit. The B1 kinetic could be nicely described by four exponential decay model, one time component in signal formation and three time components in signal decay. The τ_f in formation signal around 0.2 ps referred to the cooling of “hot electron” to the band edge. This agreed with the cooling process in the dot-in-rod NRs. The second component τ_1 was in signal decay and was ~ 1.0 ps in global fit which could be assigned to the depopulation of electron on the conduction band of CdS. This could be assigned to the electron movement to the lower conduction band of CdSe or shallow electron trap state. In this inside-out NRs, the electron movement first to the lower conduction band of CdSe then to the electron trap state was an appropriate explanation. This assignment was done based on the following reasons. Firstly, shallow states could be caused by several reasons, the impurities, surface defects and so on.¹⁸⁹ The surface coverage of nanostructures by TOPO ligands (the same ligand used in this chapter) was only 30-50% as introduced in chapter 1. There was still high chance for surface site to be exposed without passivation. Secondly, for core/shell structures, the shell would have much more pronounced surface states than the core. Third, both processes had the time constant falling in a similar time range in ps scale.¹⁹⁰ The competing between electron localization on the conduction band of the CdSe and the electron trap state showed different results in both structures. In the dot-in-rod NRs, the electron localization on the conduction band of the CdSe dominated due to stronger influence of the hole localization at the CdSe while in the inside-out NRs, the electron trap state was in domination because of the lack of hole localization in the inside-out NRs which would be discussed in the next content. Fourth, the interpretation of the multi-Gaussian peaks fit in emission spectra also confirmed the presence of this surface state. To finish the data interpretation of the CdS part, the third and fourth components (referring to τ_2 and τ_3) were in signal decay and ~ 49 ps and ~ 659 ps in global fit, referring to the recombination processes.

For the CdSe part, the kinetic could only be nicely described with three time components but not with four. Due to the large size distribution of CdSe in the inside-out structure, the global fit of 10 nm scale centered at 620 nm would describe the exciton behaviors more appropriately by reflecting average time components contributed by different sizes of CdSe parts. By the global fit of the CdSe band, the first time component in signal formation was ~ 0.4 ps referring to the cooling process to the band edge of CdSe. There was no second time component (referring to τ_1) at picosecond scale, which could be assigned with the above-mentioned electron trap states. This could be explained by more surface defects at the CdSe shell resulting in “deep” traps which

would decrease the recombination rate then resulting in a longer time component. This time component would merge into the longer recombination processes. Due to the deep trap of the hole in consist with the steady-state emission discussion, the hole localization process at the CdSe VB due to Coulombic force interaction was not pronounced in the inside-out structure. Compared to argument of no hole localization process in this inside-out NRs, another explanation would be more accurate. Although there was no evidence of hole localization related electron movement from the CB of the CdS to the CB of the CdSe, the hole localization could still happen at the CdSe. However, the deep hole trap on the CdSe shell was so pronounced that the Coulombic interaction between the hole and electron was negligible, so there was no pronounced electron population on the CB of CdSe shell resulting in no second signal formation time component τ_{f2} in the kinetic compared to the dot-in-rod NRs. The third and fourth time components (referring to τ_2 and τ_3) were ~ 68 ps and ~ 1194 ps assigning with recombination processes. All these arguments were summarized in the illustration of the carrier dynamics in the inside-out NRs in Figure 3.12.

CdS (B1) and CdSe (B2) kinetics showed four and three time components, respectively. However, unlike the dot-in-rod NRs where the first decay time component in CdS and the second formation time component in CdSe agree with each other in the same picosecond time scale with opposite amplitudes referring to the hole localization process, both kinetics in inside-out NRs showed no evidence of hole localization process in this structure but hole localization at CdSe could still exist. The related time components were listed in Table 3.2 and detailed global fit results together with DAS were displayed in Figure 3.13.

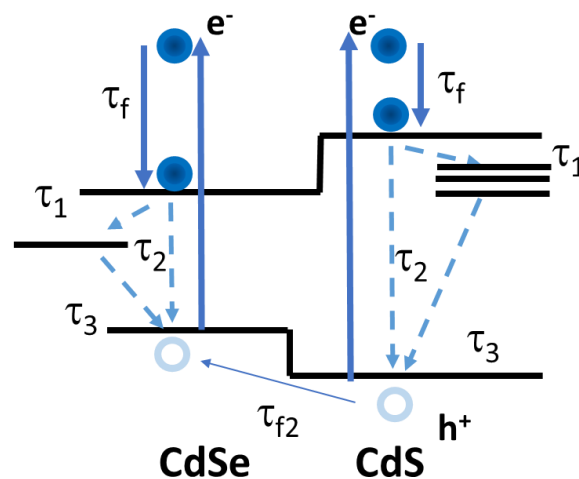


Figure 3.12. The illustration of the carrier dynamics in the inside-out NRs upon excitation. The CdSe and CdS parts of the inside-out NRs were both excited upon 390 nm excitation. The formation signal time component (τ_f) and decay time components (τ_2 and τ_3) were clearly assigned with colling of hot electron

to the band edge and the recombination processes. The decay time component (τ_1) in the CdS core was fitted in the time range of picosecond scale referring to the competing process between shallow surface states and electron migration to the CB of the CdSe shell. The time component (τ_1) in the CdSe shell was missing due to more pronounced surface defects resulting in deep surface states which further resulting in competing process on the CB of the CdSe shell between electron depopulation due to deep surface states and electron population due to electron migration from the CB of the CdS core to the CB of the CdSe shell. So, it was hard to identify the hole localization process (τ_2) from TA results in the inside-out NRs.

Table 3.2. Fitting parameters for the TA kinetics of the inside-out NRs (global fit of 10 nm scale centered at each bleach signal minimum and single kinetic fit displayed in Figure 3.11B). *The offset and amplitudes with associated errors of global fit were displayed in DAS in Figure 3.13.

	Global fit*		Single kinetic fit	
	CdS	CdSe	CdS	CdSe
Adj. R-Square	0.997	0.992	0.998	0.994
y_0	–	–	-0.19 ± 0.01	-0.32 ± 0.04
τ_f (ps)	0.2 ± 0.1	0.4 ± 0.1	0.2 ± 0.1	0.4 ± 0.1
A_f	–	–	1.58 ± 0.32	0.80 ± 0.06
τ_1 (ps)	1.0 ± 0.1	–	2.7 ± 0.5	–
A_1	–	–	-0.12 ± 0.01	–
τ_2 (ps)	49 ± 1	53 ± 1.4	57 ± 4	68 ± 5
A_2	–	–	-0.30 ± 0.01	-0.27 ± 0.01
τ_3 (ps)	659 ± 15	813 ± 34	712 ± 57	1194 ± 250
A_3	–	–	-0.42 ± 0.01	-0.40 ± 0.03

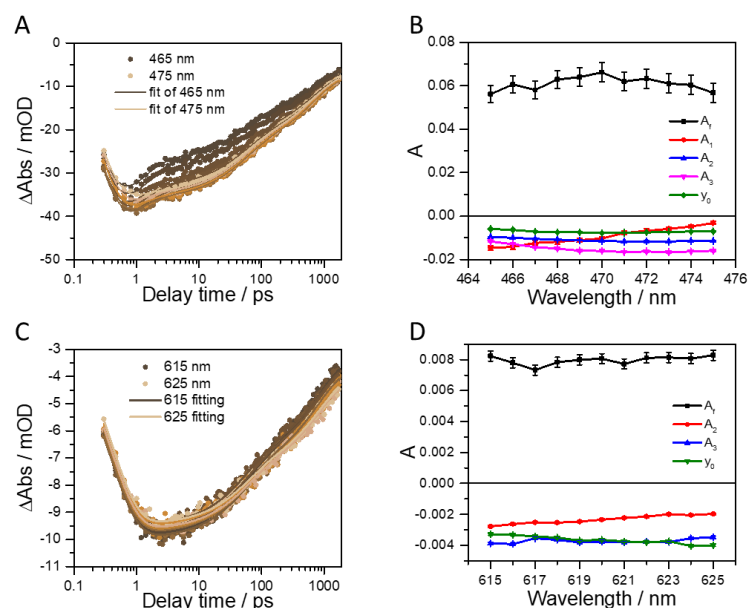


Figure 3.13. The global fit of the first measurement on the inside-out NRs (A) 10 nm scale centered at CdS bleach signal minimum 470 nm and (C) 10 nm scale centered at CdSe bleach signal minimum 620 nm. The DAS of global fit of (B) CdS and (D) CdSe parts, respectively.

3.3.3 Further measurements on the inside-out NRs and discussion

Differences of the sample signal in the repeat measurement of TA caught our attentions. Repeat measurements were performed on the inside-out NRs for additional two times, the second time was two months after the first measurement and the third time was four months after the first measurement. The TA spectra of these inside-out NRs measurements were shown in Figure 3.14, respectively. The shape of the spectra was almost identical for each time measurement on the first glance. However, from the first time to the third time measurement, the signal intensity at 470 nm referring to CdS part was decreasing from -40 to $-7 \Delta\text{mOD}$, despite for each measurement the laser intensity and beam diameter were comparable and the optical density of samples were actually increasing, 0.26, 0.36 and 0.38, respectively, indicating the sample was degrading during this four months storage time although the normalized absorption spectra of the showed no differences in Figure 3.15A. Also, the bleaches of both the CdS and CdSe were narrower in the second measurement and the narrowest in the third measurement, which could be explained by smaller size distribution due to degrading. Notably, the ratio of the intensity at CdS and CdSe bleach signal minimum also changed for each measurement. The ratio of the intensity at CdS and CdSe bleaches was ~ 3.5 at 10 ps and ~ 2.0 at 1500 ps for the first measurement. The ratio of the bleaches was reduced to ~ 2.3 at 10 ps and ~ 1.4 at 1500 ps for the second measurement. The ratio then was further reduced to ~ 1.5 at 10 ps and ~ 1.0 at 1500 ps.

So, the ratio decreased both at early time (10 ps) and late time (1500 ps) further indicating that the material itself was changing during the storage time.

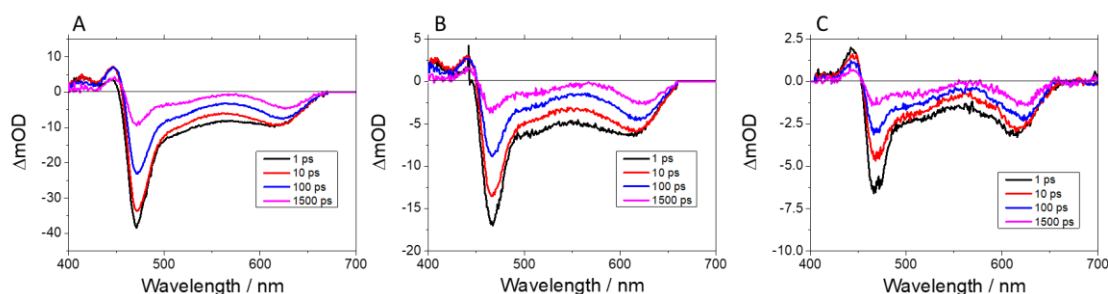


Figure 3.14. The TA spectral of the inside-out NRs of each TA measurement, (A) the first time, (B) the second time and (C) the third time, excitation wavelength was 390 nm with white light probed, the solvent was toluene.

To clarify the influence of laser during the measurements on the sample signal, the single scans of the second time measurement were also plotted in Figure 3.15B. No evidence of degrading during different scans was found. The slight decrease in signal intensity was more likely due to the instability of the laser. If there was no degrading during the measurement, the signal drop between each measurement was more likely due to degrading while the sample was in storage which is a known drawback of most reported inverted structures where both domains were exposed to the surrounding medium then introduced instability of these inverted structures.

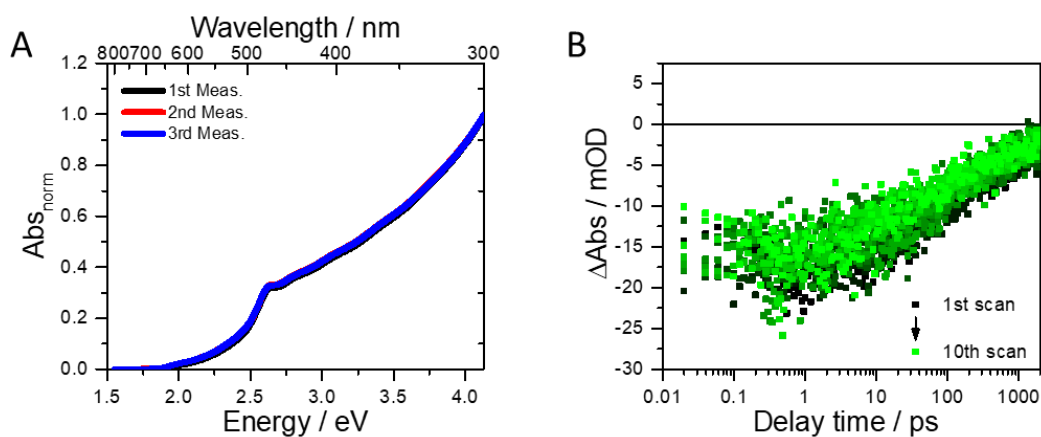


Figure 3.15. (A) The absorption spectra of the samples for transient absorption measurements in toluene, normalized as 1 at 4.13 eV (300 nm). (B) The kinetics of the inside-out NRs at 470 nm from the single scans of the second measurement, excitation wavelength was 390 nm and solvent was toluene.

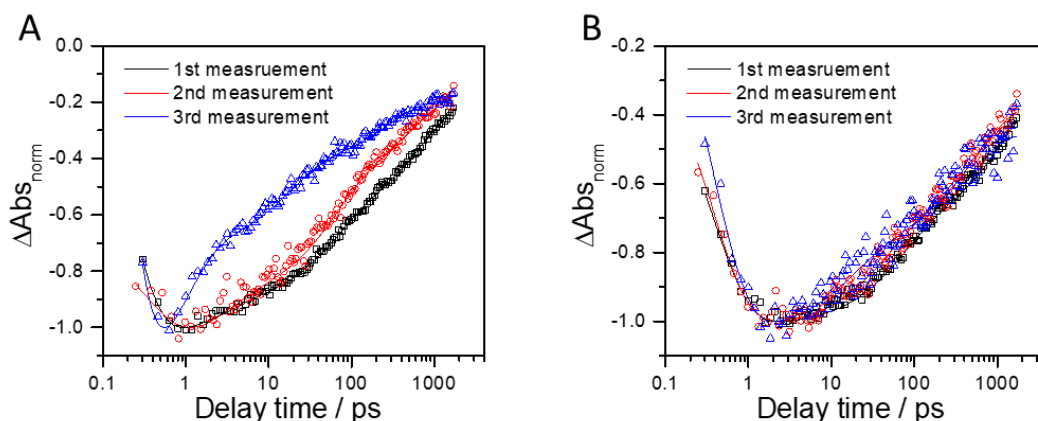


Figure 3.16. The single kinetics of all three times measurements, (A) single kinetics at 470 nm for CdS and (B) single kinetics at 620 nm for CdSe part. The excitation wavelength was 390 nm and solvent was toluene.

Not only the spectral shape in the TA changed, but also the dynamics altered during the different measurements. All the single kinetics referring to CdS part of different measurements were plotted in Figure 3.16A only for illustration. The time components were fitted by a four-exponential global fit of both CdS part (in 10 nm range centered at 470 nm) and CdSe part (10 nm range centered at 620 nm) to give reasonable comparison. Detailed parameters from global fit were displayed in Table 3.3 and Figure A1 and A2 in the Appendix. For CdS part, the kinetics of the 1st and 2nd time measurements were nearly identical, the time components of signal formation were all in 0.2 – 0.3 ps range but only a slightly accelerated decay signal in the second measurement. However, the kinetic of the third measurement decayed much faster. The first decay components (τ_1) were all calculated in the range of 1 – 5 ps range but for the third time the amplitude was much larger than the first and second measurements. This could be an indication that the surface states of CdS part was much more pronounced for the third time probably due to degrading of CdSe shell at the third time. The second and third decay time components (τ_2 and τ_3) were calculated as ~ 50 ps, and ~ 660 ps for the first measurement and ~ 65 ps and ~ 640 ps for the second measurement. These time components were quite comparable indicating the degrading of CdS was absent. They were reduced to ~ 15 ps and ~ 250 ps in the third measurements indicating the beginning of CdS degrading.

Unlike the single kinetics of the CdS part, no obvious changes could be seen from the kinetics of the CdSe part in the logarithm scale. And, since global fitting would not give information on absolute amplitudes, the single kinetics were discussed first. The kinetics of the bleach signal minimum of the CdSe part in all the TA measurements were plotted and showed in Figure 3.16B. The related fitting parameters were displayed in Table 3.4. The signal kinetics were normalized to -1 at the signal minimum. The offset (y_0) were all around 0.3 – 0.4 indicating further

recombination processes beyond the introduced delay stage. The time components corresponded to signal formation (τ_f) were all around 0.4 ps referring to the cooling of the electron to the band edge. Same as discussed above, there was no τ_1 here. The decay time components τ_2 decreased from $68(\pm 5)$ ps to $17(\pm 4)$ ps from the first measurement to the third measurement with nearly identical absolute amplitudes from $-0.27(\pm 0.01)$ to $-0.22(\pm 0.02)$, while the decay time components τ_3 decreased from $1194(\pm 250)$ ps to $305(\pm 44)$ ps with nearly unchanged absolute amplitudes from $-0.41(\pm 0.03)$ to $-0.35(\pm 0.02)$. This was the case that only time components become faster, but the associated amplitudes stayed the same. So, no obvious changes could be seen from the kinetics of the CdSe part in the logarithm scale. These decreasing time components with nearly identical amplitude strongly indicated that the same recombination processes were of faster recombination rate. Combining the increasing offset at the end of the kinetics (y_0), this could be explained by more pronounced electron trap state generation from the degradation. With the results from single kinetics fit, more reliable time components could be obtained from the global fit results. The signal formation time components of all measurements were all ~ 0.4 ps referring to cooling. The two decay time components were calculated as ~ 53 ps and ~ 813 ps for the first measurement and ~ 32 ps and ~ 461 ps for the second measurement, indicating sample degrading. They were further reduced to ~ 14 ps and ~ 273 ps in the third measurements. These results indicated the degrading of CdSe part started before the degrading of CdS part. The kinetic change in CdS kinetics was probably due to slower degrading of the CdS part in the first two months of storage but a much faster degrading in the following two months of storage. And the kinetic change in CdSe kinetics indicated that the CdSe part was already degrading during the first two months in storage and then further degraded in the next two months storage time.

Table 3.3. The detailed fit parameters of the global fit for kinetic traces of different measurements on the inside-out NRs at different times. The global fit and DAS of the first measurement was displayed in Figure 3.13. The global fit and DAS of the second and third time measurements were displayed in Figure A1 and A2.

	CdS			CdSe		
	1 st Meas.	2 nd Meas.	3 rd Meas.	1 st Meas.	2 nd Meas.	3 rd Meas.
Adj. R-Square	0.998	0.991	0.992	0.984	0.984	0.945
τ_f (ps)	0.2 ± 0.1	0.3 ± 0.1	0.2 ± 0.1	0.4 ± 0.1	0.3 ± 0.1	0.4 ± 0.2
τ_1 (ps)	1.0 ± 0.1	4.2 ± 0.4	0.9 ± 0.1	–	–	–
τ_2 (ps)	49 ± 1	66 ± 3	15 ± 1	53 ± 1	32 ± 1	14 ± 1
τ_3 (ps)	659 ± 15	637 ± 49	253 ± 6	813 ± 34	461 ± 15	273 ± 12

Table 3.4. The detailed fit parameters of the single kinetics fit of the CdSe part at the bleach signal minimum on the inside-out NRs at different times.

	1 st Meas.	2 nd Meas.	3 rd Meas.
Adj. R-Square	0.993	0.980	0.950
y_0	-0.32 ± 0.04	-0.37 ± 0.02	-0.46 ± 0.01
τ_f (ps)	0.4 ± 0.1	0.4 ± 0.1	0.4 ± 0.1
A_f	0.82 ± 0.06	0.91 ± 0.09	1.27 ± 0.19
τ_1 (ps)	–	–	–
A_1	–	–	–
τ_2 (ps)	68 ± 5	39 ± 5	17 ± 4
A_2	-0.27 ± 0.01	-0.25 ± 0.02	-0.22 ± 0.02
τ_3 (ps)	1194 ± 250	579 ± 91	305 ± 44
A_3	-0.41 ± 0.03	-0.39 ± 0.02	-0.35 ± 0.02

All these evidences led us to a hypothesis that the CdSe shell already degraded between the 1st measurement and the 2nd measurement because of the difference between kinetics at CdSe part between the first time and the second time measurements. Also, the CdS rods beneath the CdSe shell degraded between the 2nd measurement and the 3rd measurement because the dramatic difference between kinetics at CdS part from the second time and the third time measurements. These results illustrate that although steady-state absorption showed no severe changes in the electronic structure, charge dynamics could already be sensitively impacted by aging of the sample. To reveal the atomistic source of this effect, a systematic investigation of the morphology of sample degrading is needed.

3.3 Conclusion

In this chapter, using the dot-in-rod NRs as a reference, the ground state electronic structure and excited charge carrier dynamics of the inside-out NRs were investigated. The steady-state absorption spectroscopy was introduced to investigate the size distribution of the CdSe part in the dot-in-rod and inside-out NRs. The size distribution of CdSe part in the inside-out NRs was larger than that in the dot-in-rod NRs. This was further confirmed by the steady-state emission spectroscopy and TA spectroscopy. The steady-state emission spectroscopy revealed the surface states of both the dot-in-rod and inside-out NRs indicating more and/or deep surface states on the CdSe shell of the inside-out NRs. Then surface states together with charge recombination processes were probed by transient absorption spectroscopy.

The hole localization driven electron localization feature was not observable on the kinetics at both CdS and CdSe part, and this could be related with the surface state of the inside-out NRs. The surface state could turn from “shallow” to “deep” state if the surface defects reached a certain threshold, although this threshold was still unknown and more related work need to be done. The degradation of the inside-out NRs was observed and in consist with reported similar structures. The degradation should be followed systemically with PL spectroscopy. In this way, the surface states changes might be revealed. On the other hand, the band alignment of this inside-out NRs was not very clear and should be probed with further investigation. This could be done by investigating the kinetic of CdS part using transient absorption measurements where only the CdSe part is pumped. This novel inside-out NRs still faced drawbacks of its instability according to the results from multiple measurements in transient absorption spectroscopy. The next step would be to optimize the size, aspect ratio or even the composition of this nanostructure to stabilize its long-term behaviors.

cysteine¹⁹³ These ligands are attached to the NRs surface by their thiol group(s). The negatively charged carboxylate group stabilizes the dispersed NRs in water at neutral and basic pH values. However, MAA-NRs would face problems of bad colloidal stability at low pH, due to the protonation of the carboxylate group.^{78, 191} Thus, MAA-NRs are only suitable for photocatalytic systems working at $\text{pH} > 6$ as has been shown for the NRs tipped with platinum or nickel particles.^{76, 77, 194-196} However, in some photocatalytic systems, catalysts require acidic conditions for the best performance for the photocatalytic HER, such as [FeFe]-H₂ase mimics¹⁹⁷⁻¹⁹⁹ or certain metal dichalcogenide nanoparticles²⁰⁰. For applications in acidic conditions, the hydrophilic segment need to be replaced from a carboxyl group to a moiety that mediates the NRs with good colloidal stability at acidic pH or over a wide pH range. A promising candidate towards this direction is a poly(ethylene glycol) (PEG) chain which has already been shown to greatly improve the water dispersibility of CdSe quantum dots (QDs) irrespective of pH values.^{192, 201-203} A slightly different approach was to coat the NRs with hydrophilic polymers such as poly(ethylene imine) (PEI), where the imines both act as the anchor group as well as the hydrophilic segment. PEI-coating has already been reported to stabilize the quantum dots^{80, 204-208} and NRs^{76, 209} at $\text{pH} \leq 7$.

Surface coating does not only allow the NRs with stability in suspensions of different pH values, but also impacts the electronic properties and basic exciton dynamics in NRs: The intrinsic surface defects such as unpassivated metal ions, which may act as trap sites for electrons, can be passivated by electron-donating ligands such as TOPO.²¹⁰ The thiolate anchor groups can act similarly as electron trap passivation, but they also introduce trapping sites for holes. Experimentally, this could be observed as a decrease in the emission intensity in the case for the NRs, as hole localization to surface trap sites efficiently competes with the hole localization to the CdSe core⁹². Theoretically, this effect could also impact the activity of catalytically active systems, where trapping of charge carriers compete with charge separation with subsequent electron transfer to a catalyst and hole localization to the CdSe core. For example, gold-decorated PEI-NRs exhibits one (for CdS NRs) to two (for CdSe/CdS NRs) orders of magnitude higher photon to hydrogen conversion efficiency than MAA-NRs.⁷⁶

In this chapter, a study on the influence of different ligands (Figure 4.1) on the optical properties and exciton dynamics of CdSe/CdS NRs was reported. The ligands reported can be classified by their anchor groups, namely mono-thiols (MUA, HS-PEG-OCH₃), di-thiols (DHLA, DHLA-PEG), and imines (PEI), as well as their hydrophilic segment, namely carboxylate (MUA, DHLA), a PEG chain (HS-PEG-OCH₃, DHLA-PEG), and imines (PEI). The ligand exchange protocols were already introduced in chapter 2. But to give a short message here, the ligand exchange of MUA, HS-PEG-OCH₃, and DHLA were carried out in MeOH solution with approximate pH 11. The ligand exchange of DHLA-PEG were performed in neutral MeOH solution at 50 °C for at least 4 hours due to the possible hydrolysis of the -COOR group in basic condition. And PEI was coated on the NRs in CHCl₃ followed by precipitation with cyclohexane. Results obtained with these surface ligands were compared to the benchmark system TOPO-NRs in toluene. The NRs with different surface ligands were investigated by steady-state and

time-resolved absorption and photoluminescence spectroscopy to obtain information on the electronic properties and exciton dynamics in these NRs together with their pH stabilities. All data in this chapter were based on the analysis of two batches of NRs obtained from two individual synthesis, namely NRs #1 and NRs #2, but the displayed figures were always based on the NRs #2 if not otherwise indicated.

4.1 Characterization of NRs

4.1.1 The determination of size distribution of TOPO-NRs

The NRs we investigated in this chapter were two batches of NRs obtained from two individual synthesis with the same synthesis protocol, as mentioned above namely NR #1 and NR #2. The dimension and size distribution information of NRs was obtained from both batches. The dimension of NRs was characterized using ImageJ version 1.52a on the TEM images of the TOPO-NRs. In Figure 4.2, two batches of TOPO-NRs were determined with a length of 30.2 ± 2.3 nm and 29.3 ± 2.7 nm, respectively, and a diameter of 4.6 ± 0.5 nm and 4.3 ± 0.5 nm, respectively.

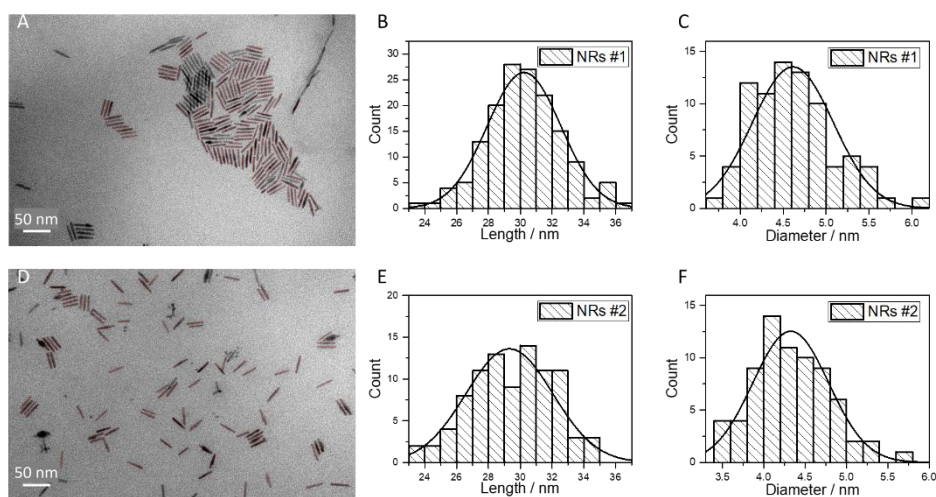


Figure 4.2. The TEM images of two batches of NRs (A) NRs #1 and (D) NRs #2, the length distribution of (B) NRs #1 and (E) NRs #2 and the diameter distribution of (C) NRs #1 and (F) NRs #2. The red line in (A) and (D) indicate the NRs which were chosen as the measuring target of the length of NRs.

4.1.2 Infrared spectroscopy investigation on NRs and discussion

The ligand exchange was monitored by FTIR spectroscopy using ATR mode. For each ligand exchanged NRs, the IR spectra of the relative pure ligand was also recorded as the reference. Detailed information on IR spectra of the pure ligands and ligand capped NRs were listed in Table 4.1 – 4.6 and related IR spectra were displayed in Figure 4.3 – 4.8. There were some characteristic peak feature worth mentioning indicating the replacement of the surface ligands.

For example, in Table 4.1 and Figure 4.3, the P=O stretch red shifted from 1143 cm^{-1} in pure TOPO to 1092 cm^{-1} in TOPO-NRs indicating the attachment of TOPO ligand on NRs.²¹¹ In Table 4.2 and Figure 4.4, the disappearance of -SH stretch in the MUA-NRs compared to the peak at 2553 cm^{-1} in pure MUA and the missing P=O stretch at 1190 cm^{-1} compared to the TOPO-NRs indicated the successful ligand replacement from TOPO-NRs to MUA-NRs. The same feature could also be seen from Table 4.3 - 4.5, that the ligand exchange of HS-PEG-OCH₃, DHLA and DHLA-PEG were also proven to be successful with the disappeared P=O stretch and -HS stretch. In Table 4.6, the disappearance of P=O stretch at 1092 cm^{-1} and the appearance of asymmetric and symmetric stretch of -NH₂ at $3350 - 3272\text{ cm}^{-1}$ indicated the successful ligand exchange of PEI although the general shape of the PEI and PEI-NRs stayed basically the same due to the tiny amount of bonding site in the PEI-NRs. The successful ligand exchange could be confirmed by the comparison among FTIR spectrum of NRs with different ligands. All IR spectra displayed in Figure 4.3 – 4.8 were normalized to [0, 1] for better illustration and the comparison in this section was only qualitatively.

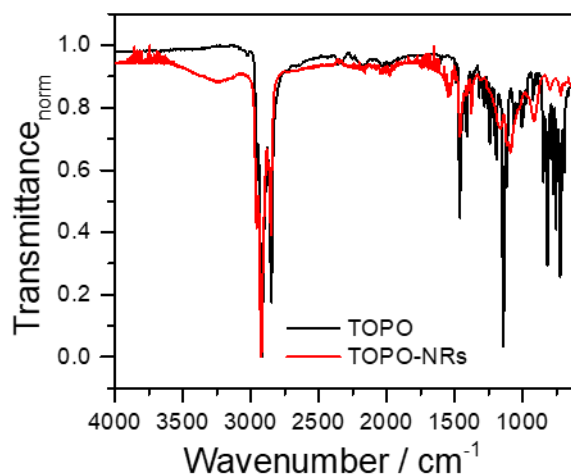


Figure 4.3. The IR spectra of TOPO and TOPO-NRs normalized as 0 to 1.

Table 4.1. IR-frequencies of TOPO and TOPO-NRs. All bands have been assigned according to reference²¹² if not noted otherwise.

wavenumber / cm ⁻¹		assigned vibration
TOPO	TOPO-NRs	
2950	2956	-CH ₃ asymmetric stretching vibrations
2924	2917	-CH ₂ asymmetric stretching vibrations
2869	2870	-CH ₃ symmetric stretching vibrations
2848	2852	-CH ₂ symmetric stretching vibrations
1471	1466	-CH ₂ scissor
1464	1464	-CH ₃ asymmetric bend
1456	1455	P-CH ₂ asymmetric deformation
1377	1379	-CH ₃ symmetric bend
1258	1258	P-CH ₂ symmetric deformation
1260	1260	-CH ₂ rock
1143	1092	P=O stretch ²¹¹
1118	1119	-CH ₂ wag
751	720	-(CH ₂) _n - (n > 4) in phase rock
694	692	P-C stretch

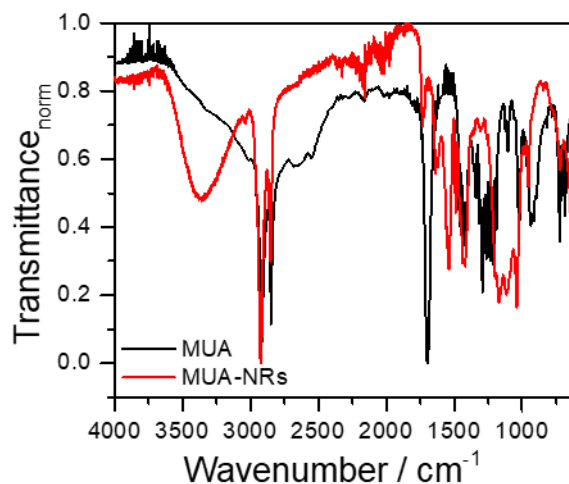


Figure 4.4. The IR spectra of MUA and MUA-NRs normalized as 0 to 1.

Table 4.2. IR-frequencies on MUA and MUA-NRs. All bands have been assigned according to reference²¹². (–) indicates the absence of a vibration.

wavenumber / cm ⁻¹		assigned vibration
MUA	MUA-NRs	
2916-2848	2924-2853	–CH ₂ asymmetric and symmetric stretching vibrations
2551	–	–SH stretching
1679	1635	–COOH, C=O asymmetric stretch
1454	1457	–CH ₂ scissor
1410	1419	C–O–H in-plane bend
1341-1210	1335-1198	C–O stretch
1262	1263	–CH ₂ wag
1122	1103	C–C skeletal stretch
1107	1114	–CH ₂ rock
1097	1102	C–O–C asymmetric stretch
936	953	OH ... O out-of-plane wag
886	889	C–O–C symmetric stretch
725	720 and 730	–(CH ₂) _n – (n > 4) in phase rock
665	673	C–S stretch

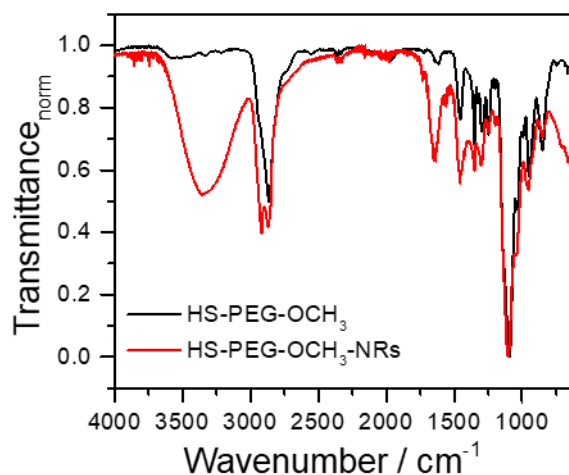


Figure 4.5. The IR spectra of HS-PEG-OCH₃ and HS-PEG-OCH₃-NRs normalized as 0 to 1.

Table 4.3. IR-frequencies on HS-PEG-OCH₃ and HS-PEG-OCH₃-NRs. All bands have been assigned according to reference²¹². (–) indicates the absence of a vibration.

wavenumber / cm ⁻¹		assigned vibration
HS-PEG-OCH ₃	HS-PEG-OCH ₃ -NRs	
2940-2863	2918-2871	–CH ₂ asymmetric and symmetric stretching vibrations
2551	–	–SH stretching
1453	1456	–CH ₂ scissor
1440	1436	O–CH ₃ symmetrical deformation
1470	1473	O–CH ₃ asymmetrical deformation
1400	1419	C–O–H in-plane bend
1350-1200	1349-1200	C–O stretch
1248	1249	–CH ₂ wag
1038	1043	–CH ₂ rock
1094	1104	C–O–C asymmetric stretch
848	850	C–O–C symmetric stretch
742	720	–(CH ₂) _n – (n > 4) in phase rock
742	720	C–S stretch

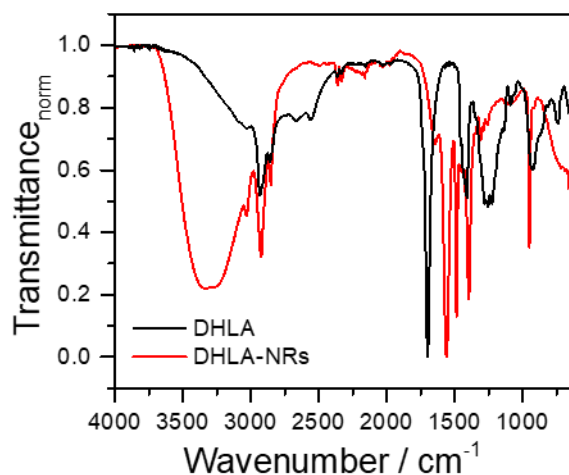


Figure 4.6. The IR spectra of DHLA and DHLA-NRs normalized as 0 to 1.

Table 4.4. IR-frequencies of DHLA and DHLA-NRs. All bands have been assigned according to reference²¹² if not noted otherwise. (–) indicates the absence of a vibration.

wavenumber / cm ⁻¹		assigned vibration
DHLA	DHLA-NRs	
2931-2858	2922-2852	–CH ₂ asymmetric and symmetric stretching vibrations
2557	–	–SH stretching
1700	1650	–COOR, C = O asymmetric stretch
1455	1455	–CH ₂ scissor
1228	1258	–COOR, C–O stretch
1253	1289	–CH ₂ rock
1140	1123	–CH ₂ wag
742	–	–(CH ₂) _n – (n > 4) in phase rock
660	657	C–S stretch

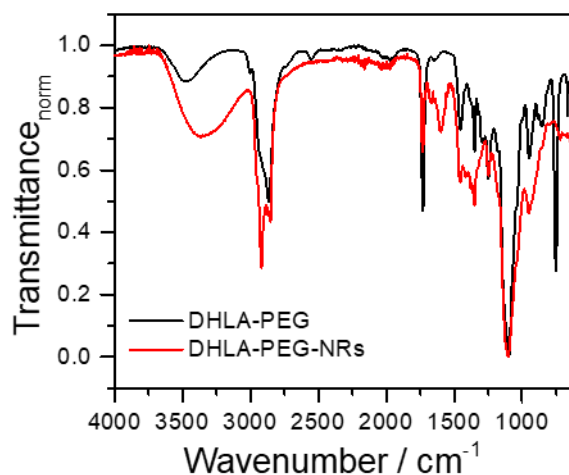


Figure 4.7. The IR spectra of DHLA-PEG and DHLA-PEG-NRs normalized as 0 to 1.

Table 4.5. IR-frequencies of DHLA-PEG and DHLA-PEG-NRs. All bands have been assigned according to reference ²¹² if not noted otherwise. (–) indicates the absence of a vibration.

wavenumber / cm ⁻¹		assigned vibration
DHLA-PEG	DHLA-PEG-NRs	
2933-2849	2953-2852	–CH ₂ asymmetric and symmetric stretching vibrations
2553	–	–SH stretching
1732	1732	–COOR, C = O asymmetric stretch
1455	1455	–CH ₂ scissor
1248	1248	–COOR C–O stretch
1260	1260	–CH ₂ rock
1176	1170	–CH ₂ wag
1097	1102	C–O–C asymmetric stretch
886	889	C–O–C symmetric stretch
725	720	–(CH ₂) _n – (n > 4) in phase rock
665	673	C–S stretch

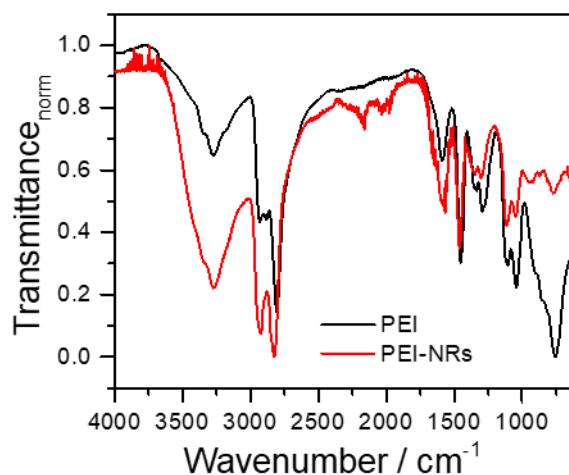


Figure 4.8. The IR spectra of PEI and PEI-NRs normalized as 0 to 1.

Table 4.6. IR-frequencies on PEI and PEI-NRs. All bands have been assigned according to reference²¹².

wavenumber / cm ⁻¹		assigned vibration
PEI	PEI-NRs	
3352-3272	3350-3272	-NH ₂ asymmetric and symmetric stretching vibrations
2931-2807	2920-2826	-CH ₂ asymmetric and symmetric stretching vibrations
1586	1566	-NH ₂ scissor amide II C-N-H bend
1454	1461	-CH ₂ scissor
1300	1293	amide III C-N-H bend
1332	1345	-CH ₂ wag
1274	1271	C-N-C ₂ stretch
1043	1049	C-NH ₂ wag
1104	1115	N-C ₃ stretching
855	871	C-NH ₂ rock C-N-C symmetric stretching
758	770	-CH ₂ rock

4.2 Steady-state measurements on the NRs and discussion

First insight on the impact of the ligands on the optical and electronic properties of the NRs was investigated by steady-state UV/Vis absorption and emission spectroscopy. In Figure 4.9, spectra of NRs #2 from the same batch but with various surface ligands were shown. The absorption spectra showed the characteristic features for NRs with the lowest energy excitonic transition of the CdS shell at around 2.67 eV and of the CdSe core at around 2.22 eV. Subtle differences between the exact positions of the excitonic peaks between the NRs with varying surface ligands were listed in Table 4.7. Notably, both CdS and CdSe absorption were blue shifted for PEI-NRs compared to TOPO-NRs, while the other ligands did not shift the absorption dramatically.

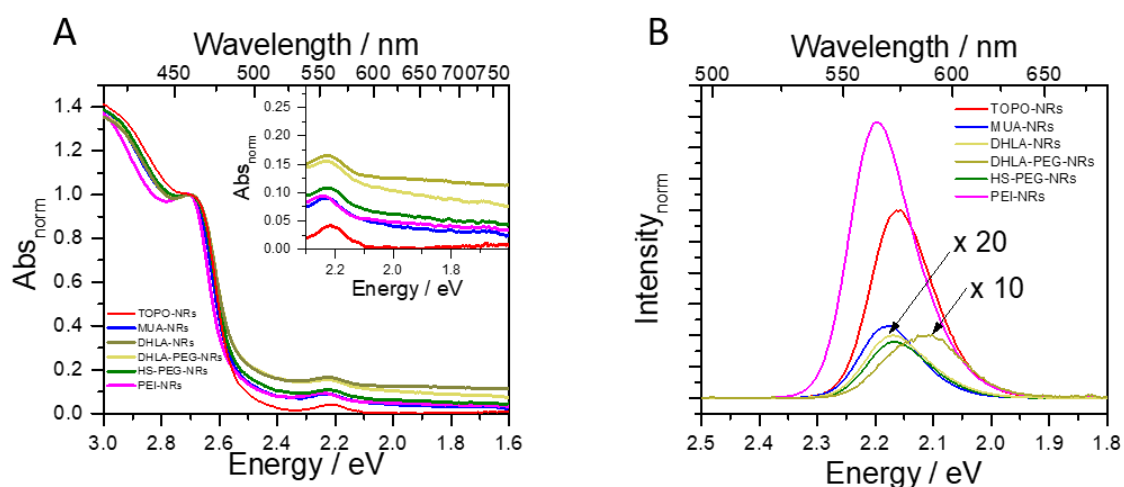


Figure 4.9. Steady-state spectroscopy on NRs #2 capped with different ligands. TOPO-NRs were dispersed in toluene, while MUA-, HS-PEG-OCH₃-, DHLA-, DHLA-PEG-, and PEI-NRs were dispersed in water. (A) Absorption spectra normalized to the lowest energy excitonic CdS absorption peak. The inset depicts the region of CdSe core absorption. (B) Emission spectra ($\lambda_{ex} = 450$ nm, for PLQY measurements) whose integrals have been normalized to their respective emission quantum yield. The emission spectrum of DHLA-PEG-NRs and DHLA-NRs have been enlarged by a factor of 20 and 10, respectively, for better comparison.

Table 4.7. Steady-state absorption and emission spectroscopy on NRs #2 with different surface ligands. Data for TOPO-NRs was recorded in toluene, while the other NRs were measured in pure water. Listed were the spectral position of the lowest energy excitonic CdS absorption peak $E_{abs,CdS}$, the CdSe seed absorption peak position $E_{abs,CdSe}$, the spectral position of the peak emission E_{em} , the absolute emission quantum yield Φ_{em} and the Stokes shift ($E_{abs,CdSe} - E_{em}$). Emission was recorded upon excitation at 400 nm and the absolute emission quantum yield was recorded upon excitation at 450 nm.

Ligand	$E_{abs,CdS}$ / eV	$E_{abs,CdSe}$ / eV	E_{em} / eV	Φ_{em}	$(E_{abs,CdSe} - E_{em})$ / meV
TOPO	2.67	2.22	2.16	0.60 ± 0.02	60
MUA	2.68	2.24	2.18	0.23 ± 0.05	60
DHLA	2.67	2.24	2.17	0.02 ± 0.02	70

DHLA-PEG	2.67	2.24	2.13	0.01 ± 0.02	110
HS-PEG-OCH ₃	2.67	2.24	2.17	0.18 ± 0.07	70
PEI	2.70	2.25	2.19	0.88 ± 0.12	60

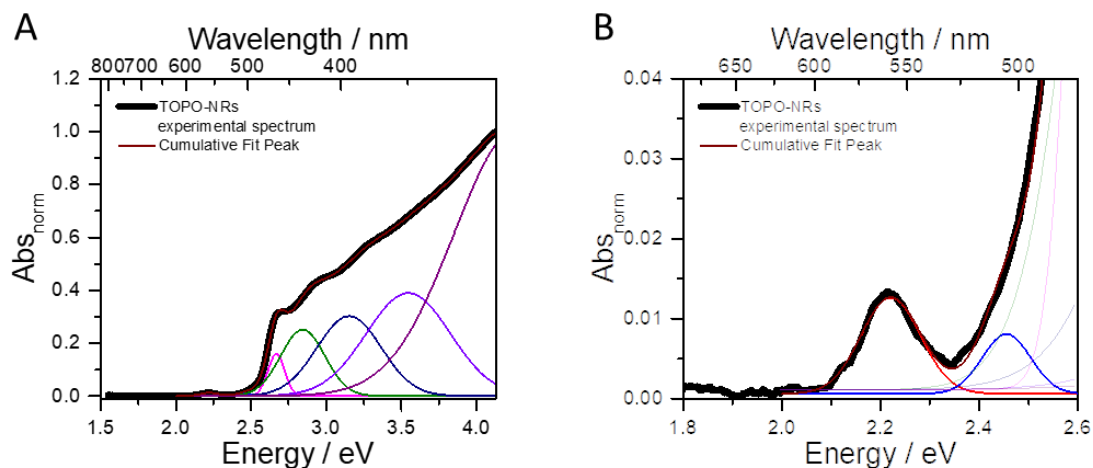


Figure 4.10. Multi-Gaussian peaks fit of the absorption spectrum of TOPO-NRs. (A) Full wavelength range and (B) CdSe related wavelength range absorption spectra recorded in toluene fitted using seven Gaussians. All spectra were normalized to 1 at 4.13 eV (300 nm). The multi-Gaussian peaks fit of the absorption spectrum of NRs with other ligands are displayed in the Appendix Figure A3 – A7.

To further quantify this observation, a multi-Gaussian peaks fit was applied to the absorption spectra. Seven Gaussians were needed to describe the absorption spectra's shape adequately. The multi-Gaussian peaks fit of TOPO-NRs is in Figure 4.10, and MUA-NRs, HS-PEG-OCH₃-NRs, DHLA-NRs, DHLA-PEG-NRs and PEI-NRs are placed in the Appendix as Figure A3 to A7. The details of the fitting parameters are listed in Table A3 in the Appendix. The peak position was determined as E_c , while $E_{c,1}$ referred to the first excitonic absorption peak of the CdSe core and $E_{c,2}$ referred to the absorption of the CdS shell directly surrounding the CdSe seed (referred to as “bulb” region).³³ The steady-state absorption peak change on the bulb region would also reflect the influence of the surface ligands, so this peak was taken into consideration in this chapter). $E_{c,3}$ to $E_{c,4}$ corresponded to the CdS rod based 1Σ ($1\sigma_e - 1\sigma_h$) and 1Π ($1\pi_e - 1\pi_h$) exciton transitions while $E_{c,5}$ and $E_{c,6}$ referred to even higher energy levels of CdS and the $E_{c,7}$ corresponded to the absorption into the continuum. All absorption features associated with the first excitonic CdSe absorption ($E_{c,1}$) showed nearly exact peak position (also considering the fitting errors) compared to $E_{c,1}$ in TOPO-NRs except for PEI-NRs which showed 10 – 20 meV blue shift. This was a strong indication of etching the CdS shell introduced by PEI and consisted with the argument by Woo.²¹³ Recent report proposed another explanation that amines not only passivated the surface atoms, but also shifted the energetic levels of both CB and VB.²¹⁴ Both of these arguments would further be proven by the bulb absorption ($E_{c,2}$) and CdS absorption ($E_{c,3}$) in PEI-NRs are shifted towards higher energies by 20 – 30 meV compared to TOPO-NRs, whereas NRs with other ligands show no to less

shift (considering the fit errors). All absorption feature associated with the higher excitonic energy levels ($E_{c,4}$ and $E_{c,5}$) in PEI-NRs were also shifted towards higher energies by more than 30 meV while NRs with other ligands showed also blues shift but only smaller. Higher absorption contributions of the CdSe core part at higher energy range resulted in larger fit errors. So $E_{c,4}$ and $E_{c,5}$ would not be intensively discussed here. Due to a much larger error while fitting, the $E_{c,6}$ and $E_{c,7}$ were also not included in this discussion.

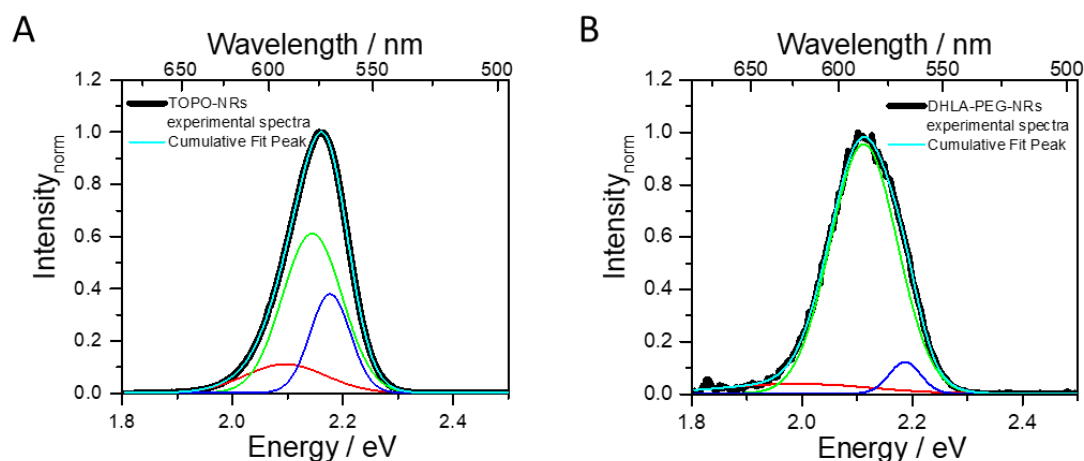


Figure 4.11. Multi-Gaussian peaks fit of the emission spectra of (A) TOPO-NRs in toluene and (B) DHLA-PEG-NRs in water excited at 400 nm and fitted using three Gaussians. The multi-Gaussian peaks fit of NRs with other ligands are displayed in the Appendix in Figure A8.

Even more pronounced shifts in the peak positions could be observed in the emission spectra in Figure 4.9B. For TOPO-NRs emission peaks at 2.16 eV and for both MUA-NRs and HS-PEG-OCH₃-NRs, the spectral shape and peak position of emission remains largely unaffected. PEI-coating, on the other hand, blue shifted the emission peak by 30 meV to 2.19 eV, while DHLA-PEG-NRs exhibit a very pronounced red shift of the emission peak by c. 30 meV to 2.13 eV. To further quantify the changes in their emissive behavior, emission spectra of the NRs were reconstructed using three Gaussians which described the shape of the emission spectra quite well. Based on the peak assignment in the previous chapter, three Gaussian peaks could be assigned as hole trap related emission (red peak in Figure 4.11), electron trap related emission (green peak) and intrinsic band gap emission (blue peak). All these Gaussian peaks were also found in the CdSe seed used for the core in NRs. Spectra of TOPO-NRs and DHLA-PEG-NRs described by three Gaussians are displayed in Figure 4.11. Spectra of all NRs with different ligands described by three Gaussians are displayed in Figure A8 in the Appendix and related fitting parameters were listed in Table A4 in the Appendix. The key parameters in the multi-Gaussian peaks fit were the position and the integral area of the peaks. The position of the peaks referred to the energetic gap related to different emission processes. The integral area of the peaks referred to the emission intensity of different emission processes. The results are displayed in Figure 4.12. By looking at Figure 4.12A, the peak positions of Gaussian peaks showed less differences in the blue peak, only

PEI-NRs showed slightly higher peak position due to slightly higher intrinsic bandgap introduced by etching of NRs due to ligand exchange of PEI. While in the green peak and red peak comparison, PEI-NRs still showed slightly higher peak position compared to NRs with other ligands, but DHLA-PEG-NRs showed significant lower peak position in the green and red peak. The slightly higher peak position of PEI-NRs in red and green peak was probably still due to the higher energetic level introduced by etching of PEI and the lower peak position of DHLA-PEG-NRs was probably due to the deep traps resulting in lower energetic difference of emission processes. In Figure 4.12B, the intensity of the Gaussian peaks was compared. In the red peak comparison, TOPO-, MUA-, HS-PEG-OCH₃-, and PEI-NRs showed more or less same emission intensity while DHLA- and DHLA-PEG-NRs showed lower proportion. This could be explained by deep hole traps introduced by DHLA and DHLA-PEG favored the non-radiative recombination processes resulting in less radiative recombination processes. By looking at the green peaks, the DHLA-PEG-NRs showed significant larger proportion compared to others due to the surface defects introduced by DHLA-PEG ligands. The PEI-NRs showed smallest proportion in the green peak due to best surface passivation of PEI that reduced the influence of the electron trap state. By looking at the blue peak, the DHLA-PEG-NRs showed smallest proportion, and this is still related to the surface defects. More pronounced non-radiative recombination of hole traps and higher proportion of electron trap related emission together contributed to this result. While the TOPO-, MUA-, HS-PEG-OCH₃-, and DHLA-NRs showed more or less the same proportions, the PEI-NRs showed the highest proportion due to better surface passivation resulting in the highest proportion in the intrinsic bandgap emission.

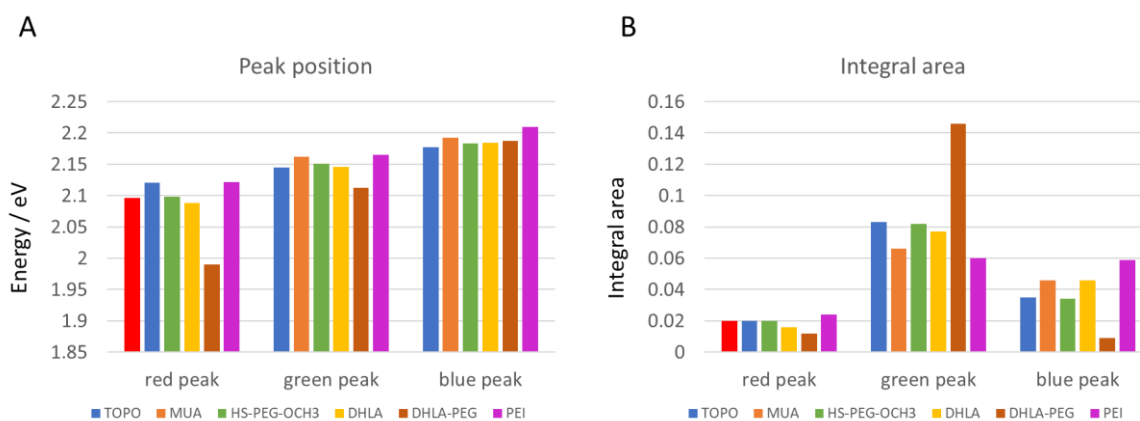


Figure 4.12. The (A) peak position and (B) integral area of the three Gaussian peaks introduced in the multi-Gaussian peaks fit of the emission spectra of NRs with different ligands.

After the above mentioned comparison, a few points were worth mentioning here.

- 1) By looking at the intrinsic band gap emission (blue peak), the PEI-NRs was dominated in this competition among different recombination processes. This was a strong indication of more radiative recombination in PEI-NRs than the other NRs, because more intrinsic band gap

emission meant less surface defect. This would further explain the highest value of PEI-NRs in the absolute PLQY measurement. DHLA-PEG-NRs showed the smallest contribution of the intrinsic band gap emission indicating the surface defect on the DHLA-PEG-NRs was much more pronounced than the others.

- 2) By looking at the electron trap related emission (green peak), only in DHLA-PEG-NRs, the electron trap emission was in domination in the competing processes completely. As mentioned above, the surface defect in DHLA-PEG-NRs was very pronounced resulting in deep traps favored the non-radiative recombination. While the influence of di-thiol ligands on electron trap related emission would be less pronounced due to the ligand bonding with Cd ion reducing the electron trap probability. This would further explain the red shifted peak position shift in DHLA-PEG-NRs compared to NRs with other ligands. The emission peak position of all NRs with different ligands was contributed by all these three Gaussian peaks related to different recombination processes. However, only in DHLA-PEG-NRs, the peak was mainly contributed by the electron trap related emission (green peak).
- 3) For all NRs, the hole trap related emission (red peak) were almost identical (errors considered) in peak position except for the DHLA-NRs and DHLA-PEG-NRs with a decrease peak area and the DHLA-PEG with a much broader hole trap related emission. This was not necessarily due to hole trap recovery because emission spectroscopy only revealed radiative recombination processes. The hole trap could be deeper compared to the NRs with other ligands due to the removal of Cd ions by the strong anchor group of dithiols by the free ligands during ligand exchanging^{215, 216} and then resulted in more non-radiative recombination. This would also explain the very small PLQY (0.01 for DHLA-PEG-NRs and 0.02 for DHLA-NRs) of the NRs with these two ligands.
- 4) When looking at PEI-NRs, even the experimental emission peak position of PEI-NRs showed obvious blue shift, the hole trap related emission peak position of PEI-NRs was in consist with the rest NRs indicating the CB and VB shift caused by PEI had much less pronounced influence on the relative energy gap between conduction band and hole trap state.

The emission property of DHLA-PEG-NRs could be introduced by different ligand exchange protocol. For MUA-NRs, DHLA-NRs and HS-PEG-OCH₃-NRs, the ligand exchange was conducted in a basic methanol environment. However, due to the hydrolysis of –COOR bond in DHLA-PEG ligand in basic environment the ligand exchange could only be performed in a neutral methanol environment with 60 °C heating for overnight. This could introduce more surface defects. PEI-NRs showed no shift in hole trap related emission but obvious blue shift in electron trap related emission and intrinsic band gap emission indicating the energetic band shift (or etching) caused by PEI have bigger influence on the emission processes related to the shell. Other NRs capped with MUA, HS-PEG-OCH₃, DHLA showed basically identical Gaussian peak positions compared to TOPO only with little difference in amplitudes

and peak areas. Also, the dramatic difference in PLQY of NRs with different ligands could be explained by surface defects. The PEI-NRs was passivated well with nearly $\Phi_{em} = 0.90$ and TOPO-NRs also with 30 – 50% coverage rate resulting in nearly $\Phi_{em} = 0.60$. The MUA-NRs and HS-PEG-OCH₃-NRs were capped with ligands through thiol groups which could passivate the electron traps but introduce hole traps resulting in around $\Phi_{em} = 0.20$. In the end, the PLQY of DHLA-NRs and DHLA-PEG-NRs were with the lowest $\Phi_{em} = 0.01 - 0.02$ due to the deep surface hole traps.

4.3 pH stability of NRs and discussion

The colloidal and pH stability are two crucial aspects when comes to practical application of the potential use of the NRs. Besides evaluating the properties in pure water, both absorption and emission spectra of NRs in aqueous solution under standard atmosphere at varying pH value were recorded.

In phosphate-buffered saline (PBS) with a concentration of 50 mM, MUA-NRs showed very poor stability with nearly instant aggregation at pH 5, while in pH 7 buffer, slower aggregation occurs spanning a time range of several hours. In pH 9 buffer, the MUA-NRs were stable for days. To probe the impact of the buffer solution and its ionic strength on the NRs stability, the same experiment was conducted with HCl solution at pH 5. In stark contrast to previous literature reports, the MUA-NRs were stable without any aggregation at pH 5 HCl solution within a comparable time scale. However, a discoloration of the MUA-NRs in HCl solution was observed within days due to the reaction between CdS (or CdSe) and HCl. DHLA-NRs should have the similar pH stability due to the same hydrophilic group.

Knowing the pH instability of MUA- and DHLA-NRs, for the rest NRs capped with different ligands, measurements were taken under pH 5 to 9 on the timescale of 1h, the results was clearly illustrated in time-lapse UV/Vis absorption spectra. The HS-PEG-OCH₃-NRs showed quite impressive colloidal stability in pH 7 and pH 9 buffers in terms of nearly unchanged absorption and emission spectral shape. While in pH 5 buffer, even if the emission intensity and the absorbance of the HS-PEG-OCH₃-NRs was dropping at the same time as measuring time went, the calculated relative PLQY of the HS-PEG-OCH₃-NRs stayed at around 0.15 for 1 hour. In the time-lapse absorption spectrum of HS-PEG-OCH₃-NRs, as displayed in Figure 4.13(A – C), HS-PEG-OCH₃-NRs showed decreased absorbance over time in pH 5 buffer, constant absorbance in pH 7 buffer and a decreased but scattered absorbance in pH 9 buffer. Worth mentioning here, the time-lapse absorption measurement was only a rough way to determine the scattering or aggregation process. Dynamic light scattering would be a more precise method to evaluate this process.

Time-lapse emission spectroscopy was also introduced here to validate the colloidal stability of the NRs. In the time-lapse emission spectrum of HS-PEG-OCH₃-NRs which is displayed in Figure 4.13(D – F), only in pH 5 buffer the emission intensity dropped over time while in pH 7 and pH 9 buffer the emission

intensity stayed constant in 60 min time scale. If compared to the emission intensity of HS-PEG-OCH₃-NRs in water, the emission intensity of HS-PEG-OCH₃-NRs in pH 5 and pH 9 was dropped but in pH 7 the emission intensity increased. (To really compare the emission intensity, PLQY need to be introduced. However, it would be difficult to calculate relative PLQY with scattering samples. In this chapter, because all samples showed tiny changes in absorption even when scattering, the emission intensity comparison was roughly carried out by comparing the maximum signal of each emission spectrum.) The properties of HS-PEG-OCH₃ benefit NRs with high colloidal stability in wide pH range from pH 5 to 9.

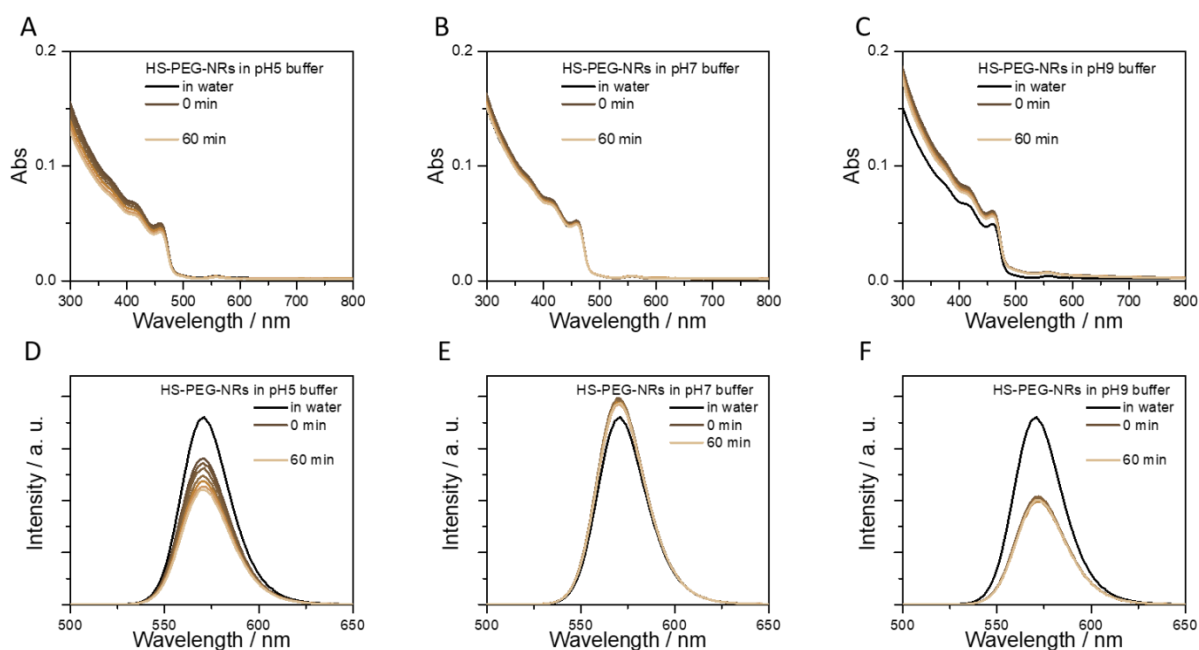


Figure 4.13. The time-lapse absorption spectrum of HS-PEG-OCH₃-NRs in different pH values in a time scale of 60min, (A) pH 5, (B) pH 7, (C) pH 9 and the time-lapse emission spectrum of HS-PEG-OCH₃-NRs in the same conditions, (D) pH 5, (E) pH 7, (F) pH 9. Excitation wavelength was 400 nm.

The DHLA-PEG capped NRs were found to be stable at all pH values investigated, at least to an extent that no severe aggregation and formation of precipitate can be observed by naked eye. In the time-lapse absorption spectra, displayed in Figure 4.14(A – C), an instant but constant scattering background was presented, which could indicate the formation of small clusters but still being stable in dispersion. This scattering effect was slightly developing during the measurement. In Figure 4.14(D – F), the colloidal stability of DHLA-PEG-NRs were good in terms of emission intensity change during 1h in pH 5 and pH 7 buffers but something different was found in pH 9 buffer, where the emission intensity was dropping even the absorbance was not change dramatically.

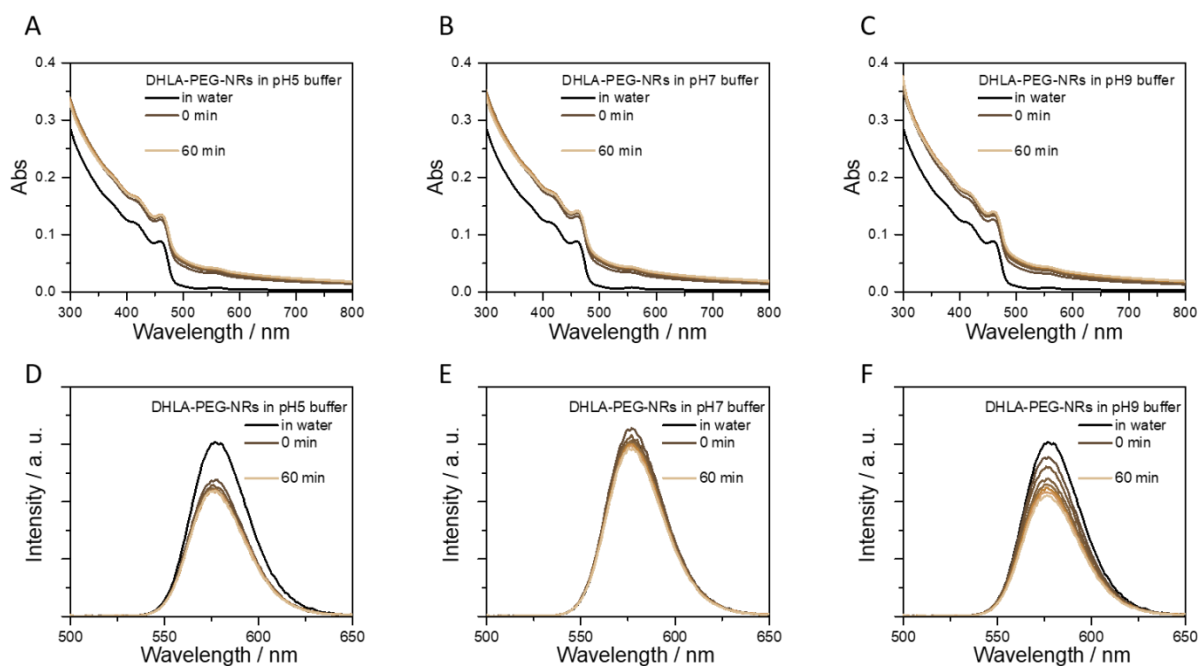


Figure 4.14. The time-lapse absorption spectrum of DHLA-PEG-NRs in different pH values in a time scale of 60min, (A) pH 5, (B) pH 7, (C) pH 9 and the time-lapse emission spectrum of DHLA-PEG-NRs in the same conditions, (D) pH 5, (E) pH 7, (F) pH 9. Excitation wavelength was 400 nm.

The PEI-NRs in pH 5 and pH 7 buffers were cloudy as could be seen by eyes. In the time-lapse absorption spectrum as shown in Figure 4.15(A-B), the differences between PEI-NRs NRs in pH 5 and pH 7 buffers and in deionized water were obvious and they were introduced by the ligand PEI itself which had been tested with pure PEI in respective buffers (data were not shown). However, when came to time-lapse emission spectrum as shown in Figure 4.15(D – E), the emission peak was red shifted to 2.18 eV (568 nm) when PEI-NRs NRs were added into the buffer. This could be explained by the removal of surface capped PEI ligands and the possible associated NRs aggregation. Because the PEI was found with a relatively high stability of the imine bond at pH 8, while fast cleavage occurred at pH 5 – 7. In pH 9 buffer, PEI-NRs NRs showed excellent colloidal stability in terms of nearly unchanged absorption spectrum in Figure 4.15C and emission intensity in Figure 4.15F.

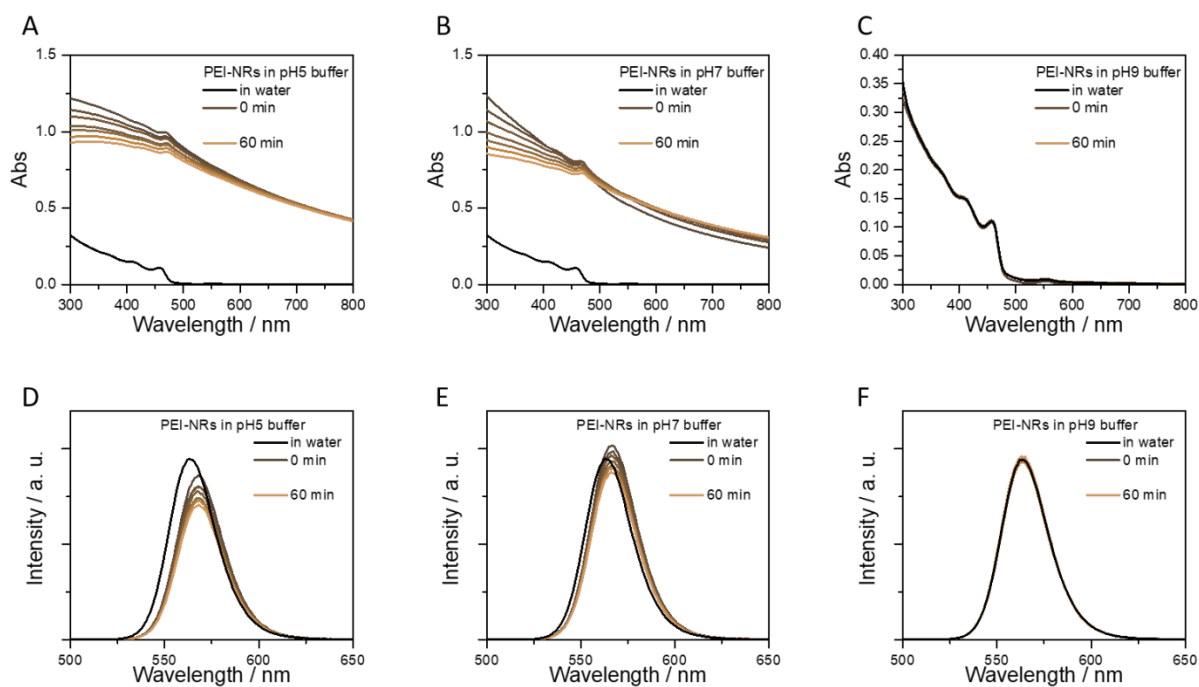


Figure 4.15. The time-lapse absorption spectrum of PEI-NRs in different pH values in a time scale of 60 min, (A) pH 5, (B) pH 7, (C) pH 9 and the time-lapse emission spectrum of PEI-NRs in the same conditions, (D) pH 5, (E) pH 7, (F) pH 9. Excitation wavelength was 400 nm.

MUA-NRs and DHLA-NRs were soluble in polar solvents like methanol and water.¹⁵⁰ DHLA-PEG-NRs¹⁵¹ and HS-PEG-OCH₃-NRs were soluble in both non-polar and polar solvents due to the solubility of long PEG chain in both non- and polar solvents. The MUA-NRs showed excellent stabilities in pH 9 buffer while in pH 7 buffer the MUA-NRs aggregate gradually in hours and in pH 5 buffer the aggregation happens instantly. This is used to be explained by the protonation of the MUA results in reduced surface charge and aggregation.⁷⁸ However, our investigation with pH 5 HCl solution showed that the MUA-NRs were stable in pH 5 HCl solution for hours without any aggregation but followed by discoloration due to the reaction between CdS, CdSe and HCl. This led us to a result that the main reason for the aggregation in pH 5 buffer was not the protonation of the MUA but could be explained by the interaction between MUA and ions in the buffer system resulting in the lack of electric repulsing. The DHLA-PEG-NRs exhibited good pH stability in pH 5 to pH 9 buffer only with an absorption (to be more precise, the extinction) increasing (compared to water: 33.1% for pH 5, 39.6% for pH 7 and 36.2% for pH 9) due to scattering effect. The absorbance appears to be increasing with time indicating the clusters are still forming even after the DHLA-PEG-NRs are added into the buffer for 1h. Time-lapse emission spectroscopy shows that the DHLA-PEG-NRs exhibit lower emission intensity in pH 5 and pH 9 buffer but relative similar emission intensity in pH 7 buffer compared to the emission intensity in water. DHLA-PEG-NRs in pH 9 in 1h showed largest emission intensity decrease at about 24% while in pH 5 7.9% and pH 7 12%. So, basically the DHLA-PEG-NRs are quite stable in pH 5 and pH 7 but less stable in pH 9 probably due to the basic hydrolysis of the -COOR bond in DHLA-PEG ligand. The

HS-PEG-OCH₃-NRs showed excellent stability in pH 7 and pH 9 buffer in both time-lapse absorption and emission measurement, only in pH 5 buffer the absorbance and emission drop over time and it seemed to be a degrading over time. However, the relative QY calculation shows that the QY stays constantly at Φ_{em} 0.15. It was not surprising that the HS-PEG-OCH₃-NRs are much more stable in pH 9 buffer than DHLA-PEG-NRs due to the lack of -COOR group. The PEI-NRs are very interesting from the results. They show instability in pH 5 and pH 7 buffer with huge scattering in absorption and decrease with peak red shift in emission spectra. The absorption scattering came from the ligand which was confirmed by measuring the pure ligand and the emission red shift probably due to the removal of surface capped PEI ligands. The solubility of PEI-NRs was slightly different from its pure ligands. The pure PEI was soluble in most of the solvents except cyclohexane, it was soluble in non-polar solvents like chloroform and toluene and polar solvents like methanol and water. However, after precipitation from chloroform with cyclohexane, the PEI-NRs could no longer be dispersed in chloroform again due to the change of stabilization mechanism from steric stabilization to electrostatic stabilization.¹⁵² In pH 9 buffer, PEI-NRs showed excellent colloidal stability in terms of nearly unchanged absorption spectrum and emission intensity. Generally, depend on pH stability results, if application was in basic media, the MUA-NRs and PEI-NRs were the best choice and if application was in a larger pH range, the DHLA-PEG-NRs and HS-PEG-OCH₃-NRs were better choices.

4.4 Time-resolved investigation on NRs and discussion

4.4.1 Time-resolved emission lifetime on NRs and discussion

To gain some deeper understanding of the radiative recombination processes in NRs with different ligands, the time resolved PL lifetime measurement was introduced. The samples were prepared and measured in an inert atmosphere with optical density of around 0.3. The results of emission lifetime were plotted in Figure 4.16 and summarized in Table 4.8. The fitting processes were done by software Decayfit version 1.4. Also, the deconvolution of the traces was done by the same software to exclude the influence of IRF. The TOPO-NRs and MUA-NRs exhibited mono-exponential decay behavior with a decay lifetime of 20.6 ns and 24.8 ns, respectively. For the rest, DHLA-NRs, DHLA-PEG-NRs, HS-PEG-NRs, and PEI-NRs all exhibited bi-exponential decay behavior. The fast decay lifetimes of these NRs were in sub-ns scale while the slow decay lifetimes were longest for PEI-NRs as 19.9 ns, shortest for DHLA-PEG-NRs as 6.2 ns. The DHLA-NRs and HS-PEG-NRs showed relative intermediate decay lifetime as 10.1 ns and 16.9 ns. In the classification of different anchor groups, monothiols (MUA-NRs and HS-PEG-NRs) showed rather long decay lifetime while di-thiols (DHLA-NRs and DHLA-PEG-NRs) showed rather short decay lifetime. In the classification of the hydrophilic segment, the carboxylates (MUA-NRs and DHLA-NRs) showed longer emission lifetime compared to their

PEG chain form (HS-PEG-NRs and DHLA-PEG-NRs). As a short conclusion here, additional thiol group in the anchor group accelerate the decay of emission lifetime while additional PEG chain has the same effect.

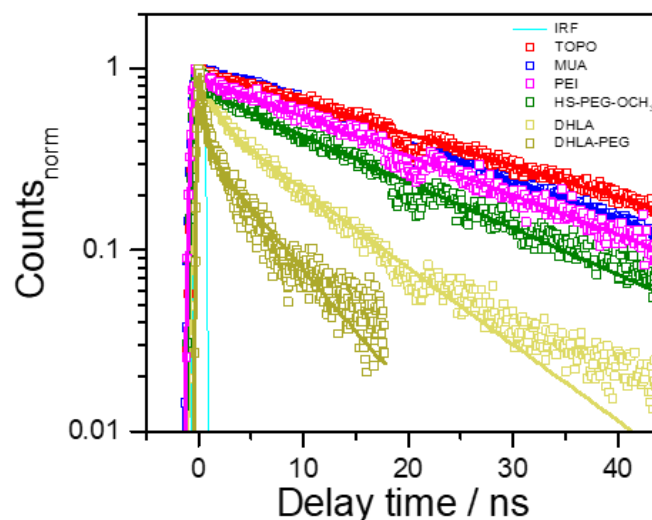


Figure 4.16. The emission lifetime of NRs with different ligands. TOPO-NRs were measured in toluene and the rest were measured in water. The excitation wavelength was 400 nm.

As the emission lifetime of TOPO-, MUA-, and PEI-NRs were all located in the range of 20 – 25 ns, their absolute PLQY were of huge differences. The PLQY of TOPO-NRs was about 0.60 and MUA-NRs was about 0.25 and PEI-NRs was nearly 0.90. This could be explained by better surface passivation of PEI. TOPO which passivated the Cd ion with 30 – 50% coverage rate, left Cd ion and Se site as electron trap and hole trap, respectively. The non-radiative recombination processes made TOPO-NRs only with 0.60 in PLQY. As for MUA-NRs, the thiol groups acted as electron trap passivator but at the same time introduced hole trap. So, MUA-NRs only resulted in 0.25 in PLQY. The same theory would also make sense on DHLA-NRs, where the DHLA introduced even deeper hole traps due to Cd^{2+} removal by strong dithiol anchor group (see section 4.2), which would result in a faster decay compared to MUA-NRs. The influence of PEG chain was still unclear at this stage, the emission lifetime was shorter compared to MUA-NRs and it was clearly that the PEG chain did not introduce more hole trap because the PLQY of MUA-NRs and HS-PEG-OCH₃-NRs were comparable. So, it might be explained by less electron trap passivation due to the large volume of PEG chain. As for DHLA-PEG-NRs, with above mentioned influence of dithiol group and PEG chain, the explanation would be much easier that both hole and electron trap were introduced resulting in the shortest emission lifetime.

Table 4.8. Fitting results of the emission lifetime of NRs with different surface ligands by Decayfit. Indicated are the fast decay lifetime τ_1 , slow decay lifetime τ_2 and their amplitude A_1 and A_2 , respectively. The sum of A_1 and A_2 is 1. * TOPO-NRs and MUA-NRs showed single exponential decay behavior, the decay lifetimes were assigned to slow decay lifetime as τ_2 .

Parameter	TOPO-NR	MUA-NR	DHLA-NRs	DHLA-PEG-NR	PEI-NR	HS-PEG-NR
τ_1 / ns	—*	—*	1.1	0.5	0.2	0.8
A_1	—*	—*	0.54	0.70	0.37	0.35
τ_2 / ns	20.6	24.8	10.1	6.2	19.9	16.9
A_2	—*	—*	0.46	0.30	0.63	0.65

4.4.2 Transient absorption measurements on NRs and discussion

While above results already painted a consistent picture of the photophysics of the NRs investigated. Transient absorption spectroscopy delivers information on the temporal evolution of electrons excited to the CdS and CdSe conduction bands.²¹⁷ The sample was excited at 390 nm and probed with a white light continuum spanning from 2.33 – 3.54 eV (350 nm to 700 nm) up to a delay time of 1700 ps. It was worth to be mentioned here that at the power density used in the transient absorption experiments, excitation at upon 3.17 eV (390 nm) directly excited mainly CdS electrons to the CB, and also to a much smaller extent CdSe electrons to the CB via direct light absorption. Qualitatively, the transient spectra for all NRs presented similar features compared to TOPO-NRs (transient spectra of TOPO-NRs at different delay times were described as the dot-in-rod NRs in Figure 3.9A in previous chapter already): (1) Two bleaches appeared at 460 nm (2.70 eV) referring to the CdS bleach and at 560 nm (2.21 eV) referring to the CdSe bleach. (2) A positive excited state absorption feature rise at 430 nm (2.90 eV). (3) Both bleach features did not fully decay until the end of the temporal detection window employed due to limited length of the mechanical delay stage (shown in Figure 3.9B). In the meanwhile, the changes at the position of bleach minimum were well in agreement with the peak shifts in both absorption and emission spectrum of the respective ligand capped NRs.

A global fit of the TA data would deliver a quantitative data analysis on the electron kinetics of the NRs. The DAS in this chapter only revealed in a relatively small wavelength range (10 nm range centered at the bleach signal minimum) but not full spectra range, because the time components needed for fitting were not the same at different bleaches. With the discussion on the time components assignment in the previous chapter on TOPO-NRs, the time components assignment in MUA-, HS-PEG-OCH₃-, DHLA-, DHLA-PEG- and PEI-NRs would also be obtained. Global fit of TOPO-NRs and the DAS were displayed in Figure 4.17 and the fitting parameters were listed in Table 4.9. And NRs with different ligands together with DAS are

displayed in Figure A9 – A13 in the Appendix and fitting parameters are also displayed in Table 4.9.

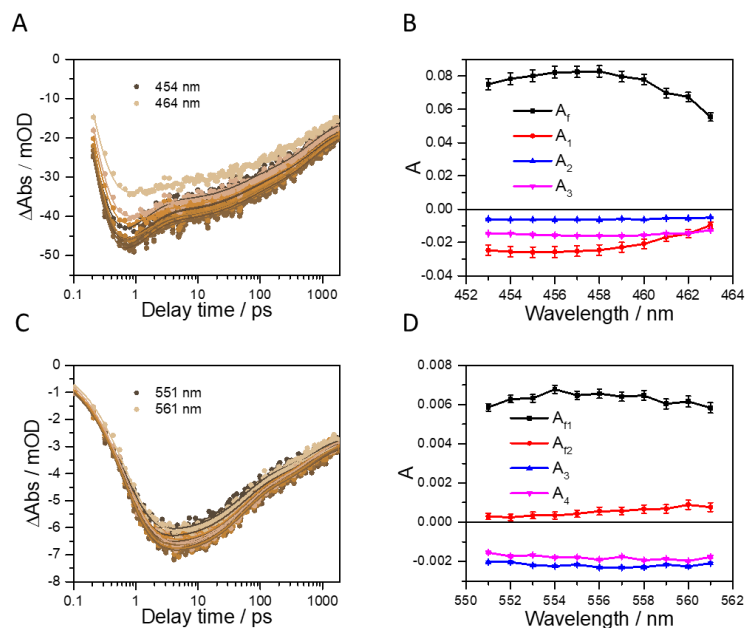


Figure 4.17. The global fit of TOPO-NRs kinetics, (A) 10 nm scale centered at CdS bleach signal minimum 458 nm and (C) 10 nm scale centered at CdSe bleach signal minimum 556 nm. The DAS of global fit of (B) CdS and (D) CdSe parts, respectively. The global fit of NRs with other ligands are displayed in the Appendix Figure A9 – A13.

Table 4.9. Transient absorption spectroscopy on NRs with different surface ligands. Time constants were obtained by a global fit within the indicated wavelength range. For the CdS, wavelength centered at around 455 nm. For the CdSe, wavelength centered at around 550 nm.

Ligand	range	τ_{f1} / ps	τ_{f2} / ps	τ_1 / ps	τ_2 / ps	τ_3 / ps
TOPO	454 – 464 nm	0.1 ± 0.1	—	1.3 ± 0.1	52 ± 3	683 ± 32
	551 – 561 nm	0.6 ± 0.1	2.4 ± 0.5	—	49 ± 1	683 ± 35
MUA	454 – 464 nm	0.1 ± 0.1	—	0.8 ± 0.2	75 ± 10	726 ± 60
	551 – 561 nm	0.3 ± 0.1	1.3 ± 0.2	—	63 ± 3	1104 ± 95
HS-PEG-OCH ₃	455 – 465 nm	0.1 ± 0.1	—	0.4 ± 0.1	61 ± 4	851 ± 51
	555 – 565 nm	0.2 ± 0.1	0.9 ± 0.1	—	48 ± 2	773 ± 40
DHHLA	454 – 464 nm	0.1 ± 0.1	—	3.3 ± 0.2	95 ± 6	916 ± 72
	549 – 559 eV	0.4 ± 0.1	2.0 ± 0.4	—	77 ± 5	1055 ± 98
DHHLA-PEG	457 – 467 nm	0.1 ± 0.1	—	1.7 ± 0.1	88 ± 7	608 ± 58
	552 – 562 nm	0.3 ± 0.1	3.5 ± 1.4	—	61 ± 14	551 ± 79
PEI	451 – 461 nm	0.1 ± 0.1	—	0.9 ± 0.1	30 ± 1	440 ± 16
	545 – 555 nm	0.9 ± 0.1	8.8 ± 1.4	—	47 ± 2	841 ± 57

There was only slight difference in the signal formation part in both CdS and CdSe part that the time component (τ_{f1}) of CdSe (0.2 – 0.9 ps) was longer than the formation time (τ_{f1}) of CdS (0.1 ps). But in the decay part of the CdS kinetics, comparable decay time component (τ_1) in NRs capped with different ligands (1.0 ~ 3.0 ps) indicating electron localization process to the shared CB was comparable among these NRs with different ligands. The τ_2 of TOPO-, MUA-, HS-PEG, DHLA-PEG-NRs were all in a time range of 30 – 100 ps while TOPO-NRs and PEI-NRs showed τ_2 faster at 30 – 50 ps and DHLA-NRs and DHLA-PEG-NRs exhibited τ_2 slower at ~ 90 ps. This could be explained by a better surface passivation of TOPO and PEI results in less surface defect favoring the recombination process while DHLA would introduce more surface defect. This would also explain the similar feature in τ_3 , that DHLA-NRs showed longer decay time component than the rest NRs. In the second part of signal formation in CdSe, the τ_{f2} was in a range from 1 – 9 ps. This process referred to the hole localization driven electron localization to the CB of CdSe due to Coulombic interaction. The τ_{f2} in TOPO-, MUA-, HS-PEG-OCH₃-, DHLA- and DHLA-PEG-NRs were in faster range 1 – 3 ps while PEI-NRs were slower at ~ 9 ps due to the competing processes between surface defects and hole localization in CdSe. The more surface defects on the CdS part, the more pronounced trap of holes would be on the CdS part, therefore, the less population of electron localization driven by hole localization could be observed on the CdSe part resulting in shorter formation time component τ_{f2} . The illustration of the related processes was displayed in Figure 4.18. In the decay part of CdSe kinetics, influence of surface defect was not so pronounced in τ_2 but more pronounced on the MUA-, HS-PEG-OCH₃-NRs that the τ_3 exhibited much slower decay time (700 – 1000 ps) compared to TOPO-NRs and PEI-NRs (400 – 600 ps).

The decay associated spectra (DAS(τ_n)) was also introduced here to reveal the spectral changes associated with different decay time constants τ_n . All DAS showed similar shape with one positive band and three negative bands in the CdS part and two positive bands and two negative bands in the CdSe part with comparable amplitudes. The worth mentioning difference would be the DAS(τ_1) (red line named A₁ in Figure 4.17B and A9 – A13B) in CdS part showed a trend towards positive at the end of the fit range. This would explain by the localization of electrons to the CdS bulb region. Also, the first half of DAS(τ_1) in CdS part of PEI-NRs (red line in Figure A13B in the Appendix) was almost double the amplitudes of the DAS(τ_2) (blue line in A13B) and DAS(τ_3) (magenta line in A13B) indicating that the depopulation of electron on the CdS CB to the CB of CdSe part due to hole localization was favored because of the better surface passivation of PEI. Meanwhile, the offset (y_0) of both CdS and CdSe part of the DHLA-PEG-NRs (green line in Figure A12B and A12D) were almost doubled compared to the DAS(τ_2) (blue line in Figure A12B and A12D) and DAS(τ_3) (magenta line in Figure A12B and A12D) while the rest showed comparable amplitude in the DAS of NRs with other ligands. This could be

explained by the more surface defects in the DHLA-PEG-NRs resulting in much longer recombination time compared to NRs with other ligands.

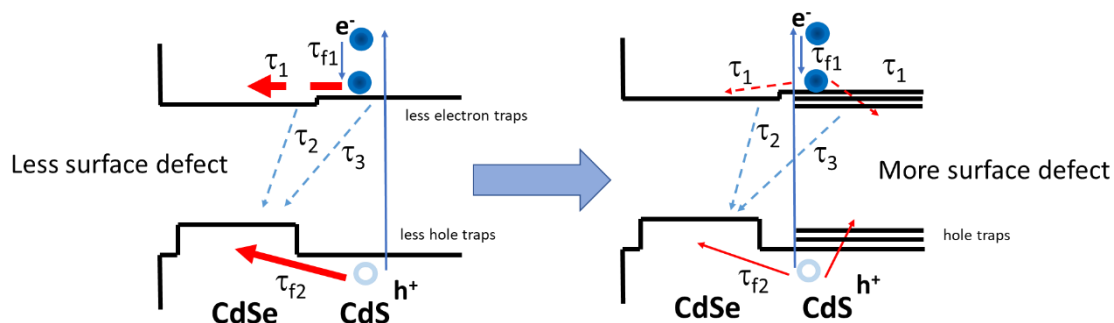


Figure 4.18. The illustration of the influence of surface defects on the carrier dynamics. The solid arrows referred to the excitation and signal formation time components (τ_{f1} and τ_{f2}) and the dashed arrows referred to the signal decay time components (τ_1 , τ_2 and τ_3). The assignment of the processes referring to the blue arrows were already discussed in reported literature.⁹² The key results in this thesis were the assignment of the influence of surface defects on the first decay time component of CdS (τ_1) and the second formation time component τ_{f2} of the CdSe (τ_{f2}) as red arrows. (The bigger arrow meant this process was favored under the certain condition). The hole localization driven electron localization on the CB of the CdSe core was favored with less surface hole traps. However, when the hole traps were more pronounced, the hole localization driven electron localization would undergo competing processes between trapped holes and localized holes at the CdSe core. Furthermore, the surface defects caused electron trap states would also competing with the hole localization driven electron localization. If the surface of the CdS rod was well passivated like PEI-NRs, the surface states of the CdS part would be only shallow states or nearly unity. Then the hole localization at the CdSe core was favored resulting in larger associated amplitudes compared to the NRs with other ligands. If the surface defects of the CdS rod were more pronounced, like the DHLA-PEG-NRs, the surface states of the CdS part would be more likely to be pronounced and dominate the competing processes of hole localization at the CdSe core and hole traps and electron traps at rod surface resulting in smaller amplitudes of (τ_1) and a shorter time component (τ_{f2}).

4.5 Conclusion

In this chapter, we successfully synthesized and transferred CdSe/CdS dot-in-rod NRs into water using MUA, HS-PEG, DHLA, DHLA-PEG and PEI as surface ligands. The distribution of TOPO-NRs was determined by TEM and the ligands exchange was monitored by FTIR. The steady-state absorption revealed different energy levels in the NRs with different ligands. All energy levels related absorption peaks in NRs were comparable except for PEI-NRs showed blue shifted peaks indicating the energetic shift of bands in PEI-NRs. This was further confirmed by steady-state emission measurements that only

PEI-NRs showed blue shift in the electron trap state related emission and band gap emission but no obvious change in the hole trap state related emission. The emission red shift caused by DHLA-PEG was explained by different contribution of above-mentioned emission processes. Although emission lifetime were comparable in TOPO-, MUA-, PEI-NRs, the PLQY were differed dramatically due to the best surface passivation of PEI recovered the non-radiative recombination processes while TOPO could only passivate partial exposed site on the NRs surface. The emission lifetime of HS-PEG-OCH₃-, DHLA-, DHLA-PEG-NRs was much faster compare to NRs with other ligands, this is explained by the surface defects introduced by PEG chain (less passivation due to large volume of PEG) and dithiol anchoring group (more exposed S sites on the rod surface due to stronger anchoring group compared to monothiol anchoring group). Transient absorption results showed that the electron dynamics were of little differences in all NRs in the employed time window with only minor difference in signal decay time components. The competing processes of the trap states and hole localization played an important role here resulting in different time components and associated amplitudes. The DHLA ligand introduced more surface defects resulted in longer recombination processes. And PEI ligand introduced better surface passivation resulted in longer hole localization time component and shorter recombination processes. The pH stability test revealed the instability of MUA-NRs and PEI-NRs in acidic buffer and the high stability of DHLA-PEG-NRs in acidic buffer and HS-PEG-OCH₃-NRs in acidic, neutral, and basic buffers.

There was no perfect one-for-all solution when choosing the surface ligands for practical applications, however, HS-PEG-NRs stand out due to high photoluminescence and excellent pH stability in a wide range of pH values (from pH 5 to 9). While PEI showed great potential in catalysis applications due to the best surface passivation resulting in faster electron transfer.

CHAPTER 5.

The interaction between CdSe/CdS dot-in-rod NRs and dopamine / polydopamine

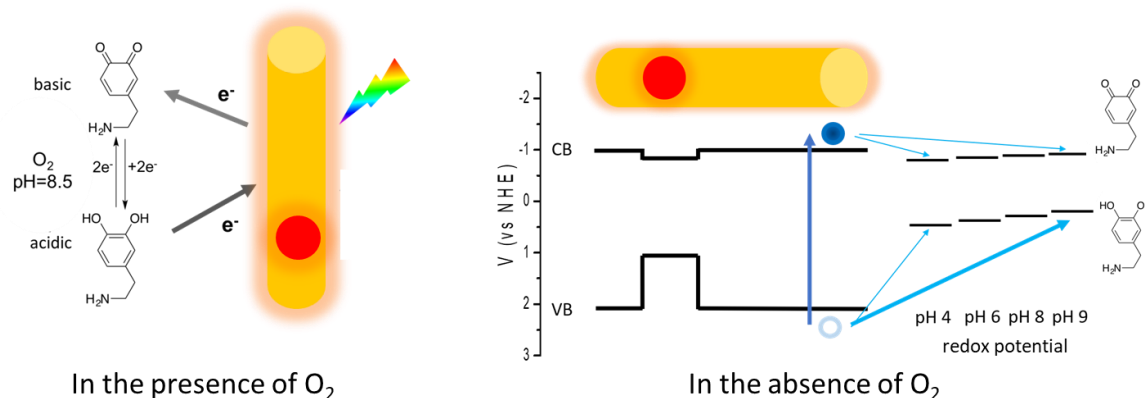


Figure 5.1. Illustration of the possible interactions between a dot-in-rod NR and dopamine in the presence of and in the absence of O₂. When oxygen is in the presence, the dopamine would be oxidized to quinone groups in basic condition. The quenching would be dominated by electron transfer from the NRs to quinone groups. When oxygen is in the absence, the dopamine is in the catechol form. The quenching would be dominated by hole transfer from the NRs to the catechol groups and based on the redox potential of free dopamine, this hole transfer is favored at higher pH value while the driving force of electron transfer is much less compared to the driving force of the hole transfer. The redox potential of dopamine in the catechol and quinone forms were calculated based on the reported results.²¹⁸

By far, the structure and surface ligands of CdSe/CdS dot-in-rod NRs were already discussed together with the related potential applications introduced in previous chapters. However, the problem of degradation caused by residuary photogenerated holes, which was a common problem for most photoactive materials, still limits the application of the NRs. The degradation gave a drawback to ensure long term stability for device application. By designing a system where photoactive rods are embedding into a compact, rigid, redox-active polydopamine matrix would give the possibility to prevent this kind of photoinduced degradation. The interaction between dopamine molecules and quantum dots were already investigated. CdSe quantum dots derivatives were introduced to detect dopamine already by the electrochemiluminescence²¹⁹⁻²²³ and photo-luminescence²²⁴⁻²²⁶ And CdSe quantum dots derivatives were also used in pH sensing associated with dopamine ligands.^{218, 227, 228} Polydopamine is a typical redox-active polymer that can be easily coated on nearly any surface by dip-coating or electrochemical coating.²²⁹ The electrochemical coating was very suitable for coating on a conductive substrate (e.g., Si,

Au or ITO substrates), corresponding to thin films with high chemical, thermal stability and long lifetime.^{230, 231}

The polydopamine coating could be achieved in buffer system like Tris-buffer²³² and PBS-buffer²³³ in alkaline pH in the presence of oxygen. The polymerization mechanism in alkaline pH involves slow oxidation of dopamine to dopamine quinone through a one step, two-electron redox reaction,²³⁴ which rapidly undergoes Michael-type intramolecular cycloaddition reaction forming leucodopaminechrome. Then, the oxidation of leucodopaminechrome and rearrangement results in the formation of 5,6-dihydroxyindole and 5,6-indolequinone. These two molecules will undergo branching reactions at positions 2, 3, 4 and 7 resulting in different dimers or higher order oligomers, which will eventually forming thin polydopamine film coating on substrates or targets.²³⁵

Polydopamine contains both catechol and quinone groups, which are in pH-dependent redox equilibrium with each other. When interacting with CdSe/CdS dot-in-rod NRs, quinone groups that dominate at basic pH values might act as electron acceptors and when interacting with the NRs with a catalytic center, the quinone groups might even intercept the electron transfer from the excited NRs to the catalytic reaction center, like a tunable switch to turn on and off the catalytic reaction by adjusting the pH values. Catechol groups which dominate at acidic pH values can act as hole quencher and remove the residuary photogenerated holes to protect the NRs from degrading. Therefore, the electron or hole transfer would result in emission quenching used for qualitative or quantitative investigation. By adjusting the pH, the domination of catechol groups or quinone groups could be tuned. These mechanisms need to be studied with the detailed spectroscopic investigation.

Herein, this chapter studied the interactions between rods and polydopamine starting with the most basic system of these two species, water-soluble NRs and dopamine molecules which have the same groups transformation as the polydopamine under certain pH and oxygen conditions. Figure 5.1 shows the illustration of possible interactions between nanorod and dopamine. Both oxidized and reduced form of dopamine and the equilibrium in dependence on pH value were shown. In this chapter, NRs referred to the CdSe/CdS dot-in-rod NRs.

5.1 The interaction between MUA-NRs with dopamine molecules

Water-soluble NRs with 11-mercaptoundecanoic acid as surface ligands (MUA-NRs) were already obtained in previous chapters. Absorption and emission spectra of MUA-NRs were plotted in Figure 5.2. (Please be aware that the MUA-NRs used in this chapter were not the same batch used in chapter 4. The MUA-NRs used in this chapter were about 50 nm in length and 5 nm in width which might result in different optical properties, like absorption peak and emission peak positions.) In the absorption spectrum, the small peak around 555 nm was the first excitonic absorption peak of CdSe core, and the

peak around 455 nm was the first excitonic absorption peak of CdS shell. After excitation at 450 nm, the rods showed an emission peak around 570 nm. The quantum yield (QY) of this batch of MUA-NRs was 0.30 when the rods were freshly synthesized determined by an excitation wavelength of 450 nm.

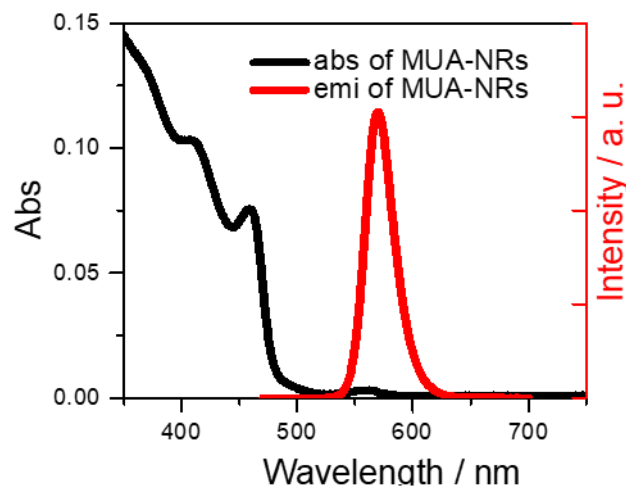


Figure 5.2. The absorption and emission spectrum of MUA-NRs in water. The excitation wavelength was 450 nm.

To understand the basic interaction between MUA-NRs and dopamine, a quenching experiment was carried out, where MUA-NRs were used as the emitter, and dopamine was used as the quencher. Since the key parameters of the equilibrium between catechol and quinone forms of dopamine were pH value and oxygen, the pH value and oxygen level should be carefully handled in the quenching experiments. Phosphate buffered saline (PBS) with 50 mM in concentration from pH 8 to pH 10 was introduced to maintain the pH values across each quenching experiment to investigate the influence of pH values in quenching experiments (the rods with MUA ligand showed poor colloidal stability in buffer lower than pH 8). PBS in the presence and absence of oxygen was also introduced to investigate the influence of oxygen on quenching experiments. The MUA-NRs emission spectrum was recorded in the presence and absence of dopamine in water with excitation wavelength at 450 nm. After recording the initial emission intensity of rods, different amounts of dopamine were added into the same cell which holds the MUA-NRs solution. After each time adding dopamine, the emission spectrum was recorded. An example of emission spectra in the quenching experiment in pH 9 in the absence of oxygen was shown in Figure 5.3. The emission intensity was decreasing as the concentration of dopamine increased. Worth mentioning here, the concentration of NRs was calculated here using a reported method to give a basic idea of the ratio between emitter and quencher.²³⁶ The relationship of the extinction coefficient of NRs at 350 nm is displayed here as Equation 5.1:

$$\varepsilon = 28326.9 \frac{L}{\text{mol} \cdot \text{cm} \cdot \text{nm}^3} \cdot V \quad (5.1)$$

where V was the total rod volume in nm which could be determined by TEM image. Then the concentration could be obtained by the Lambert-Beer's law. The concentration of NRs was calculated to be around 1.4×10^{-8} M. The concentration of dopamine was designed to be 0.2×10^{-8} M with each single titration step (also referred to each single trace in Figure 5.3). So, the ratio between quencher and emitter was 0, 0.14, 0.29, 0.43, 0.57, 0.71 when 0, 2, 4, 6, 8, 10 μ M dopamine was added in the experiment. But these numbers were only estimated numbers because each method reported calculating the extinction coefficient was an estimated method. The absorption peaks of dopamine were at 230 nm and 280 nm (not shown in the figure), so there was no overlap between the absorption spectrum of the quencher and the emission spectrum of the emitter. In this case, the electron transfer mechanism was a more reasonable explanation for quenching.

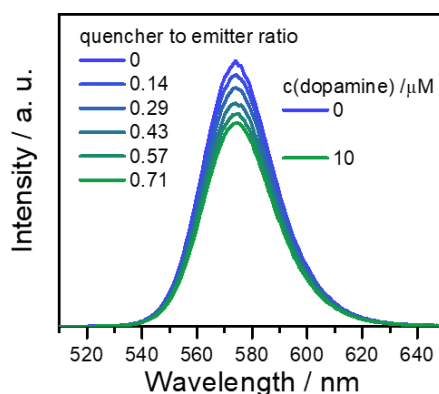


Figure 5.3. The emission spectra of MUA-NRs in pH 9 PBS buffer in the absence of oxygen with different amounts of dopamine added. The quencher to emitter ratio was also displayed. The excitation wavelength was 450 nm.

The quenching efficiencies in different pH values, both in the presence and absence of oxygen, were shown in Figure 5.4. The quenching efficiency E_Q is determined by:

$$E_Q = 1 - (I/I_0) \quad (5.2)$$

where I_0 and I were the emission intensities determined by the integral of emission peak in the absence and presence of quencher, respectively. The emission intensity was determined as the integrated fluorescence intensity. Two basic conclusions could be drawn from Figure 5.4: 1) the quenching was more dramatic as the pH values increasing from 8 to 10. The quenching efficiency in pH 8 in the presence of oxygen was only 0.4 with 10 μ M dopamine (Figure 5.4B) but increased dramatically to 0.8 in pH 9 buffer and 0.95 in pH 10 buffer in the presence of oxygen (Figure 5.4B). Almost the same trend was observed in the quenching efficiency plots in the absence of oxygen in Figure 5.4A. This could be explained by the greater driving force at higher pH value for hole transfer from NRs to dopamine

catechol groups. The reduction potential of free dopamine was reported to be decreasing with increasing pH values²¹⁸ indicating the hole transfer from the NRs to dopamine molecules was favored at high pH values. 2) When the pH value is fixed, the quenching is more pronounced as oxygen is induced, resulting in higher quinone concentration. Regarding the same 10 μM concentration of the quencher, the quenching efficiency was only 0.2 in pH 9 buffer in the absence of oxygen (Figure 5.4A) but increased to 0.8 in the same pH values in the presence of oxygen (Figure 5.4B). This could be explained by higher quinone group concentration in the presence of oxygen at a fixed basic pH value. And also, dopamine absorbing at the NRs surface would result in a static quenching mechanism.

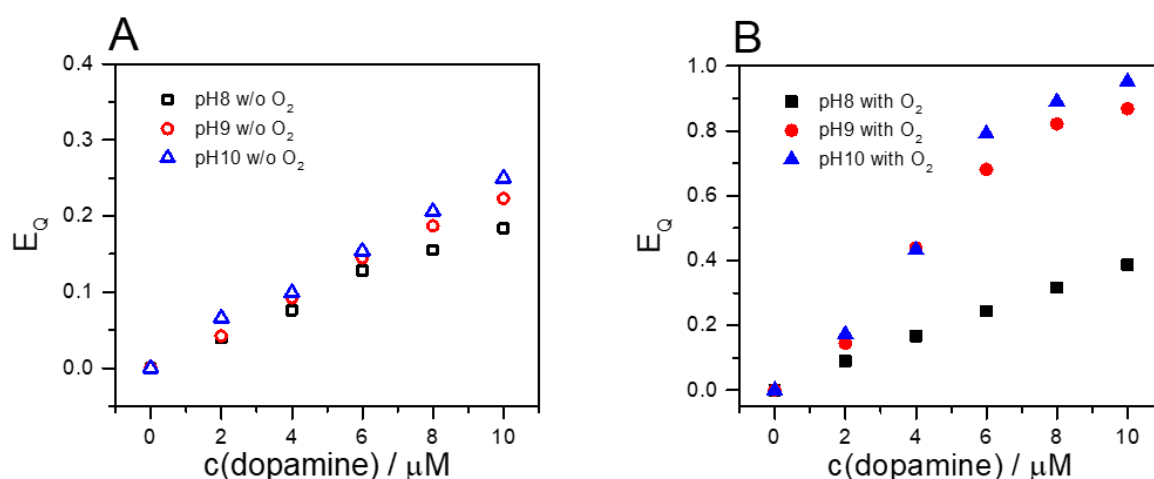


Figure 5.4. The quenching efficiency of MUA-NRs at different pH values in the presence (A) and absence (B) of oxygen.

To gain a deeper understanding of the data, the Stern-Volmer method was introduced here to interpret the data. The Stern-Volmer equation¹⁵⁶ is displayed below:

$$\frac{I_0}{I} = 1 + K_{SV}[Q] \quad (5.3)$$

where I_0 and I were the fluorescence intensities in the absence and presence of quencher, respectively; K_{SV} was the Stern-Volmer constant. $[Q]$ was the concentration of the quencher. If the quenching mechanism is only dynamic quenching, then K_{SV} could be replaced by K_d :

$$\frac{I_0}{I} = 1 + K_d[Q] \quad (5.4)$$

$$K_d = \tau_0 k_q \quad (5.5)$$

Where k_q is the bimolecular quenching constant; τ_0 is the lifetime of the emission in the absence of a quencher. If the quenching is only static, then the equation should be written as:

$$\frac{I_0}{I} = 1 + K_s[Q] \quad (5.6)$$

Where K_s represents the association constant for non-emitting complex formation. Equation 5.4 and 5.5 are both first-order in $[Q]$, which account for a linear relationship in plots. However, in many instances, the emission can be quenched both by collisions and by complex formation with the same quencher. Then the Stern-Volmer equation could be written as:

$$\frac{I_0}{I} = (1 + K_d[Q])(1 + K_s[Q]) \quad (5.7)$$

This modified form of the Stern-Volmer equation is second order in $[Q]$, which accounts for an upward curvature in plots when both static and dynamic quenching occurred for the same emitter.

In Figure 5.5, Stern-Volmer plots of emission quenching experiments were shown, and the difference between the two systems was obvious. After fitting, an upward curvature could be observed in the presence of oxygen in Figure 5.5A, indicating the quenching mechanism was a combined dynamic and static quenching, and a polynomial fitting could be nicely applied on it, while a linear fitting would nicely describe the plots in the absence of oxygen in Figure 5.5B. This indicates that the quenching mechanism here was either only dynamic or static quenching.

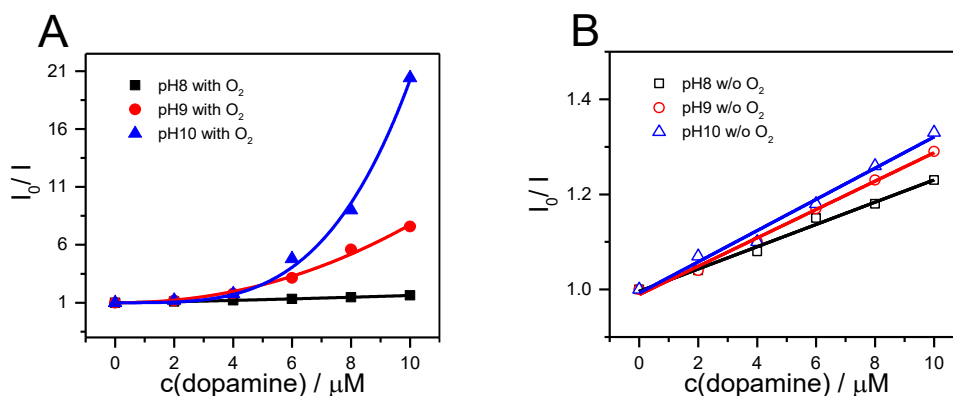


Figure 5.5. Stern-Volmer plots of MUA-NRs emission quenching at different pH values in the presence (A) and absence (B) of oxygen.

The Stern-Volmer plots in the presence and absence of oxygen in pH 8 buffer were displayed in Figure 5.6. And the two different behaviors referring to two different quenching mechanisms could be clearly seen. The upward curvature in the presence of oxygen could be fitted with a parabola function indicating the relationship with $[Q]$ in the second order. While in the absence of oxygen, the plots were linear fitted indicating the first-order relation with $[Q]$.

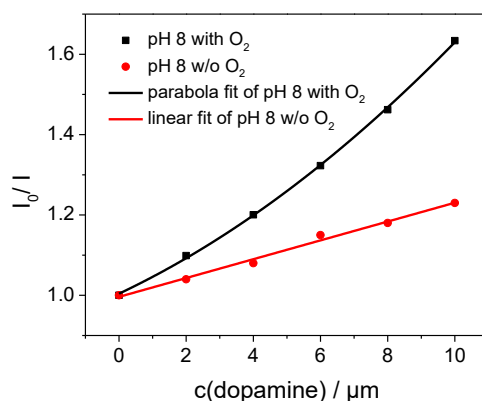


Figure 5.6. Stern-Volmer plots of MUA-NRs emission quenching in pH 8 PBS buffer in the presence and absence of oxygen with the associated fitting.

Further, to figure out the electron transfer quenching mechanism, we performed emission lifetime measurements. The Stern-Volmer method could be described as below for dynamic quenching:

$$\frac{\tau_0}{\tau} = \frac{I_0}{I} = 1 + K_d[Q] = 1 + \tau_0 k_q [Q] \quad (5.8)$$

And for static quenching:

$$\frac{\tau_0}{\tau} = 1 \quad (5.9)$$

where τ_0 and τ were the lifetime of the emission in the absence and presence of quencher, respectively. The measurement was carried out on one sample, which is the one in pH 9 buffer in the presence of oxygen. Plots were displayed in Figure 5.7, and fitting parameters were listed in Table 5.1. By fitting the emission lifetime plots, the results showed that there were two time components, one component was around 1.2 ns (this time component only appeared once dopamine was added, so data points started at dopamine concentration of 4 μM), and the other one was decreasing from 15.2 ns to 10.9 ns while the concentration of dopamine increased from 0 μM to 10 μM . Worth mentioning here, the IRF was not deconvoluted with software Decayfit here but determined as a 0.2 ns decay time component. In the meanwhile, all time components obtained from exponential fit were larger than 0.2 ns, so the time components in this chapter could be trusted.

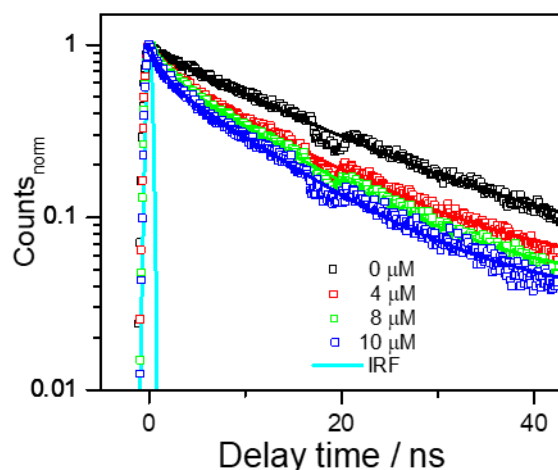


Figure 5.7. The emission lifetime plots of MUA-NRs in pH 9 buffer in the presence of oxygen with different concentrations of dopamine. All data were normalized to 1 at the signal maximum. The excitation wavelength was 400 nm.

Table 5.1. Time components of emission lifetime obtained with mono- or bi-exponential fit. The emission lifetime of MUA-NRs without dopamine (0 μM) was fitted by mono-exponential fit. The emission lifetimes of MUA-NRs with dopamine added (4 μM , 8 μM , 10 μM) were fitted by bi-exponential fit.

c(dopamine) / μM	τ_1 / ns	τ_2 / ns
0	—	15.2 ± 0.2
4	1.2 ± 0.1	12.3 ± 0.2
8	1.2 ± 0.1	11.3 ± 0.2
10	1.3 ± 0.1	10.9 ± 0.2

When we plotted the decreasing time component in a Stern-Volmer plot (Figure 5.8), it could be nicely described by a linear fitting, which meant this decreasing time component was a prove of dynamic quenching and the 1.2 ns time component was a strong indication of static quenching. This conclusion fitted the statement we addressed from the emission intensity Stern-Volmer plots that the quenching mechanism of our system was a combination of dynamic and static quenching in the presence of oxygen. The static quenching could be introduced by the static adsorption process of dopamine on the NRs,²³⁷ forming the shorter emission lifetime, which was not concentration-dependent, and the dynamic quenching could be introduced by electron transfer from MUA-NRs to the free quinone group with a concentration-dependent emission lifetime.

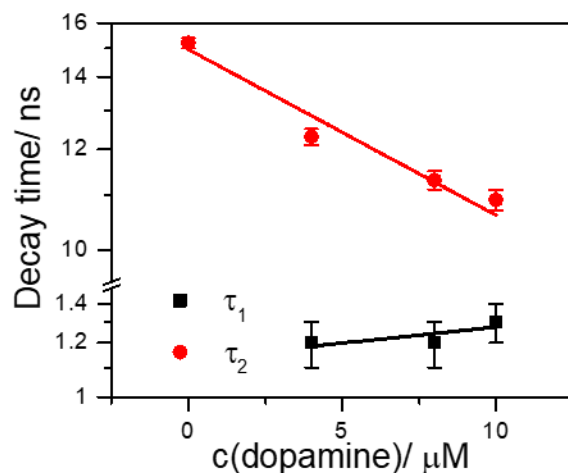


Figure 5.8. Stern-Volmer plots of time components with different concentrations of the quencher in pH 9 buffer in the presence of oxygen.

5.2 The interaction between MUA-NRs with polydopamine

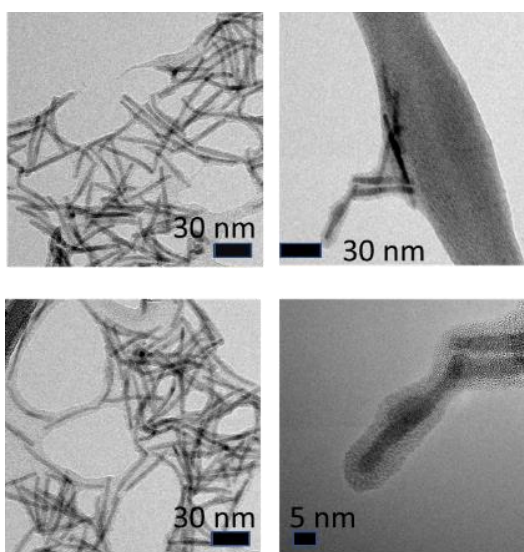


Figure 5.9. TEM image of P-MUA-NRs at different sample positions. The scale bars were inserted in each TEM image (provided by *Weil* group and displayed here with their permission).

With knowing the electron transfer mechanism of MUA-NRs with dopamine molecules, we would like to investigate further to the electron transfer mechanism of MUA-NRs with polydopamine. In cooperation with Prof. *Tanja Weil*, Max-Planck-Institute for Polymer Research, Mainz, a batch of MUA-NRs coated with polydopamine (P-MUA-NRs) was synthesized by mixing MUA-NRs and dopamine hydrochloride in pH 8.5 PBS buffer for 20 min at 55 °C with sonication. The MUA-NRs were determined to be with 50 nm in length and 5 nm in diameter, as mentioned above. And the thickness of the polydopamine shell was determined to be around 5 nm, as showed in Figure 5.9.

By comparing the steady-state absorption and emission spectra in Figure 5.10, the basic shape and feature of MUA-NRs remained in the absorption spectrum of P-MUA-NRs like the should at around 485 nm referring to the first excitonic absorption peak of CdS and two shoulders in the higher energy range referring to the higher levels in CdS. The P-MUA-NRs had a background compared to MUA-NRs in the displayed wavelength range due to the absorption of polydopamine. The emission spectrum of P-MUA-NRs showed one expected peak centered at 570 nm referred to the emission from the coated NRs, which was the same in position as the MUA-NRs also centered at 570 nm. An artifact with a star at 532 nm referred to the Raman band of water due to low emission intensity of the samples. By exciting at 450 nm, the emission intensity of P-MUA-NRs was extremely low compared to the emission intensity of MUA-NRs.

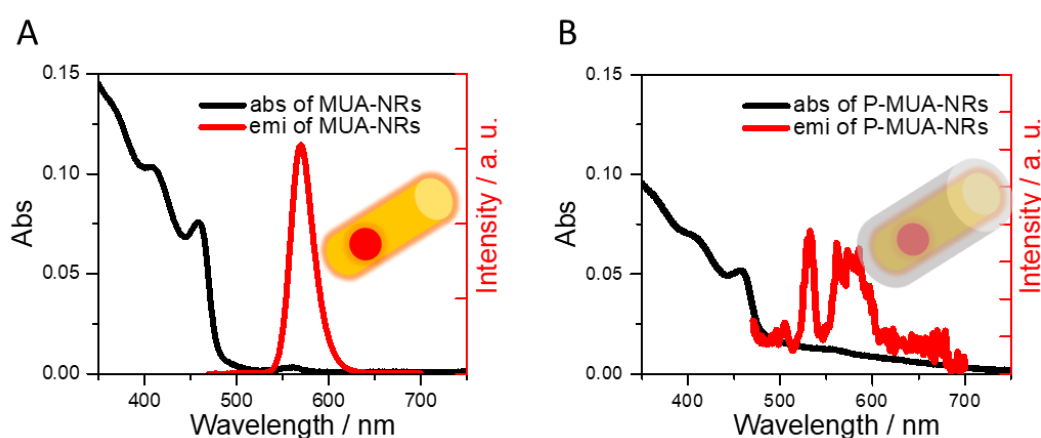


Figure 5.10. Absorption and emission spectra of (A) MUA-NRs and (B) P-MUA-NRs in water. The rod figures in the respective plots were the illustration of MUA-NRs and P-MUA-NRs. The excitation wavelength was 450 nm.

Relative PLQY measurement was carried out for the quantitative comparison between MUA-NRs and P-MUA-NRs in different pH buffer using MUA-NRs as the standard since the absolute PLQY of MUA-NRs was measured as 0.30 with excitation of 450 nm, and the emission spectral shape of the MUA-NRs and the P-MUA-NRs were comparable. The relative PLQY was calculated with Equation 2.6 in chapter 2. Only the emission contributed by the NRs was considered, which means the Raman band of water was not taken into the calculation of the PLQY. The absorbance was corrected by a background of polydopamine. The background was determined by extracting the absorption spectrum of MUA-NRs multiplied by a factor from the absorption spectrum of P-MUA-NRs to get a baseline as smooth as possible. The relative PLQY results were displayed in Figure 5.11. The relative PLQY of P-MUA-NRs showed the highest in pH 5 and lowest in pH 11 with a trend of decreasing as the pH increased. This could be explained by the same electron transfer mechanism mentioned above. As the pH increased, the driving force of the electron transfer from NRs to the polydopamine shell increased, could result in a lower PLQY. (Worth mentioning here, although the measurements were performed with caution, the

relative PLQY of P-MUA-NRs was so low, and the error introduced by this method was $\sim 10\%$ ²³⁸, which meant that the results here were only for a basic guide to related experiment but not for a solid statement.)

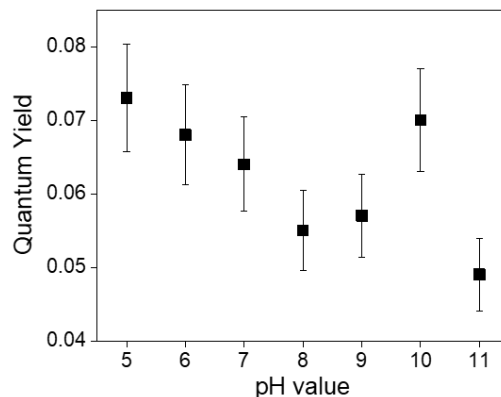


Figure 5.11. Relative PLQY of P-MUA-NRs in different pH buffers. The relative PLQY of pH 10 could be a bad point or artifact due to very low emission intensity of the sample.

However, alone from PL results, it was still unknown if the quenching was due to the electron transfer from the NRs to the polydopamine shell or the hole transfer. After steady-state data discussion, the TA measurement of P-MUA-NRs was carried out with MUA-NRs as the reference. The TA spectra were showed in Figure 5.12, with an excitation wavelength of 390 nm. There were two bleaching signals in both spectra at 460 nm and 560 nm, referring to the CdS and CdSe, respectively. The decay of CdS and CdSe in MUA-NRs was slow at first and fast in late time. The signal did not decay to 0 at the end of the measurement, which was 1700 ps. However, the decay of CdS and CdSe were already fast at first and decayed to 0 at the end of the measurements.

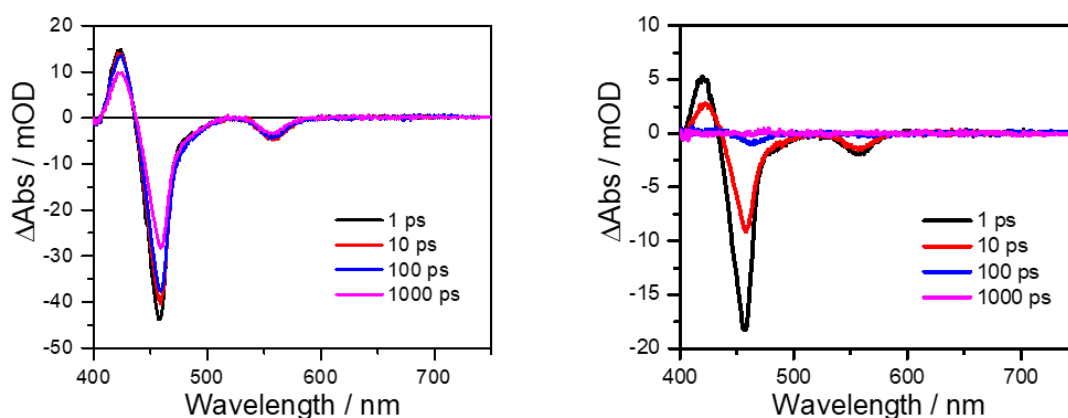


Figure 5.12. The TA spectrum of (A) MUA-NRs and (B) P-MUA-NRs at different delay times in water. The excitation wavelength was 390 nm.

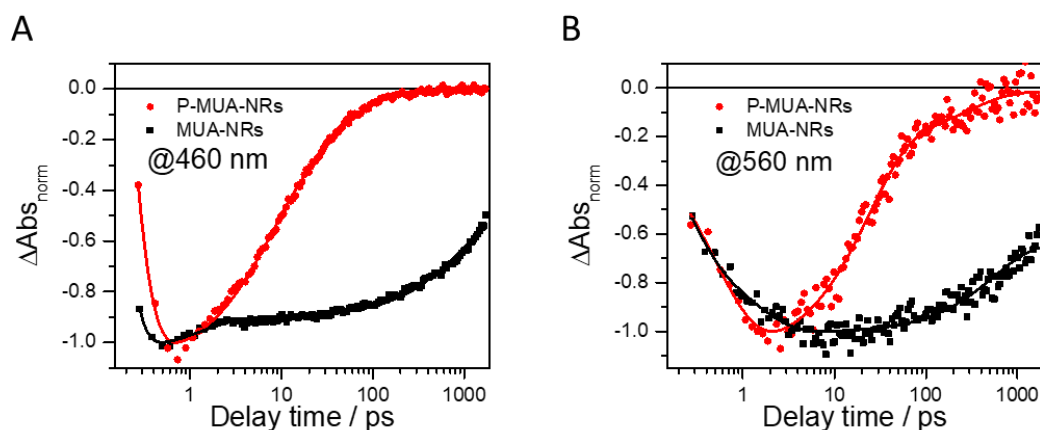


Figure 5.13. The kinetics of P-MUA-NRs and MUA-NRs at 460 nm (CdS) and 560 nm (CdSe). The kinetics were normalized to -1 at the minimum of the fitting curve.

The decay would be more clearly demonstrated when the kinetic at 460 nm (CdS) and 560 nm (CdSe) were plotted and fitted. Related fitting parameters were displayed in Table 5.2. As shown in Figure 5.13, in MUA-NRs and P-MUA-NRs, the decay kinetics of CdS could be fitted with three decay components. (This was single kinetic fit, so delivered information might be different compared to global fit in chapter 4) The first time component, as mentioned many times in this thesis in the signal formation (τ_1), was referring to the cooling of hot electron at ~ 0.1 ps. The first decay time components (τ_1) of CdS in both MUA-NRs and P-MUA-NRs were in the range of 1 – 6 ps, referring to the electron depopulation on the CdS conduction band. In MUA-NRs, this was due to the hole localization driven electron localization from the CB of CdS to the CB of CdSe because the (τ_2) in CdSe part in MUA-NRs was with positive amplitudes indicating population on the CB of CdSe due to the process of hole localization. In P-MUA-NRs, the (τ_1) in CdSe part was not with a positive amplitude but a negative amplitude indicating the electron was not localized on the CB of CdSe, so the (τ_1) in CdS decay of P-MUA-NRs could be assigned with electron movement to the matrix. The second decay time component (τ_2) was fast in P-MUA-NRs ~ 41 ps and relatively slow in MUA-NRs ~ 900 ps. In MUA-NRs, this time component was assigned with the exciton recombination process, but in P-MUA-NRs, this time component should be assigned with electron transfer to polydopamine due to the rate of this decay. A similar assignment also explained the decay kinetics at 560 nm (CdSe). The first time component in signal formation referred to cooling. The time component (τ_2) in MUA-NRs was a signal formation process, with a positive amplitude, and referred to the hole localization process corresponding to the first decay time components (τ_1) in CdS in MUA-NRs as introduced in the previous chapter. The time component (τ_1) in P-MUA-NRs was indeed a decay signal, which meant the electron movement to CB was not happening, probably due to the electron transfer to the polydopamine. The second decay component in MUA-NRs referred to the recombination process, but in P-MUA-NRs, it referred to the electron transfer to the polydopamine, and this could be further confirmed by comparing the decay time (τ_2) in both CdS

and CdSe. The decay time (τ_2) was faster ~ 40 ps in the shell than in the core ~ 300 ps, because the shell was closer to the polydopamine.

Table 5.2 Detailed fitting parameters in 460 nm (CdS) and 560 nm (CdSe) kinetics. R^2 referred to the Adj. R-Square and y_0 referred to the offset at the end of the fitting.

Samples	R^2	y_0	τ_{f1}	A_f	τ_{f2}	A_{f2}	τ_1	A_1	τ_2	A_2
P-MUA-NRs 460 nm	0.998	-0.01 ± 0.00	0.1 ± 0.0	9.6 ± 1.7	–	–	6.4 ± 0.3	-0.62 ± 0.02	41 ± 2	-0.45 ± 0.02
MUA-NRs 460 nm	0.985	-0.49 ± 0.01	0.1 ± 0.0	14.9 ± 23.3	–	–	1.3 ± 0.2	-0.15 ± 0.02	915 ± 60	-0.42 ± 0.01
P-MUA-NRs 560 nm	0.980	-0.02 ± 0.02	0.5 ± 0.1	0.93 ± 0.12	–	–	23.5 ± 1.9	-0.87 ± 0.03	300 ± 103	-0.20 ± 0.03
MUA-NRs 560 nm	0.891	-0.64 ± 0.02	0.2 ± 0.2	0.79 ± 0.67	1.3 ± 0.4	0.35 ± 0.14	–	–	545 ± 73	-0.36 ± 0.02

5.3 The interaction between HS-PEG-OCH₃-NRs with dopamine molecules

Above mentioned, after ligand exchange with MUA, the colloidal stability of NRs in acidic buffer faced problems due to charged $-\text{COO}^-$ group. The protonation of the carboxylate groups in the acidic buffer will result in a decrease of electrostatic repulsion between nanoparticles, eventually leading to nanoparticle aggregation.⁷⁸ So, a new surface ligand was desired, ending with a neutral end group while containing a long hydrophilic polyethylene glycol (PEG) chain acting as the hydrophilic part and a thiol group acting as the anchoring group. As mentioned in the previous chapter, HS-PEG-OCH₃ was chosen because of its $-\text{OCH}_3$ neutral end group and a PEG chain with a repeat unit of roughly 18. The ligand exchange protocol and its properties on steady-state, time-resolved measurements, and pH stability were also introduced in the previous chapter. In this chapter, we shall only focus on the quenching experiment itself. Since the NRs capped with HS-PEG-OCH₃ were able to be dispersed in PBS lower than pH 8, we chose pH 5, pH 7, and pH 9 as the target pH values to investigate the quenching experiments. Worth mentioning here, the HS-PEG-OCH₃-NRs was not exchanged on the same batch of NRs as the above mentioned MUA-NRs. The main difference between these two batches of NRs was the dimension of the NRs. When the quenching experiments were performed with HS-PEG-OCH₃-NRs, the absorbance of each sample was adjusted comparably to the above mentioned MUA-NRs. However, due to differences in size, the ratio of quencher to emitter was changed dramatically in this section. The

quencher to emitter ratio was 0.03, 0.06, 0.09, 0.11, 0.14 with 2 μM , 4 μM , 6 μM , 8 μM and 10 μM dopamine added, respectively.

As shown in Figure 5.14, the quenching experiments were carried out in pH 5, pH 7 and pH 9 PBS buffer (concentration 50 mM) both in the presence and absence of oxygen to investigate the influence of pH values and oxygen on quenching experiments. After recording the initial emission intensity of rods, different amounts of dopamine were added into the same cell, which holds the rods solution. After adding 1 μM dopamine each time, the absorption and emission spectrum was recorded. For each plot in Figure 5.14, the emission intensity was decreasing as the concentration of dopamine increased. But unlike what happened to MUA-NRs, the HS-PEG-OCH₃-NRs in pH 7 showed the smallest intensity changes in three different values both in the absence and presence of oxygen. And the largest intensity change appeared in pH 9 in the absence of oxygen, which is quite a surprise that the intensity change when the oxygen is present is even smaller compared to in the absence of oxygen in pH 7 and pH 9. This result is very different from what we had with MUA-NRs. To find the appropriate explanation, quenching efficiency and the Stern-Volmer method was performed.

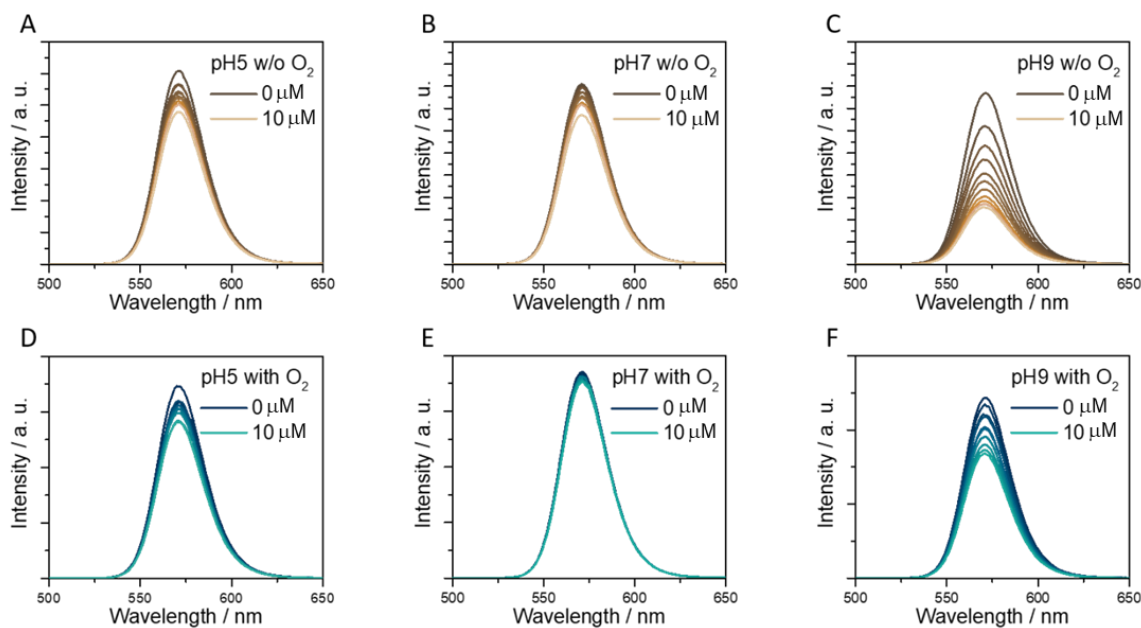


Figure 5.14. The emission spectra of HS-PEG-OCH₃-NRs in different pH value buffer in the absence and presence of oxygen with different amounts of dopamine added. (A) pH 5 without O₂, (B) pH 7 without O₂, (C) pH 9 without O₂, (D) pH 5 with O₂, (E) pH 7 with O₂, and (F) pH 9 with O₂.

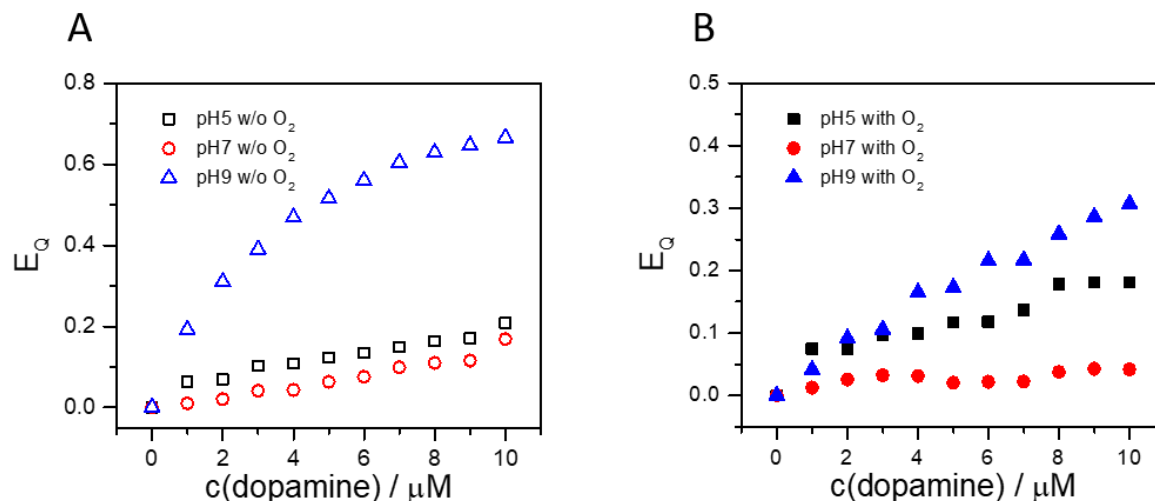


Figure 5.15. The quenching efficiency of HS-PEG-OCH₃-NRs in different pH values in the presence (A) and absence (B) of oxygen.

The quenching efficiency in different pH values, both in the presence and absence of oxygen, were shown in Figure 5.15. The quenching efficiency E_Q was determined by Equation (5.1). At a given dopamine concentration, for example, 10 μM , the quenching efficiency of HS-PEG-OCH₃-NRs exhibited the lowest value ($E_Q = 0.17$) in pH 7 buffer in the absence of oxygen, while the highest quenching efficiency ($E_Q = 0.67$) appeared in pH 9 and the intermediate quenching efficiency ($E_Q = 0.21$) showed in pH 5. The same trend was also exhibited in the presence of oxygen, lowest value ($E_Q = 0.04$) in pH 7 buffer, while the highest quenching efficiency ($E_Q = 0.31$) appeared in pH 9 and the intermediate quenching efficiency ($E_Q = 0.18$) showed in pH 5. The quenching efficiency could be interpreted by the classification of pH values. To interpret the data in a way that depended on oxygen, at a given dopamine concentration of 10 μM in pH 5 buffer, the quenching efficiency in the absence ($E_Q = 0.21$) and presence ($E_Q = 0.18$) of oxygen were nearly identical. This meant that oxygen had a minor influence in pH 5 buffer. For pH 7, the quenching efficiency in the absence of oxygen ($E_Q = 0.17$) was higher than that in the presence of oxygen ($E_Q = 0.04$). The same trend could also be found in pH 9. The quenching efficiency in the absence of oxygen ($E_Q = 0.67$) is much higher than that in the presence of oxygen ($E_Q = 0.31$). To make a short conclusion, at a given dopamine concentration, $E_{Q \text{ pH}9} > E_{Q \text{ pH}5} > E_{Q \text{ pH}7}$ both for in the absence and presence of oxygen. At the same time, in pH 5 and pH 7 buffer, $E_{Q \text{ w/o oxygen}} \approx E_{Q \text{ with oxygen}}$, while in pH 9, $E_{Q \text{ w/o oxygen}} > E_{Q \text{ with oxygen}}$.

But the electron transfer quenching mechanism could not explain the quenching between HS-PEG-OCH₃-NRs and dopamine because the quenching in pH 9 without oxygen was even more pronounced than that in the pH 9 in the presence of oxygen. However, this could be explained by the hole transfer mechanism. The driving force of hole transfer was increased with increased pH values.²¹⁸ When in pH 9 buffer, the driving force was stronger than in pH 5 and pH 7, resulting in stronger quenching no matter

it was in the absence or presence of oxygen. The quenching was less pronounced in pH 9 in the presence of oxygen compared to in the absence of oxygen. This could be explained by the decreasing amount of catechol group due to the oxidation of dopamine. The higher quenching efficiency of pH 5 compared to that in pH 7 might be explained by the competing process between the driving force and oxidation of dopamine, and this was further confirmed by the higher quenching efficiency of pH 7 in the absence of oxygen compared to that in the presence of oxygen. This argument was summaries in Figure 5.16.

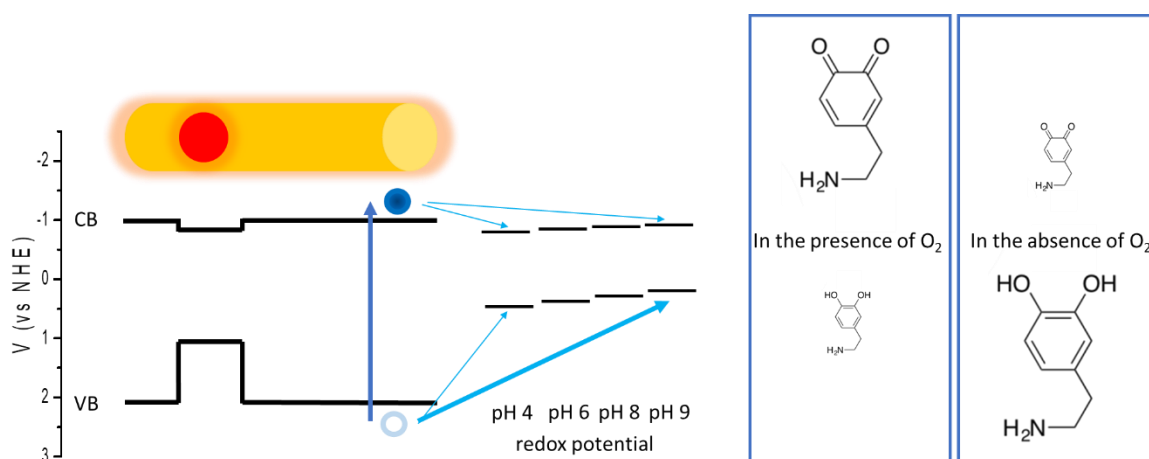


Figure 5.16. The illustration of the influence of pH and oxygen in the quenching experiment between HS-PEG-OCH₃-NRs and dopamine. The quenching efficiency was influenced by two key parameters, namely the driving force (ΔG , based on the energy difference between the VB of the HS-PEG-OCH₃-NRs and the redox potential of free dopamine or the CB of the HS-PEG-OCH₃-NRs and the redox potential of dopamine quinone)²¹⁸ and the concentration of the catechol groups. In the absence of oxygen, the increasing of pH values had positive influences on the driving force of the hole transfer from HS-PEG-OCH₃-NRs to dopamine catechol groups but not so pronounced positive influences on the driving force of the electron transfer from HS-PEG-OCH₃-NRs to the dopamine quinone groups since the driving force is so small between the CB of the HS-PEG-OCH₃-NRs and the redox potential of the dopamine quinone groups. In the meanwhile, the presence of oxygen showed negative influences on the concentration of the catechol groups (negative meant disfavoring the hole transfer from HS-PEG-OCH₃-NRs to the catechol groups here). However, the electron transfer was favored from MUA-NRs to quinone groups in the presence of oxygen at pH 9 but disfavored for HS-PEG-OCH₃-NRs. This could be explained by more electron trap states on the latter NRs which competed with the electron transfer from NRs to quinone groups. This system, HS-PEG-OCH₃-NRs and dopamine showed very complicated competing processes and the observation of the quenching experiments between HS-PEG-OCH₃-NRs and dopamine were results of these complicated competing processes.

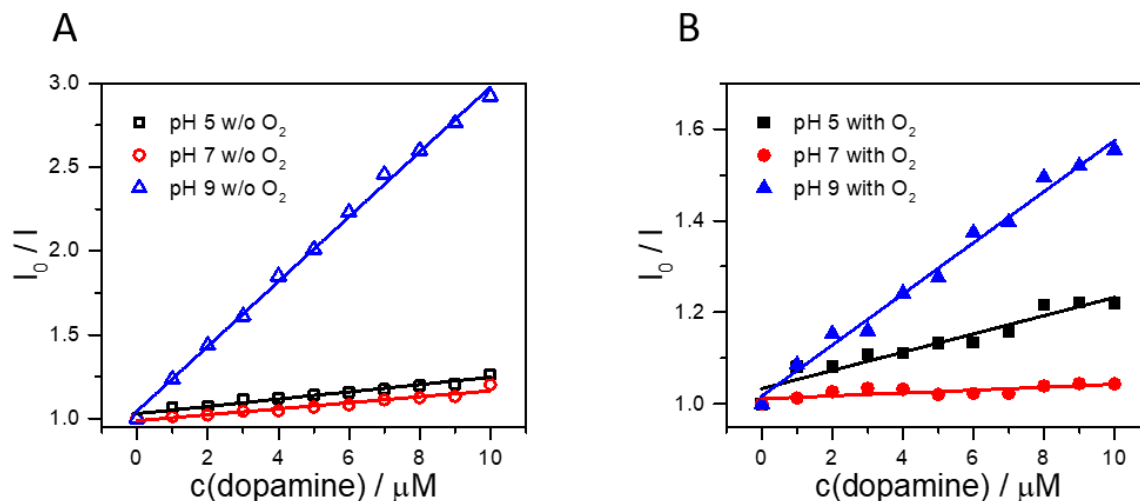


Figure 5.17. Stern-Volmer plots of HS-PEG-OCH₃-NRs emission quenching in different pH values in the presence (A) and absence (B) of oxygen.

The Stern-Volmer method was introduced here to interpret the data further using equation (5.2) – (5.8), in Figure 5.17. The feature of the first order in [Q] could be seen in these Stern-Volmer plots indicating that the quenching mechanism was either dynamic quenching or static quenching in this case. Even though dopamine was already oxidized in pH 9 in the presence of oxygen, the electron transfer would not occur. With the information obtained in the quenching efficiency and quenching of MUA-NRs above, the dynamic quenching of hole transfer would be a reasonable explanation here as shown in Figure 5.18.

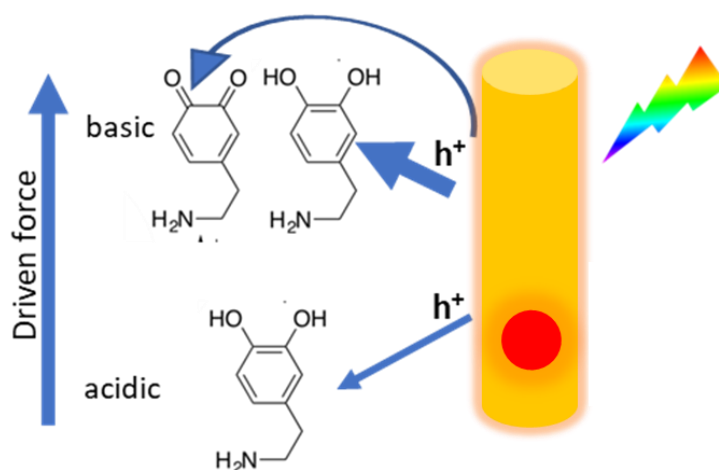


Figure 5.18. The illustration of hole transfer mechanism between HS-PEG-OCH₃-NRs and dopamine. The driving force of hole transfer was increasing with the increased pH values. The hole transfer would be suppressed in the presence of oxygen due to oxidation of dopamine resulting in less concentration of the catechol groups.

The main difference between MUA-NRs and HS-PEG-OCH₃-NRs was that HS-PEG-OCH₃-NRs had surface ligand containing PEG chain and had more pronounced electron traps due to the larger volume of PEG chain resulting in less coverage rate. The electron trap state on the surface of the HS-PEG-OCH₃-NRs was more pronounced than that on the surface of MUA-NRs. This would further explain the quenching efficiency difference between the MUA-NRs and HS-PEG-OCH₃-NRs at pH 9 in the absence of oxygen, because the trapping of electron favored the hole transfer process.

5.4 Conclusion

In this chapter, the interactions between NRs and dopamine were investigated. For MUA-NRs, the quenching mechanism was dynamic quenching in the absence of oxygen due to the electron transfer from the CB of NRs to the quinone groups. The quenching mechanism changed to combined dynamic and static quenching when oxygen was in the presence. The polymerized polydopamine could be coated or form small clusters attached to the MUA-NRs, resulting in a coated nanoparticle with a short emission lifetime that was not concentration-dependent. While the free dopamine still acted as the quencher in the dynamic quenching mechanism as the emission lifetime referring to this process was concentration dependent. For P-MUA-NRs, TEM and steady-state absorption and emission measurements proved that the coating of dopamine was successful. And relative PLQY showed a trend of decreasing while the pH increased. But the relative PLQY was too low and the errors introduced by this relative PLQY calculation were too large, so more absolute PLQY measurements need to be done. TA measurements were taken to probe the fast electron transfer from both the CdS and CdSe to the polydopamine, while the electron transfer of CdS was much faster than that in the CdSe due to distance. For HS-PEG-OCH₃-NRs, the quenching mechanism could be explained by hole transfer quenching mechanism from NRs to the catechol group, which could be further explained by the different surface states of different ligands. The complicated quenching efficiency results could be explained by competing processes between pH values and oxygen. Time-resolved measurements were not able to be performed on HS-PEG-OCH₃-NRs due to limited time at the end of my Ph.D. project, which was a pity at the end of my thesis. But the outlook of possibilities on easier hole removal of the dot-in-rod NRs was already at the dawn.

CHAPTER 6.**Summary**

The design and investigation on nanocrystals were never paused in the last few decades, so new researchers, like me, could do their researches standing on the shoulders of giants. The more we discovered, the more we found that need to be discovered. And this is probably the driving force of science ($\Delta G_{sci} < 0$).

The main focus of this thesis was the preparation of using NRs as photosensitizers, and divided into three chapters, where the structure of CdSe/CdS NRs, the phase transfer of CdSe/CdS dot-in-rod NRs and the interactions between dot-in-rod NRs and dopamine / polydopamine were discussed from chapter 3 to chapter 5.

In chapter 3, CdSe/CdS dot-in-rod and inside-out NRs were studied. The properties of the dot-in-rod NRs were used as references to compare the properties of the inside-out NRs. By comparing the steady-state absorption spectra, the dot-in-rod NRs showed a well-confined structure while a large size distribution of CdSe part was confirmed in the inside-out NRs. By comparing the steady-state emission spectra, the inside-out NRs exhibited the intrinsic emission together with two surface states emission, namely the shallow state related emission (sharp) and deep hole trap emission (broad), while the dot-in-rod NRs also exhibited these three emission peaks. But the intrinsic emission of the dot-in-rod NRs were sharper than that in the inside-out NRs. The shallow state related emission of the dot-in-rod NRs was slightly sharper than the inside-out NRs and the deep hole trap related emission of the dot-in-rod NRs was much less pronounced than that in the inside-out NRs indicating less surface states in the dot-in-rod NRs due to the surface passivation of CdS shell on the CdSe core. Notably, the intrinsic emission of the inside-out NRs was much broader than that in the dot-in-rod NRs, further confirmed the large size distribution of the CdSe part in this structure. Depending on the extent of the surface disorder, the surface state could be near the conduction band as a “shallow” state or far away from the conduction band as a “deep” trap. The shallow and deep traps were further confirmed by transient absorption spectroscopy. In the dot-in-rod NRs, with a quasi-Type II band alignment, the hole localization could be probed by the second time component in the same time range with opposite amplitudes in the kinetics of the CdS bleach and CdSe bleach. In the inside-out NRs, there was no spectral evidence of hole localization driven electron localization on the shell, but the hole localization could still be possible. The second time component in the kinetic of CdS bleach in picosecond range was assigned to the fast trapping by shallow traps while the second time component in the kinetic of CdSe bleach in picosecond range was just missing due to competing processes between electron population on the CB due to energy offset and electron depopulation due to surface traps. The residual at the end of each kinetic was further

evidence of these surface trap states. The inside-out NRs left us much more to be desired. The band alignment, the surface defect passivation, and the control over its shape needed to be investigated more. And since the surface trap states could be related to the PL, a systemic investigation of PL of degrading should also be performed to probe the influence of degrading on the electronic structure of the inside-out NRs.

In chapter 4, CdSe/CdS dot-in-rod NRs with different ligands were investigated. The steady-state absorption measurements and the multi-Gaussian fit probed the ground state electronic structures of NRs, PEI seemed to etch the CdS surface or change the energetic band structures of the NRs, which was further proved by the steady-state emission measurements. The steady-state emission measurements and the multi-Gaussian fit also revealed the radiative recombination processes in the NRs where TOPO-, MUA-, HS-PEG-OCH₃-, DHLA-NRs were not influenced much by the surface ligands, but PEI gave evidence of surface defects removal and DHLA-PEG resulted in much more pronounced deep surface defects. This was further investigated with time-resolved emission spectroscopy. More pieces of evidence of surface defects were showed because the TOPO-, MUA-, and PEI-NRs showed comparable emission lifetime but exhibited very different absolute PLQY due to a better surface passivation of PEI, an intermediate surface passivation of TOPO but least on MUA-NRs. Transient absorption measurements gave more information on the non-radiative processes. Even the radiative recombination was so different in NRs with different ligands, and the non-radiative recombination seems to follow the same rule. All NRs exhibited comparable decay processed only with different decay time components with different amplitudes after data analysis revealing the influence of surface states. The pH stability test was also carried out to give information in practical applications. The MUA- and PEI-NRs showed great potential in basic pH values, while for applications in the acidic or wide pH range, HS-PEG-OCH₃-NRs was a much better choice in terms of pH stability.

In chapter 5, the interactions between NRs and dopamine and polydopamine were investigated. For MUA-NRs and HS-PEG-OCH₃-NRs, the quenching mechanism was dynamic quenching in the absence of oxygen due to the electron and hole transfer, respectively. The quenching mechanism changed to combined dynamic and static quenching when oxygen was in the presence for MUA-NRs. But for HS-PEG-OCH₃-NRs, the quenching mechanism was still dynamic quenching because of the hole transfer mechanism due to less HS-PEG-OCH₃ ligands coverage resulting in more electron traps compared to MUA-NRs. For P-MUA-NRs, TEM and steady-state absorption and emission measurements proved that the coating of dopamine was successful. Fast electron transfer from both the CdS and CdSe to the polydopamine was observed in the TA spectroscopy, while the electron transfer of CdS was much faster than that in the CdSe because the CdS shell was much closer to the polydopamine shell. And the feature in both kinetics assigned with hole localization was missing in P-MUA-NRs, indicating the polydopamine dominated the competing process of accepting the electron. Time-resolved measurements were still needed for the HS-PEG-OCH₃-NRs and dopamine / polydopamine to give

solid proofs of the quenching mechanism in the future. The results in the chapter left us a lot of potential applications with the electron and hole transfer quenching mechanism, like sensing, photocatalysis, and hole remover.

This thesis presented a quiet full picture in terms of hole removal and phase transfer of NRs. Based on the results of chapter 3, the inside-out NRs was very promising on the hole localization at the CdSe shell when the surface defects could be passivated. And this could be further achieved by surface passivation of PEI, based on the results from chapter 4. The surface passivation of PEI would probably make the inside-out NRs not only fewer surface defects but also water soluble, which would further favor the application as photosensitizers. The surface passivation of different ligands would also result in different quenching mechanism when the CdSe/CdS dot-in-rod NRs were interacting with dopamine. The quenching experiments of MUA-NRs and dopamine could be explained by electron transfer from the NRs to the dopamine molecules and for HS-PEG-OCH₃-NRs could be explained by the hole transfer from the NRs to the dopamine molecules due to more electron traps on the surface of the latter NRs. This was a strong indication that the electron or hole transfer quenching mechanism could be tuned by the surface states of the NRs which could further tuned by the surface ligands. Together with the inside-out NRs and different surface ligands, the aim of easy hole removal after exciton generation would be possible. And according to the TA results of the P-MUA-NRs, the on and off of electron transfer could also be tuned by adjusting the pH values, which would further introduce various possibilities of applications.

In short, the presented results in this thesis on NRs revealed the properties of the NRs from the inside out, from structural to surficial, end up with interaction with other molecules. I know I am not a giant in science, but I still wish my work would inspire other researchers on the way to their achievements.

CHAPTER 7.

Zusammenfassung

Das Design und die Untersuchung von Nanokristallen wurden in den letzten Jahrzehnten nie unterbrochen, sodass neue Forscher wie ich ihre Forschungen auf den Schultern von Riesen durchführen konnten. Je mehr wir entdeckten, desto mehr mussten wir entdecken. Und das ist wahrscheinlich die treibende Kraft der Wissenschaft ($\Delta G_{sci} < 0$).

Das Hauptaugenmerk dieser Arbeit lag auf der Herstellung von NRs als Photosensibilisatoren und war in drei Kapitel unterteilt, in denen die Struktur von CdSe/CdS-NRs, der Phasentransfer von CdSe/CdS dot-in-rod-NRs und die Wechselwirkungen zwischen dot-in-rod NRs und Dopamin / Polydopamin wurden beschrieben von Kapitel 3 bis Kapitel 5 diskutiert.

In Kapitel 3 wurden CdSe/CdS dot-in-rod und inside-out NRs untersucht. Die Eigenschaften der dot-in-rod NRs wurden als Referenz verwendet, um die Eigenschaften der inside-out NRs zu vergleichen. Durch Vergleich der stationären Absorptionsspektren zeigten die dot-in-rod NRs eine gut begrenzte Struktur, während eine große Größenverteilung des CdSe-Teils in den inside-out NRs bestätigt wurde. Durch Vergleichen der stationären Emissionsspektren zeigten die inside-out NRs die intrinsische Emission zusammen mit zwei Oberflächenzustandsemissionen, nämlich der Emission im flachen Zustand (scharf) und der Emission von tiefen Lochfallen (breit), während der dot-in-rod NRs zeigten auch diese drei Emissionspeaks. Die intrinsische Emission der dot-in-rod NRs war jedoch formschöner als die der inside-out NRs. Die flache zustandsbezogene Emission der dot-in-rod NRs war etwas schärfer als die Inside-Out-NRs, und die Emission der dot-in-rod NRs in Bezug auf tiefe Lochfallen war viel weniger ausgeprägt als die in den Inside-Out-NRs weniger Oberflächenzustände in den dot-in-rod NRs aufgrund der Oberflächenpassivierung der CdS-Schale auf dem CdSe-Kern. Bemerkenswerterweise war die intrinsische Emission der inside-out NRs viel breiter als die der dot-in-rod NRs, was die große Größenverteilung des CdSe-Teils in dieser Struktur weiter bestätigte. Abhängig vom Ausmaß der Oberflächenstörung kann der Oberflächenzustand als "flacher" Zustand in der Nähe des Leitungsbandes oder als "tiefe" Falle weit vom Leitungsband entfernt sein. Die flachen und tiefen Fallen wurden durch transiente Absorptionsspektroskopie weiter bestätigt. In den dot-in-rod NRs mit einer Quasi-Type-II Bandenausrichtung konnte die Lochlokalisierung durch die zweite Zeitkomponente im gleichen Zeitbereich mit entgegengesetzten Amplituden in der Kinetik des CdS-Bleichmittels und des CdSe-Bleichmittels untersucht werden. In den inside-out NRs gab es keine spektralen Hinweise auf eine Lochlokalisierung auf der Schale, aber die Lochlokalisierung konnte immer noch möglich sein. Die zweite Zeitkomponente in der Kinetik des CdS-Bleichmittels im Pikosekundenbereich wurde dem schnellen Einfangen durch flache Fallen zugeordnet, während die zweite Zeitkomponente in der Kinetik

des CdSe-Bleichmittels im Pikosekundenbereich aufgrund konkurrierender Prozesse zwischen der Elektronenpopulation im CB nur fehlte zu Energieversatz und Elektronendepopulation aufgrund von Oberflächenfallen. Der Rest am Ende jeder Kinetik war ein weiterer Beweis für diese Oberflächenfallenzustände. Die Inside-Out-NRs ließen uns viel mehr zu wünschen übrig. Die Bandausrichtung, die Passivierung von Oberflächendefekten und die Kontrolle über ihre Form mussten genauer untersucht werden. Und da die Oberflächenfallenzustände mit dem PL zusammenhängen könnten, sollte auch eine systemische Untersuchung des PL des Abbaus durchgeführt werden, um den Einfluss des Abbaus auf die elektronische Struktur der inside-out NRs zu untersuchen.

In Kapitel 4 wurden CdSe/CdS dot-in-rod NRs mit verschiedenen Liganden untersucht. Die stationären Absorptionmessungen und die Multi-Gauß-Anpassung untersuchten die elektronischen Grundzustandsstrukturen von NRs. PEI schien die CdS-Oberfläche zu ätzen oder die energetischen Bandstrukturen der NRs zu verändern, was durch die stationären Emissionsmessungen weiter bewiesen wurde. Die stationären Emissionsmessungen und die Multi-Gauß-Anpassung zeigten auch die Strahlungsrekombinationsprozesse in den NRs, bei denen TOPO-, MUA-, HS-PEG-OCH₃-, DHLA-NRs nicht stark von den Oberflächenliganden beeinflusst wurden, aber PEI ergab Hinweise auf die Entfernung von Oberflächendefekten und DHLA-PEG führten zu viel ausgeprägteren tiefen Oberflächendefekten. Dies wurde mit zeitaufgelöster Emissionsspektroskopie weiter untersucht. Weitere Hinweise auf Oberflächendefekte wurden gezeigt, da die TOPO-, MUA- und PEI-NRs eine vergleichbare Emissionslebensdauer zeigten, jedoch aufgrund einer besseren Oberflächenpassivierung von PEI, einer Zwischenoberflächenpassivierung von TOPO, jedoch am wenigsten auf MUA, eine sehr unterschiedliche absolute PLQY zeigten -NRs. Transiente Absorptionmessungen lieferten weitere Informationen zu den nicht strahlenden Prozessen. Sogar die strahlende Rekombination war in NRs mit verschiedenen Liganden so unterschiedlich, und die nicht strahlende Rekombination scheint der gleichen Regel zu folgen. Alle dot-in-rod NRs zeigten einen vergleichbaren Zerfall, der nur mit unterschiedlichen Abklingzeitkomponenten mit unterschiedlichen Amplituden nach Datenanalyse verarbeitet wurde und den Einfluss von Oberflächenzuständen enthüllte. Der pH-Stabilitätstest wurde auch durchgeführt, um Informationen in praktischen Anwendungen zu geben. Die MUA- und PEI-NRs zeigten ein großes Potenzial bei den basischen pH-Werten, während HS-PEG-OCH₃-NRs für Anwendungen im sauren oder weiten pH-Bereich eine viel bessere Wahl hinsichtlich der pH-Stabilität waren.

In Kapitel 5 wurden die Wechselwirkungen zwischen NRs und Dopamin und Polydopamin untersucht. Für MUA-NRs und HS-PEG-OCH₃-NRs war der Löschmechanismus ein dynamisches Löschen in Abwesenheit von Sauerstoff aufgrund des Elektronen- bzw. Lochtransfers. Der Löschmechanismus änderte sich zu einem kombinierten dynamischen und statischen Löschen, wenn Sauerstoff für MUA-NRs vorhanden war. Bei HS-PEG-OCH₃-NRs war der Löschmechanismus jedoch aufgrund des Lochtransfermechanismus aufgrund der geringeren Abdeckung der HS-PEG-OCH₃-Liganden immer

noch dynamisch, was zu mehr Elektronenfallen im Vergleich zu MUA-NRs führte. Für P-MUA-NRs zeigten TEM- und stationäre Absorptions- und Emissionsmessungen, dass die Beschichtung mit Dopamin erfolgreich war. In der TA-Spektroskopie wurde ein schneller Elektronentransfer sowohl vom CdS als auch vom CdSe zum Polydopamin beobachtet, während der Elektronentransfer von CdS viel schneller war als der im CdSe, da die CdS-Schale viel näher an der Polydopaminschale lag. Und das Merkmal in beiden Kinetiken, das der Lochlokalisierung zugeordnet ist, fehlte in P-MUA-NRs, was darauf hinweist, dass das Polydopamin den konkurrierenden Prozess der Aufnahme des Elektrons gewonnen hat. Für die HS-PEG-OCH₃-NRs und Dopamin / Polydopamin waren noch zeitaufgelöste Messungen erforderlich, um in Zukunft solide Beweise für den Löschmechanismus zu liefern. Die Ergebnisse in diesem Kapitel haben uns viele mögliche Anwendungen mit dem Elektronen- und Lochtransfer-Löschmechanismus hinterlassen, wie z. B. Sensorik, Photokatalyse und Lochentfernung.

Diese Arbeit lieferte ein ruhiges Gesamtbild in Bezug auf Lochentfernung und Phasentransfer von NRs. Basierend auf den Ergebnissen von Kapitel 3 waren die inside-out NRs für die Lochlokalisierung an der CdSe-Schale sehr vielversprechend, wenn die Oberflächendefekte passiviert werden konnten. Und dies könnte weiter durch Oberflächenpassivierung von PEI erreicht werden, basierend auf den Ergebnissen aus Kapitel 4. Die Oberflächenpassivierung von PEI würde die inside-out NRs wahrscheinlich nicht nur weniger Oberflächendefekte, sondern auch wasserlöslich machen, was die Anwendung als weiter begünstigen würde Photosensibilisatoren. Die Oberflächenpassivierung verschiedener Liganden würde auch zu unterschiedlichen Löschmechanismen führen, wenn die CdSe/CdS dot-in-rod NRs mit Dopamin wechselwirken. Die Löschexperimente von MUA-NRs und Dopamin konnten durch Elektronentransfer von den NRs zu den Dopaminmolekülen und für HS-PEG-OCH₃-NRs durch den Lochtransfer von den NRs zu den Dopaminmolekülen aufgrund von mehr Elektronenfallen erklärt werden auf der Oberfläche der letzteren NRs. Dies war ein starker Hinweis darauf, dass der Elektronen- oder Lochtransferlöschmechanismus durch die Oberflächenzustände der NRs abgestimmt werden konnte, die durch die Oberflächenliganden weiter abgestimmt werden konnten. Zusammen mit den inside-out NRs und verschiedenen Oberflächenliganden wäre das Ziel einer einfachen Lochentfernung nach der Erzeugung von Exzitonen möglich. Und gemäß den TA-Ergebnissen der P-MUA-NRs könnte das Ein- und Ausschalten des Elektronentransfers auch durch Einstellen der pH-Werte eingestellt werden, was weitere Anwendungsmöglichkeiten einführen würde.

Kurzgesagt, die in dieser Arbeit zu NRs vorgestellten Ergebnisse zeigten, dass die Eigenschaften der NRs von innen nach außen, von strukturell bis oberflächlich, mit Wechselwirkungen mit anderen Molekülen enden. Ich weiß, dass ich kein Riese in der Wissenschaft bin, aber ich wünschte immer noch, meine Arbeit würde andere Forscher auf dem Weg zu ihren Errungenschaften inspirieren.

Bibliography

1. Chapman, D.; Mount, T.; Tyrrell, T., Electricity Demand Growth and the Energy Crisis: An analysis of electricity demand growth projections suggests overestimates in the long run. *Science* **1972**, *178* (4062), 703-8.
2. Boulding, K. E., The social system and the energy crisis. *Science* **1974**, *184* (4134), 255-7.
3. Hafele, W., Energy choices that Europe faces: a European view of energy. *Science* **1974**, *184* (4134), 360-7.
4. Hafele, W., A global and long-range picture of energy developments. *Science* **1980**, *209* (4452), 174-82.
5. Popp, M., German energy technology prospects. *Science* **1982**, *218* (4579), 1280-5.
6. Starr, C.; Searl, M. F.; Alpert, S., Energy sources: a realistic outlook. *Science* **1992**, *256* (5059), 981-7.
7. Hoekstra, A. Y.; Wiedmann, T. O., Humanity's unsustainable environmental footprint. *Science* **2014**, *344* (6188), 1114-7.
8. Duffy, P. B.; Field, C. B.; Diffenbaugh, N. S.; Doney, S. C.; Dutton, Z.; Goodman, S.; Heinzerling, L.; Hsiang, S.; Lobell, D. B.; Mickley, L. J.; Myers, S.; Natali, S. M.; Parmesan, C.; Tierney, S.; Williams, A. P., Strengthened scientific support for the Endangerment Finding for atmospheric greenhouse gases. *Science* **2019**, *363* (6427).
9. Green, L., Jr., Energy needs versus environmental pollution: a reconciliation? *Science* **1967**, *156* (3781), 1448-50.
10. Schneider, S. H., The greenhouse effect: science and policy. *Science* **1989**, *243* (4892), 771-81.
11. Wheeler, T.; von Braun, J., Climate change impacts on global food security. *Science* **2013**, *341* (6145), 508-13.
12. Hanley, E. S.; Deane, J. P.; Gallachóir, B. P. Ó., The role of hydrogen in low carbon energy futures—A review of existing perspectives. *Renewable and Sustainable Energy Reviews* **2018**, *82*, 3027-3045.
13. Brandon, N. P.; Kurban, Z., Clean energy and the hydrogen economy. *Philos Trans A Math Phys Eng Sci* **2017**, *375* (2098).
14. Pudukudy, M.; Yaakob, Z.; Mohammad, M.; Narayanan, B.; Sopian, K., Renewable hydrogen economy in Asia – Opportunities and challenges: An overview. *Renewable and Sustainable Energy Reviews* **2014**, *30*, 743-757.

15. Abbasi, T.; Abbasi, S. A., 'Renewable' hydrogen: Prospects and challenges. *Renewable and Sustainable Energy Reviews* **2011**, *15* (6), 3034-3040.
16. Dunn, S., Hydrogen futures: toward a sustainable energy system. *International Journal of Hydrogen Energy* **2002**, *27* (3), 235-264.
17. Tollefson, J., Hydrogen vehicles: Fuel of the future? *Nature* **2010**, *464* (7293), 1262-4.
18. Dodds, P. E.; Demoullin, S., Conversion of the UK gas system to transport hydrogen. *International Journal of Hydrogen Energy* **2013**, *38* (18), 7189-7200.
19. Dodds, P. E.; Staffell, I.; Hawkes, A. D.; Li, F.; Grünewald, P.; McDowall, W.; Ekins, P., Hydrogen and fuel cell technologies for heating: A review. *International Journal of Hydrogen Energy* **2015**, *40* (5), 2065-2083.
20. Napp, T. A.; Gambhir, A.; Hills, T. P.; Florin, N.; Fennell, P. S., A review of the technologies, economics and policy instruments for decarbonising energy-intensive manufacturing industries. *Renewable and Sustainable Energy Reviews* **2014**, *30*, 616-640.
21. Ball, M.; Weeda, M., The hydrogen economy – Vision or reality? 1 This paper is also published as Chapter 11 'The hydrogen economy – vision or reality?' in Compendium of Hydrogen Energy Volume 4: Hydrogen Use, Safety and the Hydrogen Economy, Edited by Michael Ball, Angelo Basile and T. Nejat Veziroglu, published by Elsevier in 2015, ISBN: 978-1-78242-364-5. For further details see: <http://www.elsevier.com/books/compendium-of-hydrogen-energy/ball/978-1-78242-364-5>. *International Journal of Hydrogen Energy* **2015**, *40* (25), 7903-7919.
22. Samsatli, S.; Staffell, I.; Samsatli, N. J., Optimal design and operation of integrated wind-hydrogen-electricity networks for decarbonising the domestic transport sector in Great Britain. *International Journal of Hydrogen Energy* **2016**, *41* (1), 447-475.
23. World Resources Institute, CAIT Climate Data Explorer, <http://cait.wri.org>.
24. Wu, K.; Lian, T., Quantum confined colloidal nanorod heterostructures for solar-to-fuel conversion. *Chem Soc Rev* **2016**, *45* (14), 3781-810.
25. Srdanov, V. I.; Blake, N. P.; Markgraber, D.; Metiu, H.; Stucky, G. D., Alkali Metal and Semiconductor Clusters in Zeolites. In *Advanced Zeolite Science and Applications*, Jansen, J. C.; Stöcker, M.; Karge, H. G.; Weitkamp, J., Eds. Elsevier: 1994; Vol. 85, pp 115-144.
26. Fu, Y.; Hellström, S.; ÅGren, H., Nonlinear Optical Properties of Quantum Dots: Excitons in Nanostructures. *Journal of Nonlinear Optical Physics & Materials* **2012**, *18* (02), 195-226.
27. Gaponenko, S. V.; Woggon, U.; Müller, M.; Klingshirn, C.; Saleh, M.; Langbein, W.; Uhrig, A., Nonlinear-optical properties of semiconductor quantum dots and their correlation with the precipitation stage. *Journal of the Optical Society of America B* **1993**, *10* (10).

28. Panfil, Y. E.; Oded, M.; Banin, U., Colloidal Quantum Nanostructures: Emerging Materials for Display Applications. *Angew Chem Int Ed Engl* **2018**, *57* (16), 4274-4295.
29. Singh, M.; Singhal, A. In *Modeling of Shape and Size Effects for the Band Gap of Semiconductor Nanoparticles*, 2018 2nd International Conference on Micro-Electronics and Telecommunication Engineering (ICMETE), 20-21 Sept. 2018; 2018; pp 339-342.
30. Yang, Q. H.; Cheng, H. M., Carbon nanotubes: Surface, porosity, and related applications. In *Carbon Nanotechnology*, Dai, L., Ed. Elsevier: Amsterdam, 2006; pp 323-359.
31. Peng, Z. A.; Peng, X., Nearly monodisperse and shape-controlled CdSe nanocrystals via alternative routes: nucleation and growth. *J Am Chem Soc* **2002**, *124* (13), 3343-53.
32. Bang, J.; Yang, H.; Holloway, P. H., Enhanced and stable green emission of ZnO nanoparticles by surface segregation of Mg. *Nanotechnology* **2006**, *17* (4), 973-8.
33. Wu, K.; Rodriguez-Cordoba, W. E.; Liu, Z.; Zhu, H.; Lian, T., Beyond band alignment: hole localization driven formation of three spatially separated long-lived exciton states in CdSe/CdS nanorods. *ACS Nano* **2013**, *7* (8), 7173-85.
34. Dai, X.; Zhang, Z.; Jin, Y.; Niu, Y.; Cao, H.; Liang, X.; Chen, L.; Wang, J.; Peng, X., Solution-processed, high-performance light-emitting diodes based on quantum dots. *Nature* **2014**, *515* (7525), 96-9.
35. Lee, K. H.; Lee, J. H.; Song, W. S.; Ko, H.; Lee, C.; Lee, J. H.; Yang, H., Highly efficient, color-pure, color-stable blue quantum dot light-emitting devices. *ACS Nano* **2013**, *7* (8), 7295-302.
36. Shirasaki, Y.; Supran, G. J.; Bawendi, M. G.; Bulović, V., Emergence of colloidal quantum-dot light-emitting technologies. *Nature Photonics* **2012**, *7* (1), 13-23.
37. Dai, X.; Deng, Y.; Peng, X.; Jin, Y., Quantum-Dot Light-Emitting Diodes for Large-Area Displays: Towards the Dawn of Commercialization. *Adv Mater* **2017**, *29* (14).
38. Snee, P. T.; Somers, R. C.; Nair, G.; Zimmer, J. P.; Bawendi, M. G.; Nocera, D. G., A ratiometric CdSe/ZnS nanocrystal pH sensor. *J Am Chem Soc* **2006**, *128* (41), 13320-1.
39. Vlaskin, V. A.; Janssen, N.; van Rijssel, J.; Beaulac, R.; Gamelin, D. R., Tunable dual emission in doped semiconductor nanocrystals. *Nano Lett* **2010**, *10* (9), 3670-4.
40. McLaurin, E. J.; Vlaskin, V. A.; Gamelin, D. R., Water-soluble dual-emitting nanocrystals for ratiometric optical thermometry. *J Am Chem Soc* **2011**, *133* (38), 14978-80.
41. Michalet, X.; Pinaud, F. F.; Bentolila, L. A.; Tsay, J. M.; Doose, S.; Li, J. J.; Sundaresan, G.; Wu, A. M.; Gambhir, S. S.; Weiss, S., Quantum dots for live cells, in vivo imaging, and diagnostics. *Science* **2005**, *307* (5709), 538-44.
42. Bruchez, M., Jr.; Moronne, M.; Gin, P.; Weiss, S.; Alivisatos, A. P., Semiconductor nanocrystals as fluorescent biological labels. *Science* **1998**, *281* (5385), 2013-6.

43. Chan, W. C.; Nie, S., Quantum dot bioconjugates for ultrasensitive nonisotopic detection. *Science* **1998**, *281* (5385), 2016-8.
44. Nel, A. E.; Madler, L.; Velegol, D.; Xia, T.; Hoek, E. M.; Somasundaran, P.; Klaessig, F.; Castranova, V.; Thompson, M., Understanding biophysicochemical interactions at the nano-bio interface. *Nat Mater* **2009**, *8* (7), 543-57.
45. Yu, J. H.; Kwon, S. H.; Petrusek, Z.; Park, O. K.; Jun, S. W.; Shin, K.; Choi, M.; Park, Y. I.; Park, K.; Na, H. B.; Lee, N.; Lee, D. W.; Kim, J. H.; Schwille, P.; Hyeon, T., High-resolution three-photon biomedical imaging using doped ZnS nanocrystals. *Nat Mater* **2013**, *12* (4), 359-66.
46. Lv, H.; Wang, C.; Li, G.; Burke, R.; Krauss, T. D.; Gao, Y.; Eisenberg, R., Semiconductor quantum dot-sensitized rainbow photocathode for effective photoelectrochemical hydrogen generation. *Proc Natl Acad Sci U S A* **2017**, *114* (43), 11297-11302.
47. Huang, Y.; Zhu, Y.; Egap, E., Semiconductor Quantum Dots as Photocatalysts for Controlled Light-Mediated Radical Polymerization. *ACS Macro Letters* **2018**, *7* (2), 184-189.
48. Nakibli, Y.; Amirav, L., Selective Growth of Ni Tips on Nanorod Photocatalysts. *Chemistry of Materials* **2016**, *28* (13), 4524-4527.
49. Coropceanu, I. Colloidal CdSe/CdS nanostructures : synthesis, optical characterization and applications. PhD Thesis, Massachusetts Institute of Technology, 2016.
50. Sanguinetti, S.; Guzzi, M.; Gatti, E.; Gurioli, M., Photoluminescence Characterization of Structural and Electronic Properties of Semiconductor Quantum Wells. In *Characterization of Semiconductor Heterostructures and Nanostructures*, Lamberti, C.; Agostini, G., Eds. Elsevier: Oxford, 2013; pp 509-556.
51. Medintz, I. L.; Uyeda, H. T.; Goldman, E. R.; Mattoussi, H., Quantum dot bioconjugates for imaging, labelling and sensing. *Nat Mater* **2005**, *4* (6), 435-46.
52. Efros, A. L.; Efros, A. L., Interband absorption of light in a semiconductor sphere. *Soviet Physics Semiconductors-Ussr* **1982**, *16* (7), 772-775.
53. Brus, L. E., Electron-electron and electron-hole interactions in small semiconductor crystallites: The size dependence of the lowest excited electronic state. *The Journal of Chemical Physics* **1984**, *80* (9), 4403-4409.
54. Brus, L., Electronic wave functions in semiconductor clusters: experiment and theory. *The Journal of Physical Chemistry* **1986**, *90* (12), 2555-2560.
55. Brus, L. E., A simple model for the ionization potential, electron affinity, and aqueous redox potentials of small semiconductor crystallites. *The Journal of Chemical Physics* **1983**, *79* (11), 5566-5571.

56. Bawendi, M. G.; Steigerwald, M. L.; Brus, L. E., The Quantum Mechanics of Larger Semiconductor Clusters ("Quantum Dots"). *Annual Review of Physical Chemistry* **1990**, *41* (1), 477-496.
57. Steigerwald, M. L.; Brus, L. E., Semiconductor crystallites: a class of large molecules. *Accounts of Chemical Research* **2002**, *23* (6), 183-188.
58. Kippeny, T.; Swafford, L. A.; Rosenthal, S. J., Semiconductor Nanocrystals: A Powerful Visual Aid for Introducing the Particle in a Box. *Journal of Chemical Education* **2002**, *79* (9), 1094.
59. Smith, A. M.; Nie, S., Chemical analysis and cellular imaging with quantum dots. *Analyst* **2004**, *129* (8), 672-7.
60. Spanhel, L.; Haase, M.; Weller, H.; Henglein, A., Photochemistry of colloidal semiconductors. 20. Surface modification and stability of strong luminescing CdS particles. *Journal of the American Chemical Society* **1987**, *109* (19), 5649-5655.
61. Klimov, V. I.; Haring-Bolivar, P.; Kurz, H.; Karavanskii, V. A., Optical nonlinearities and carrier trapping dynamics in CdS and CuxS nanocrystals. *Superlattices and Microstructures* **1996**, *20* (3), 395-404.
62. Klimov, V. V.; Bolivar, P. H.; Kurz, H., Ultrafast carrier dynamics in semiconductor quantum dots. *Phys Rev B Condens Matter* **1996**, *53* (3), 1463-1467.
63. Dannhauser, T.; O'Neil, M.; Johansson, K.; Whitten, D.; McLendon, G., Photophysics of quantized colloidal semiconductors. Dramatic luminescence enhancement by binding of simple amines. *The Journal of Physical Chemistry* **1986**, *90* (23), 6074-6076.
64. Hines, M. A.; Guyot-Sionnest, P., Synthesis and Characterization of Strongly Luminescing ZnS-Capped CdSe Nanocrystals. *The Journal of Physical Chemistry* **1996**, *100* (2), 468-471.
65. Dabbousi, B. O.; Rodriguez-Viejo, J.; Mikulec, F. V.; Heine, J. R.; Mattoussi, H.; Ober, R.; Jensen, K. F.; Bawendi, M. G., (CdSe)ZnS Core-Shell Quantum Dots: Synthesis and Characterization of a Size Series of Highly Luminescent Nanocrystallites. *The Journal of Physical Chemistry B* **1997**, *101* (46), 9463-9475.
66. Kern, S. J.; Sahu, K.; Berg, M. A., Heterogeneity of the electron-trapping kinetics in CdSe nanoparticles. *Nano Lett* **2011**, *11* (8), 3493-8.
67. Zhu, H.; Song, N.; Lian, T., Controlling charge separation and recombination rates in CdSe/ZnS type I core-shell quantum dots by shell thicknesses. *J Am Chem Soc* **2010**, *132* (42), 15038-45.
68. Cao, Y.; Stavrinadis, A.; Lasanta, T.; So, D.; Konstantatos, G., The role of surface passivation for efficient and photostable PbS quantum dot solar cells. *Nature Energy* **2016**, *1* (4), 16035.

69. Wang, Q.; Kuo, Y.; Wang, Y.; Shin, G.; Ruengruglikit, C.; Huang, Q., Luminescent properties of water-soluble denatured bovine serum albumin-coated CdTe quantum dots. *J Phys Chem B* **2006**, *110* (34), 16860-6.
70. Steigerwald, M. L.; Alivisatos, A. P.; Gibson, J. M.; Harris, T. D.; Kortan, R.; Muller, A. J.; Thayer, A. M.; Duncan, T. M.; Douglass, D. C.; Brus, L. E., Surface derivatization and isolation of semiconductor cluster molecules. *Journal of the American Chemical Society* **1988**, *110* (10), 3046-3050.
71. Murray, C. B.; Kagan, C. R.; Bawendi, M. G., Self-Organization of CdSe Nanocrystallites into Three-Dimensional Quantum Dot Superlattices. *Science* **1995**, *270* (5240), 1335-1338.
72. Ma, N.; Yang, J.; Stewart, K. M.; Kelley, S. O., DNA-passivated CdS nanocrystals: luminescence, bioimaging, and toxicity profiles. *Langmuir* **2007**, *23* (26), 12783-7.
73. Murray, C. B.; Norris, D. J.; Bawendi, M. G., Synthesis and characterization of nearly monodisperse CdE (E = sulfur, selenium, tellurium) semiconductor nanocrystallites. *Journal of the American Chemical Society* **1993**, *115* (19), 8706-8715.
74. Bai, S.; Yin, W.; Wang, L.; Li, Z.; Xiong, Y., Surface and Interface Design in Cocatalysts for Photocatalytic Water Splitting and CO₂ Reduction. *RSC Adv.* **2016**, *6*, 57446.
75. Barber, J., Photosynthetic energy conversion: natural and artificial. *Chem Soc Rev* **2009**, *38* (1), 185-96.
76. Ben-Shahar, Y.; Scotognella, F.; Waiskopf, N.; Kriegel, I.; Dal Conte, S.; Cerullo, G.; Banin, U., Effect of surface coating on the photocatalytic function of hybrid CdS-Au nanorods. *Small* **2015**, *11* (4), 462-71.
77. Kalisman, P.; Nakibli, Y.; Amirav, L., Perfect Photon-to-Hydrogen Conversion Efficiency. *Nano Lett* **2016**, *16* (3), 1776-81.
78. Ansar, S. M.; Chakraborty, S.; Kitchens, C. L., pH-Responsive Mercaptoundecanoic Acid Functionalized Gold Nanoparticles and Applications in Catalysis. *Nanomaterials (Basel)* **2018**, *8* (5), 339-351.
79. Ballou, B.; Lagerholm, B. C.; Ernst, L. A.; Bruchez, M. P.; Waggoner, A. S., Noninvasive imaging of quantum dots in mice. *Bioconjug Chem* **2004**, *15* (1), 79-86.
80. Duan, H.; Nie, S., Cell-penetrating quantum dots based on multivalent and endosome-disrupting surface coatings. *J Am Chem Soc* **2007**, *129* (11), 3333-8.
81. Pang, Z.; Zhang, J.; Cao, W.; Kong, X.; Peng, X., Partitioning surface ligands on nanocrystals for maximal solubility. *Nat Commun* **2019**, *10* (1), 2454.
82. Becerra, L. R.; Murray, C. B.; Griffin, R. G.; Bawendi, M. G., Investigation of the surface morphology of capped CdSe nanocrystallites by ³¹P nuclear magnetic resonance. *The Journal of Chemical Physics* **1994**, *100* (4), 3297-3300.

83. Vassiltsova, O. V.; Zhao, Z.; Petrukhina, M. A.; Carpenter, M. A., Surface-functionalized CdSe quantum dots for the detection of hydrocarbons. *Sensors and Actuators B: Chemical* **2007**, *123* (1), 522-529.
84. Talapin, D. V.; Rogach, A. L.; Mekis, I.; Haubold, S.; Kornowski, A.; Haase, M.; Weller, H., Synthesis and surface modification of amino-stabilized CdSe, CdTe and InP nanocrystals. *Colloids and Surfaces A: Physicochemical and Engineering Aspects* **2002**, *202* (2-3), 145-154.
85. Talapin, D. V.; Rogach, A. L.; Kornowski, A.; Haase, M.; Weller, H., Highly Luminescent Monodisperse CdSe and CdSe/ZnS Nanocrystals Synthesized in a Hexadecylamine–Trioctylphosphine Oxide–Trioctylphosphine Mixture. *Nano Letters* **2001**, *1* (4), 207-211.
86. Green, M., The nature of quantum dot capping ligands. *Journal of Materials Chemistry* **2010**, *20* (28), 5797-5809.
87. Bao, Y.; Beerman, M.; Pakhomov, A. B.; Krishnan, K. M., Controlled crystalline structure and surface stability of cobalt nanocrystals. *J Phys Chem B* **2005**, *109* (15), 7220-2.
88. Yan, Y.; Chen, G.; Van Patten, P. G., Ultrafast Exciton Dynamics in CdTe Nanocrystals and Core/Shell CdTe/CdS Nanocrystals. *The Journal of Physical Chemistry C* **2011**, *115* (46), 22717-22728.
89. Yu, W. W.; Wang, Y. A.; Peng, X., Formation and Stability of Size-, Shape-, and Structure-Controlled CdTe Nanocrystals: Ligand Effects on Monomers and Nanocrystals. *Chemistry of Materials* **2003**, *15* (22), 4300-4308.
90. Bera, D.; Qian, L.; Tseng, T.-K.; Holloway, P. H., Quantum Dots and Their Multimodal Applications: A Review. *Materials* **2010**, *3* (4), 2260-2345.
91. Maity, P.; Debnath, T.; Ghosh, H. N., Ultrafast Charge Carrier Delocalization in CdSe/CdS Quasi-Type II and CdS/CdSe Inverted Type I Core–Shell: A Structural Analysis through Carrier-Quenching Study. *The Journal of Physical Chemistry C* **2015**, *119* (46), 26202-26211.
92. Nakibli, Y.; Mazal, Y.; Dubi, Y.; Wachtler, M.; Amirav, L., Size Matters: Cocatalyst Size Effect on Charge Transfer and Photocatalytic Activity. *Nano Lett* **2018**, *18* (1), 357-364.
93. Peng, X.; Schlamp, M. C.; Kadavanich, A. V.; Alivisatos, A. P., Epitaxial Growth of Highly Luminescent CdSe/CdS Core/Shell Nanocrystals with Photostability and Electronic Accessibility. *Journal of the American Chemical Society* **1997**, *119* (30), 7019-7029.
94. Reiss, P.; Bleuse, J.; Pron, A., Highly Luminescent CdSe/ZnSe Core/Shell Nanocrystals of Low Size Dispersion. *Nano Letters* **2002**, *2* (7), 781-784.
95. Qian, L.; Bera, D.; Tseng, T.-K.; Holloway, P. H., High efficiency photoluminescence from silica-coated CdSe quantum dots. *Applied Physics Letters* **2009**, *94* (7).

96. Chen, X.; Lou, Y.; Samia, A. C.; Burda, C., Coherency Strain Effects on the Optical Response of Core/Shell Heteronanostructures. *Nano Letters* **2003**, *3* (6), 799-803.
97. Kortan, A. R.; Hull, R.; Opila, R. L.; Bawendi, M. G.; Steigerwald, M. L.; Carroll, P. J.; Brus, L. E., Nucleation and Growth of CdSe on ZnS Quantum Crystallite Seeds, and Vice Versa, in Inverse Micelle Media. *Journal of the American Chemical Society* **2002**, *112* (4), 1327-1332.
98. Danek, M.; Jensen, K. F.; Murray, C. B.; Bawendi, M. G., Synthesis of Luminescent Thin-Film CdSe/ZnSe Quantum Dot Composites Using CdSe Quantum Dots Passivated with an Overlayer of ZnSe. *Chemistry of Materials* **1996**, *8* (1), 173-180.
99. Hoener, C. F.; Allan, K. A.; Bard, A. J.; Campion, A.; Fox, M. A.; Mallouk, T. E.; Webber, S. E.; White, J. M., Demonstration of a shell-core structure in layered cadmium selenide-zinc selenide small particles by x-ray photoelectron and Auger spectroscopies. *The Journal of Physical Chemistry* **1992**, *96* (9), 3812-3817.
100. Tian, Y.; Newton, T.; Kotov, N. A.; Guldi, D. M.; Fendler, J. H., Coupled Composite CdS-CdSe and Core-Shell Types of (CdS)CdSe and (CdSe)CdS Nanoparticles. *The Journal of Physical Chemistry* **1996**, *100* (21), 8927-8939.
101. Chon, B.; Lim, S. J.; Kim, W.; Seo, J.; Kang, H.; Joo, T.; Hwang, J.; Shin, S. K., Shell and ligand-dependent blinking of CdSe-based core/shell nanocrystals. *Phys Chem Chem Phys* **2010**, *12* (32), 9312-9.
102. Chen, O.; Zhao, J.; Chauhan, V. P.; Cui, J.; Wong, C.; Harris, D. K.; Wei, H.; Han, H. S.; Fukumura, D.; Jain, R. K.; Bawendi, M. G., Compact high-quality CdSe-CdS core-shell nanocrystals with narrow emission linewidths and suppressed blinking. *Nat Mater* **2013**, *12* (5), 445-51.
103. Qin, H.; Niu, Y.; Meng, R.; Lin, X.; Lai, R.; Fang, W.; Peng, X., Single-dot spectroscopy of zinc-blende CdSe/CdS core/shell nanocrystals: nonblinking and correlation with ensemble measurements. *J Am Chem Soc* **2014**, *136* (1), 179-87.
104. Yang, Z.; Chen, C. Y.; Liu, C. W.; Chang, H. T., Electrocatalytic sulfur electrodes for CdS/CdSe quantum dot-sensitized solar cells. *Chem Commun (Camb)* **2010**, *46* (30), 5485-7.
105. Zhong, X.; Xie, R.; Zhang, Y.; Basché, T.; Knoll, W., High-Quality Violet- to Red-Emitting ZnSe/CdSe Core/Shell Nanocrystals. *Chemistry of Materials* **2005**, *17* (16), 4038-4042.
106. Shen, G.; Guyot-Sionnest, P., HgS and HgS/CdS Colloidal Quantum Dots with Infrared Intraband Transitions and Emergence of a Surface Plasmon. *The Journal of Physical Chemistry C* **2016**, *120* (21), 11744-11753.
107. Lee, Y.-L.; Lo, Y.-S., Highly Efficient Quantum-Dot-Sensitized Solar Cell Based on Co-Sensitization of CdS/CdSe. *Advanced Functional Materials* **2009**, *19* (4), 604-609.
108. Sambur, J. B.; Parkinson, B. A., CdSe/ZnS core/shell quantum dot sensitization of low index TiO(2) single crystal surfaces. *J Am Chem Soc* **2010**, *132* (7), 2130-1.

109. Jin, X.; Bai, J.; Gu, X.; Chang, C.; Shen, H.; Zhang, Q.; Li, F.; Chen, Z.; Li, Q., Efficient light-emitting diodes based on reverse type-I quantum dots. *Optical Materials Express* **2017**, *7* (12).
110. AbouElhamd, A.; Al-Sallal, K.; Hassan, A., Review of Core/Shell Quantum Dots Technology Integrated into Building's Glazing. *Energies* **2019**, *12* (6).
111. Kim, S.; Fisher, B.; Eisler, H. J.; Bawendi, M., Type-II quantum dots: CdTe/CdSe(core/shell) and CdSe/ZnTe(core/shell) heterostructures. *J Am Chem Soc* **2003**, *125* (38), 11466-7.
112. Ning, Z.; Tian, H.; Yuan, C.; Fu, Y.; Qin, H.; Sun, L.; Ågren, H., Solar cells sensitized with type-II ZnSe–CdS core/shell colloidal quantum dots. *Chem. Commun.* **2011**, *47* (5), 1536-1538.
113. Yu, X.-Y.; Lei, B.-X.; Kuang, D.-B.; Su, C.-Y., Highly efficient CdTe/CdS quantum dot sensitized solar cells fabricated by a one-step linker assisted chemical bath deposition. *Chemical Science* **2011**, *2* (7).
114. Jiao, S.; Shen, Q.; Mora-Seró, I.; Wang, J.; Pan, Z.; Zhao, K.; Kuga, Y.; Zhong, X.; Bisquert, J., Band Engineering in Core/Shell ZnTe/CdSe for Photovoltage and Efficiency Enhancement in Exciplex Quantum Dot Sensitized Solar Cells. *ACS Nano* **2015**, *9* (1), 908-915.
115. Sitt, A.; Della Sala, F.; Menagen, G.; Banin, U., Multiexciton engineering in seeded core/shell nanorods: transfer from type-I to quasi-type-II regimes. *Nano Lett* **2009**, *9* (10), 3470-6.
116. Raino, G.; Stoferle, T.; Moreels, I.; Gomes, R.; Kamal, J. S.; Hens, Z.; Mahrt, R. F., Probing the wave function delocalization in CdSe/CdS dot-in-rod nanocrystals by time- and temperature-resolved spectroscopy. *ACS Nano* **2011**, *5* (5), 4031-6.
117. Smith, E. R.; Luther, J. M.; Johnson, J. C., Ultrafast electronic delocalization in CdSe/CdS quantum rod heterostructures. *Nano Lett* **2011**, *11* (11), 4923-31.
118. Wu, K.; Hill, L. J.; Chen, J.; McBride, J. R.; Pavlopolous, N. G.; Richey, N. E.; Pyun, J.; Lian, T., Universal Length Dependence of Rod-to-Seed Exciton Localization Efficiency in Type I and Quasi-Type II CdSe@CdS Nanorods. *ACS Nano* **2015**, *9* (4), 4591-9.
119. Christodoulou, S.; Rajadell, F.; Casu, A.; Vaccaro, G.; Grim, J. Q.; Genovese, A.; Manna, L.; Climente, J. I.; Meinardi, F.; Raino, G.; Stoferle, T.; Mahrt, R. F.; Planelles, J.; Brovelli, S.; Moreels, I., Band structure engineering via piezoelectric fields in strained anisotropic CdSe/CdS nanocrystals. *Nat Commun* **2015**, *6*, 7905.
120. Dubertret, B.; Skourides, P.; Norris, D. J.; Noireaux, V.; Brivanlou, A. H.; Libchaber, A., In vivo imaging of quantum dots encapsulated in phospholipid micelles. *Science* **2002**, *298* (5599), 1759-62.
121. Pelley, J. L.; Daar, A. S.; Saner, M. A., State of academic knowledge on toxicity and biological fate of quantum dots. *Toxicol Sci* **2009**, *112* (2), 276-96.

122. Jun, Y. W.; Choi, J. S.; Cheon, J., Shape control of semiconductor and metal oxide nanocrystals through nonhydrolytic colloidal routes. *Angew Chem Int Ed Engl* **2006**, *45* (21), 3414-39.
123. Ratsch, C.; Zangwill, A., Equilibrium theory of the Stranski-Krastanov epitaxial morphology. *Surface Science* **1993**, *293* (1-2), 123-131.
124. Ma, C.; Ding, Y.; Moore, D.; Wang, X.; Wang, Z. L., Single-crystal CdSe nanosaws. *J Am Chem Soc* **2004**, *126* (3), 708-9.
125. Zhang, Y.; Wang, L.; Liu, X.; Yan, Y.; Chen, C.; Zhu, J., Synthesis of nano/micro zinc oxide rods and arrays by thermal evaporation approach on cylindrical shape substrate. *J Phys Chem B* **2005**, *109* (27), 13091-3.
126. Pan, Z. W.; Dai, Z. R.; Xu, L.; Lee, S. T.; Wang, Z. L., Temperature-Controlled Growth of Silicon-Based Nanostructures by Thermal Evaporation of SiO Powders. *The Journal of Physical Chemistry B* **2001**, *105* (13), 2507-2514.
127. Walter, P.; Welcomme, E.; Hallegot, P.; Zaluzec, N. J.; Deeb, C.; Castaing, J.; Veysiere, P.; Breniaux, R.; Leveque, J. L.; Tsoucaris, G., Early use of PbS nanotechnology for an ancient hair dyeing formula. *Nano Lett* **2006**, *6* (10), 2215-9.
128. McDonald, S. A.; Konstantatos, G.; Zhang, S.; Cyr, P. W.; Klem, E. J.; Levina, L.; Sargent, E. H., Solution-processed PbS quantum dot infrared photodetectors and photovoltaics. *Nat Mater* **2005**, *4* (2), 138-42.
129. Levina, L.; Sukhovatkin, V.; Musikhin, S.; Cauchi, S.; Nisman, R.; Bazett-Jones, D. P.; Sargent, E. H., Efficient Infrared-Emitting PbS Quantum Dots Grown on DNA and Stable in Aqueous Solution and Blood Plasma. *Advanced Materials* **2005**, *17* (15), 1854-1857.
130. Kulkarni, S. K., *Nanotechnology: Principles and Practices*. 2015.
131. Salas, G.; Costo, R.; Morales, M. d. P., Synthesis of Inorganic Nanoparticles. In *Nanobiotechnology - Inorganic Nanoparticles vs Organic Nanoparticles*, de la Fuente, J. M.; Grazu, V., Eds. Elsevier: 2012; Vol. 4, pp 35-79.
132. Park, J.; Joo, J.; Kwon, S. G.; Jang, Y.; Hyeon, T., Synthesis of monodisperse spherical nanocrystals. *Angew Chem Int Ed Engl* **2007**, *46* (25), 4630-60.
133. Li, J. J.; Wang, Y. A.; Guo, W.; Keay, J. C.; Mishima, T. D.; Johnson, M. B.; Peng, X., Large-scale synthesis of nearly monodisperse CdSe/CdS core/shell nanocrystals using air-stable reagents via successive ion layer adsorption and reaction. *J Am Chem Soc* **2003**, *125* (41), 12567-75.
134. Talapin, D. V.; Nelson, J. H.; Shevchenko, E. V.; Aloni, S.; Sadtler, B.; Alivisatos, A. P., Seeded growth of highly luminescent CdSe/CdS nanoheterostructures with rod and tetrapod morphologies. *Nano Lett* **2007**, *7* (10), 2951-9.
135. Peng, X.; Manna, L.; Yang, W.; Wickham, J.; Scher, E.; Kadavanich, A.; Alivisatos, A. P., Shape control of CdSe nanocrystals. *Nature* **2000**, *404* (6773), 59-61.

136. Li, L.-s.; Hu, J.; Yang, W.; Alivisatos, A. P., Band Gap Variation of Size- and Shape-Controlled Colloidal CdSe Quantum Rods. *Nano Letters* **2001**, *1* (7), 349-351.
137. Li, J.; Wang, Shape Effects on Electronic States of Nanocrystals. *Nano Lett* **2003**, *3* (10), 1357-1363.
138. Koh, W. K.; Bartnik, A. C.; Wise, F. W.; Murray, C. B., Synthesis of monodisperse PbSe nanorods: a case for oriented attachment. *J Am Chem Soc* **2010**, *132* (11), 3909-13.
139. Carbone, L.; Nobile, C.; De Giorgi, M.; Sala, F. D.; Morello, G.; Pompa, P.; Hytch, M.; Snoeck, E.; Fiore, A.; Franchini, I. R.; Nadasan, M.; Silvestre, A. F.; Chiodo, L.; Kudera, S.; Cingolani, R.; Krahn, R.; Manna, L., Synthesis and micrometer-scale assembly of colloidal CdSe/CdS nanorods prepared by a seeded growth approach. *Nano Lett* **2007**, *7* (10), 2942-50.
140. Mokari, T.; Rothenberg, E.; Popov, I.; Costi, R.; Banin, U., Selective growth of metal tips onto semiconductor quantum rods and tetrapods. *Science* **2004**, *304* (5678), 1787-90.
141. Habas, S. E.; Yang, P.; Mokari, T., Selective growth of metal and binary metal tips on CdS nanorods. *J Am Chem Soc* **2008**, *130* (11), 3294-5.
142. Wu, K.; Du, Y.; Tang, H.; Chen, Z.; Lian, T., Efficient Extraction of Trapped Holes from Colloidal CdS Nanorods. *J Am Chem Soc* **2015**, *137* (32), 10224-30.
143. Berr, M. J.; Wagner, P.; Fischbach, S.; Vaneski, A.; Schneider, J.; Susha, A. S.; Rogach, A. L.; Jäckel, F.; Feldmann, J., Hole scavenger redox potentials determine quantum efficiency and stability of Pt-decorated CdS nanorods for photocatalytic hydrogen generation. *Applied Physics Letters* **2012**, *100* (22), 223903.
144. Acharya, K. P.; Khnayzer, R. S.; O'Connor, T.; Diederich, G.; Kirsanova, M.; Klinkova, A.; Roth, D.; Kinder, E.; Imboden, M.; Zamkov, M., Correction to The Role of Hole Localization in Sacrificial Hydrogen Production by Semiconductor-Metal Heterostructured Nanocrystals. *Nano Letters* **2011**, *12* (1), 522-522.
145. Wu, K.; Rodriguez-Cordoba, W.; Lian, T., Exciton localization and dissociation dynamics in CdS and CdS-Pt quantum confined nanorods: effect of nonuniform rod diameters. *J Phys Chem B* **2014**, *118* (49), 14062-9.
146. Simon, T.; Carlson, M. T.; Stolarczyk, J. K.; Feldmann, J., Electron Transfer Rate vs Recombination Losses in Photocatalytic H₂ Generation on Pt-Decorated CdS Nanorods. *ACS Energy Letters* **2016**, *1* (6), 1137-1142.
147. Wu, K.; Chen, Z.; Lv, H.; Zhu, H.; Hill, C. L.; Lian, T., Hole removal rate limits photodriven H₂ generation efficiency in CdS-Pt and CdSe/CdS-Pt semiconductor nanorod-metal tip heterostructures. *J Am Chem Soc* **2014**, *136* (21), 7708-16.
148. Marcus, R. A.; Sutin, N., Electron transfers in chemistry and biology. *Biochimica et Biophysica Acta (BBA) - Reviews on Bioenergetics* **1985**, *811* (3), 265-322.

149. Yu, W. W.; Qu, L.; Guo, W.; Peng, X., Experimental Determination of the Extinction Coefficient of CdTe, CdSe, and CdS Nanocrystals. *Chemistry of Materials* **2003**, *15* (14), 2854-2860.
150. Amirav, L.; Alivisatos, A. P., Photocatalytic Hydrogen Production with Tunable Nanorod Heterostructures. *The Journal of Physical Chemistry Letters* **2010**, *1* (7), 1051-1054.
151. Uyeda, H. T.; Medintz, I. L.; Jaiswal, J. K.; Simon, S. M.; Mattoussi, H., Synthesis of compact multidentate ligands to prepare stable hydrophilic quantum dot fluorophores. *J Am Chem Soc* **2005**, *127* (11), 3870-8.
152. Nann, T., Phase-transfer of CdSe@ZnS quantum dots using amphiphilic hyperbranched polyethylenimine. *Chem Commun (Camb)* **2005**, (13), 1735-6.
153. Brochure, Jasco V-780-CFR UV-Vis-NIR double beam spectrophotometer.
154. Letter from James Gregory to John Collins, dated 13 May 1673. Reprinted in: Rigaud, Stephen Jordan, ed. (1841). *Correspondence of Scientific Men of the Seventeenth Century*, Oxford University Press, pp. 251-5.
155. Braslavsky, S. E., *Glossary of Terms Used in Photochemistry, 3rd Edition (IUPAC Recommendations 2006)*. Pure Appl. Chem.: 2007; Vol. 79.
156. Lakowicz, J. R., *Principles of Fluorescence Spectroscopy*. 3 ed.; Springer US: 2006.
157. Mooney, J.; Kambhampati, P., Get the Basics Right: Jacobian Conversion of Wavelength and Energy Scales for Quantitative Analysis of Emission Spectra. *The Journal of Physical Chemistry Letters* **2013**, *4* (19), 3316-3318.
158. FLS980-Spectrometer. <https://www.edinst.com/wp-content/uploads/2015/04/FLS980-Spectrometer.pdf>.
159. Porres, L.; Holland, A.; Palsson, L. O.; Monkman, A. P.; Kemp, C.; Beeby, A., Absolute measurements of photoluminescence quantum yields of solutions using an integrating sphere. *J Fluoresc* **2006**, *16* (2), 267-72.
160. Suzuki, K.; Kobayashi, A.; Kaneko, S.; Takehira, K.; Yoshihara, T.; Ishida, H.; Shiina, Y.; Oishi, S.; Tobita, S., Reevaluation of absolute luminescence quantum yields of standard solutions using a spectrometer with an integrating sphere and a back-thinned CCD detector. *Phys Chem Chem Phys* **2009**, *11* (42), 9850-60.
161. Wu, J. L. a. N., *Biosensors Based on Nanomaterials and Nanodevices*. CRC Press,: 2017.
162. Williams, A. T. R.; Winfield, S. A.; Miller, J. N., Relative fluorescence quantum yields using a computer-controlled luminescence spectrometer. *The Analyst* **1983**, *108* (1290), 1067-1071.

163. Wokaun, A., B. Schrader: Infrared and Raman Spectroscopy - Methods and Applications. VCH, Weinheim, 1995, DM 298,-, ISBN 3-527-26446-9. *Berichte der Bunsengesellschaft für physikalische Chemie* **1996**, 100 (7), 1268-1268.
164. Bruker Tensor 27 FTIR Instructions. <https://www.ru.nl/publish/pages/609550/bruker-tensor-ftir-instructions.pdf>.
165. Salin F. (2005) How to Manipulate and Change the Characteristics of Laser Pulses. In: Rullière C. (eds) Femtosecond Laser Pulses. Advanced Texts in Physics. Springer, New York, NY. https://doi.org/10.1007/0-387-26674-7_6.
166. Rullière C., Amand T., Marie X. (1998) Spectroscopic Methods for Analysis of Sample Dynamics. In: Rullière C. (eds) Femtosecond Laser Pulses. Springer, Berlin, Heidelberg. https://doi.org/10.1007/978-3-662-03682-2_8.
167. Dietzek, B.; Pascher, T.; Sundström, V.; Yartsev, A., Appearance of coherent artifact signals in femtosecond transient absorption spectroscopy in dependence on detector design. *Laser Physics Letters* **2007**, 4 (1), 38-43.
168. Bold, S.; Zedler, L.; Zhang, Y.; Massin, J.; Artero, V.; Chavarot-Kerlidou, M.; Dietzek, B., Electron transfer in a covalent dye-cobalt catalyst assembly - a transient absorption spectroelectrochemistry perspective. *Chem Commun (Camb)* **2018**, 54 (75), 10594-10597.
169. FluorTools. DecayFit - Fluorescence Decay Analysis Software 1.4; 2014.
170. Khon, E.; Lambright, K.; Khayzer, R. S.; Moroz, P.; Perera, D.; Butaeva, E.; Lambright, S.; Castellano, F. N.; Zamkov, M., Improving the catalytic activity of semiconductor nanocrystals through selective domain etching. *Nano Lett* **2013**, 13 (5), 2016-23.
171. Halpert, J. E.; Porter, V. J.; Zimmer, J. P.; Bawendi, M. G., Synthesis of CdSe/CdTe nanobarells. *J Am Chem Soc* **2006**, 128 (39), 12590-1.
172. Kirsanova, M.; Nemchinov, A.; Hewa-Kasakarage, N. N.; Schmall, N.; Zamkov, M., Synthesis of ZnSe/CdS/ZnSe Nanobarells Showing Photoinduced Charge Separation. *Chemistry of Materials* **2009**, 21 (18), 4305-4309.
173. Cohen, L. Coupling the Photosystem with Nanoscale Photocatalysts for Overall Solar Water Splitting. Technion Haifa, 2019.
174. Oh, N.; Nam, S.; Zhai, Y.; Deshpande, K.; Trefonas, P.; Shim, M., Double-heterojunction nanorods. *Nat Commun* **2014**, 5 (1), 3642.
175. Talapin, D. V.; Koeppel, R.; Götzinger, S.; Kornowski, A.; Lupton, J. M.; Rogach, A. L.; Benson, O.; Feldmann, J.; Weller, H., Highly Emissive Colloidal CdSe/CdS Heterostructures of Mixed Dimensionality. *Nano Letters* **2003**, 3 (12), 1677-1681.
176. Soloviev, V. N.; Eichhöfer, A.; Fenske, D.; Banin, U., Molecular Limit of a Bulk Semiconductor: Size Dependence of the "Band Gap" in CdSe Cluster Molecules. *Journal of the American Chemical Society* **2000**, 122 (11), 2673-2674.

177. Leung, K.; Whaley, K. B., Surface relaxation in CdSe nanocrystals. *The Journal of Chemical Physics* **1999**, *110* (22), 11012-11022.
178. Thibert, A.; Frame, F. A.; Busby, E.; Holmes, M. A.; Osterloh, F. E.; Larsen, D. S., Sequestering High-Energy Electrons to Facilitate Photocatalytic Hydrogen Generation in CdSe/CdS Nanocrystals. *The Journal of Physical Chemistry Letters* **2011**, *2* (21), 2688-2694.
179. Hewa-Kasakarage, N. N.; Kirsanova, M.; Nemchinov, A.; Schmall, N.; El-Khoury, P. Z.; Tarnovsky, A. N.; Zamkov, M., Radiative recombination of spatially extended excitons in (ZnSe/CdS)/CdS heterostructured nanorods. *J Am Chem Soc* **2009**, *131* (3), 1328-34.
180. Wei, H. H.; Evans, C. M.; Swartz, B. D.; Neukirch, A. J.; Young, J.; Prezhdo, O. V.; Krauss, T. D., Colloidal semiconductor quantum dots with tunable surface composition. *Nano Lett* **2012**, *12* (9), 4465-71.
181. Lifshitz, E.; Dag, I.; Litvin, I.; Hodes, G.; Gorer, S.; Reisfeld, R.; Zelner, M.; Minti, H., Optical properties of CdSe nanoparticle films prepared by chemical deposition and sol-gel methods. *Chemical Physics Letters* **1998**, *288* (2-4), 188-196.
182. Underwood, D. F.; Kippeny, T.; Rosenthal, S. J., Ultrafast Carrier Dynamics in CdSe Nanocrystals Determined by Femtosecond Fluorescence Upconversion Spectroscopy. *The Journal of Physical Chemistry B* **2001**, *105* (2), 436-443.
183. Pu, C.; Peng, X., To Battle Surface Traps on CdSe/CdS Core/Shell Nanocrystals: Shell Isolation versus Surface Treatment. *J Am Chem Soc* **2016**, *138* (26), 8134-42.
184. Lifshitz, E.; Dag, I.; Litvitn, I. D.; Hodes, G., Optically Detected Magnetic Resonance Study of Electron/Hole Traps on CdSe Quantum Dot Surfaces. *The Journal of Physical Chemistry B* **1998**, *102* (46), 9245-9250.
185. Zou, H.; Dong, C.; Li, S.; Im, C.; Jin, M.; Yao, S.; Cui, T.; Tian, W.; Liu, Y.; Zhang, H., Effect of Surface Trap States on Photocatalytic Activity of Semiconductor Quantum Dots. *The Journal of Physical Chemistry C* **2018**, *122* (17), 9312-9319.
186. Abdellah, M.; Karki, K. J.; Lenngren, N.; Zheng, K.; Pascher, T.; Yartsev, A.; Pullerits, T., Ultra Long-Lived Radiative Trap States in CdSe Quantum Dots. *The Journal of Physical Chemistry C* **2014**, *118* (37), 21682-21686.
187. Demortiere, A.; Leonard, D. N.; Petkov, V.; Chapman, K.; Chattopadhyay, S.; She, C.; Cullen, D. A.; Shibata, T.; Pelton, M.; Shevchenko, E. V., Strain-Driven Stacking Faults in CdSe/CdS Core/Shell Nanorods. *J Phys Chem Lett* **2018**, *9* (8), 1900-1906.
188. Gispert, J.R. (2008). *Coordination Chemistry*. WileyVCH. p. 483. ISBN3-527-31802-X.
189. Resta R. (1986) Shallow Impurity States in Semiconductors: Theoretical Aspects. In: Butcher P.N., March N.H., Tosi M.P. (eds) *Crystalline Semiconducting Materials and Devices. Physics of Solids and Liquids*. Springer, Boston, MA. https://doi.org/10.1007/978-1-4757-9900-2_6.

190. Burda, C.; El-Sayed, M. A., High-density femtosecond transient absorption spectroscopy of semiconductor nanoparticles. A tool to investigate surface quality. *Pure and Applied Chemistry* **2000**, *72* (1-2), 165-177.
191. Kodaimati, M. S.; McClelland, K. P.; He, C.; Lian, S.; Jiang, Y.; Zhang, Z.; Weiss, E. A., Viewpoint: Challenges in Colloidal Photocatalysis and Some Strategies for Addressing Them. *Inorg Chem* **2018**, *57* (7), 3659-3670.
192. Susumu, K.; Uyeda, H. T.; Medintz, I. L.; Pons, T.; Delehanty, J. B.; Mattoussi, H., Enhancing the stability and biological functionalities of quantum dots via compact multifunctional ligands. *J Am Chem Soc* **2007**, *129* (45), 13987-96.
193. Zhang, Y.; Clapp, A., Overview of stabilizing ligands for biocompatible quantum dot nanocrystals. *Sensors (Basel)* **2011**, *11* (12), 11036-55.
194. Simon, T.; Bouchonville, N.; Berr, M. J.; Vaneski, A.; Adrovic, A.; Volbers, D.; Wyrwich, R.; Doblinger, M.; Susha, A. S.; Rogach, A. L.; Jackel, F.; Stolarczyk, J. K.; Feldmann, J., Redox shuttle mechanism enhances photocatalytic H₂ generation on Ni-decorated CdS nanorods. *Nat Mater* **2014**, *13* (11), 1013-8.
195. Wolff, C. M.; Frischmann, P. D.; Schulze, M.; Bohn, B. J.; Wein, R.; Livadas, P.; Carlson, M. T.; Jäckel, F.; Feldmann, J.; Würthner, F.; Stolarczyk, J. K., All-in-one visible-light-driven water splitting by combining nanoparticulate and molecular co-catalysts on CdS nanorods. *Nature Energy* **2018**, *3* (10), 862-869.
196. Schneider, J.; Vaneski, A.; Pesch, G. R.; Susha, A. S.; Yang Teoh, W.; Rogach, A. L., Enhanced hydrogen evolution rates at high pH with a colloidal cadmium sulphide–platinum hybrid system. *APL Materials* **2014**, *2* (12), 126102.
197. Jian, J. X.; Liu, Q.; Li, Z. J.; Wang, F.; Li, X. B.; Li, C. B.; Liu, B.; Meng, Q. Y.; Chen, B.; Feng, K.; Tung, C. H.; Wu, L. Z., Chitosan confinement enhances hydrogen photogeneration from a mimic of the diiron subsite of [FeFe]-hydrogenase. *Nat Commun* **2013**, *4*, 2695.
198. Wen, M.; Li, X. B.; Jian, J. X.; Wang, X. Z.; Wu, H. L.; Chen, B.; Tung, C. H.; Wu, L. Z., Secondary coordination sphere accelerates hole transfer for enhanced hydrogen photogeneration from [FeFe]-hydrogenase mimic and CdSe QDs in water. *Sci Rep* **2016**, *6*, 29851.
199. Jian, J.-X.; Ye, C.; Wang, X.-Z.; Wen, M.; Li, Z.-J.; Li, X.-B.; Chen, B.; Tung, C.-H.; Wu, L.-Z., Comparison of H₂ photogeneration by [FeFe]-hydrogenase mimics with CdSe QDs and Ru(bpy)₃Cl₂ in aqueous solution. *Energy & Environmental Science* **2016**, *9* (6), 2083-2089.
200. Kong, D.; Cha, J. J.; Wang, H.; Lee, H. R.; Cui, Y., First-row transition metal dichalcogenide catalysts for hydrogen evolution reaction. *Energy & Environmental Science* **2013**, *6* (12).

201. Ali, M.; Zayed, D.; Ramadan, W.; Kamel, O. A.; Shehab, M.; Ebrahim, S., Synthesis, characterization and cytotoxicity of polyethylene glycol-encapsulated CdTe quantum dots. *International Nano Letters* **2019**, *9* (1), 61-71.
202. Palui, G.; Na, H. B.; Mattoussi, H., Poly(ethylene glycol)-based multidentate oligomers for biocompatible semiconductor and gold nanocrystals. *Langmuir* **2012**, *28* (5), 2761-72.
203. Susumu, K.; Mei, B. C.; Mattoussi, H., Multifunctional ligands based on dihydrolipoic acid and polyethylene glycol to promote biocompatibility of quantum dots. *Nat Protoc* **2009**, *4* (3), 424-36.
204. Liang, W. J.; Wang, F.; Wen, M.; Jian, J. X.; Wang, X. Z.; Chen, B.; Tung, C. H.; Wu, L. Z., Branched polyethylenimine improves hydrogen photoproduction from a CdSe quantum dot/[FeFe]-hydrogenase mimic system in neutral aqueous solutions. *Chemistry* **2015**, *21* (8), 3187-92.
205. Mohs, A. M.; Duan, H.; Kairdolf, B. A.; Smith, A. M.; Nie, S., Proton-Resistant Quantum Dots: Stability in Gastrointestinal Fluids and Implications for Oral Delivery of Nanoparticle Agents. *Nano Res* **2009**, *2* (6), 500-508.
206. Zhang, Y.; Liu, J. M.; Yan, X. P., Self-assembly of folate onto polyethyleneimine-coated CdS/ZnS quantum dots for targeted turn-on fluorescence imaging of folate receptor overexpressed cancer cells. *Anal Chem* **2013**, *85* (1), 228-34.
207. Smith, A. M.; Duan, H.; Rhyner, M. N.; Ruan, G.; Nie, S., A systematic examination of surface coatings on the optical and chemical properties of semiconductor quantum dots. *Phys Chem Chem Phys* **2006**, *8* (33), 3895-903.
208. Tang, H.; Zhou, C.; Wu, R.; Mao, M.; Shen, H.; Li, L. S., The enhanced fluorescence properties & colloid stability of aqueous CdSe/ZnS QDs modified with N-alkylated poly(ethyleneimine). *New Journal of Chemistry* **2015**, *39* (6), 4334-4342.
209. Zhuang, Z.; Lu, X.; Peng, Q.; Li, Y., Direct synthesis of water-soluble ultrathin CdS nanorods and reversible tuning of the solubility by alkalinity. *J Am Chem Soc* **2010**, *132* (6), 1819-21.
210. Peterson, M. D.; Cass, L. C.; Harris, R. D.; Edme, K.; Sung, K.; Weiss, E. A., The role of ligands in determining the exciton relaxation dynamics in semiconductor quantum dots. *Annu Rev Phys Chem* **2014**, *65*, 317-39.
211. Navarro, D. A.; Watson, D. F.; Aga, D. S.; Banerjee, S., Natural organic matter-mediated phase transfer of quantum dots in the aquatic environment. *Environ Sci Technol* **2009**, *43* (3), 677-82.
212. Lin-Vien, D.; Colthup, N. B.; Fateley, W. G.; Grasselli, J. G., In *The Handbook of Infrared and Raman Characteristic Frequencies of Organic Molecules*, Lin-Vien, D.; Colthup, N. B.; Fateley, W. G.; Grasselli, J. G., Eds. Academic Press: San Diego, 1991; pp 9-422.

213. Woo, W.-K. Fabrication and characterization of quantum-confined optoelectronic devices based on CdSe nanocrystals. Ph. D. Thesis, Massachusetts Institute of Technology, 2002.
214. Diroll, B. T.; Turk, M. E.; Gogotsi, N.; Murray, C. B.; Kikkawa, J. M., Ultrafast Photoluminescence from the Core and the Shell in CdSe/CdS Dot-in-Rod Heterostructures. *Chemphyschem* **2016**, *17* (5), 759-65.
215. Wang, W.; Guo, Y.; Tiede, C.; Chen, S.; Kopytynski, M.; Kong, Y.; Kulak, A.; Tomlinson, D.; Chen, R.; McPherson, M.; Zhou, D., Ultraefficient Cap-Exchange Protocol To Compact Biofunctional Quantum Dots for Sensitive Ratiometric Biosensing and Cell Imaging. *ACS Appl Mater Interfaces* **2017**, *9* (18), 15232-15244.
216. Zhou, D.; Li, Y.; Hall, E. A.; Abell, C.; Klenerman, D., A chelating dendritic ligand capped quantum dot: preparation, surface passivation, bioconjugation and specific DNA detection. *Nanoscale* **2011**, *3* (1), 201-11.
217. Morgan, D. P.; Kelley, D. F., What Does the Transient Absorption Spectrum of CdSe Quantum Dots Measure? *The Journal of Physical Chemistry C* **2020**, *124* (15), 8448-8455.
218. Liu, S.; Zhang, X.; Yu, Y.; Zou, G., A Monochromatic Electrochemiluminescence Sensing Strategy for Dopamine with Dual-Stabilizers-Capped CdSe Quantum Dots as Emitters. *Analytical Chemistry* **2014**, *86* (5), 2784-2788.
219. Liu, X.; Cheng, L.; Lei, J.; Ju, H., Dopamine detection based on its quenching effect on the anodic electrochemiluminescence of CdSe quantum dots. *Analyst* **2008**, *133* (9), 1161-3.
220. Bao, L.; Sun, L.; Zhang, Z.-L.; Jiang, P.; Wise, F. W.; Abruña, H. D.; Pang, D.-W., Energy-Level-Related Response of Cathodic Electrogenerated-Chemiluminescence of Self-Assembled CdSe/ZnS Quantum Dot Films. *The Journal of Physical Chemistry C* **2011**, *115* (38), 18822-18828.
221. Wang, J.; Han, H.; Jiang, X.; Huang, L.; Chen, L.; Li, N., Quantum dot-based near-infrared electrochemiluminescent immunosensor with gold nanoparticle-graphene nanosheet hybrids and silica nanospheres double-assisted signal amplification. *Anal Chem* **2012**, *84* (11), 4893-9.
222. Stewart, A. J.; Hendry, J.; Dennany, L., Whole Blood Electrochemiluminescent Detection of Dopamine. *Anal Chem* **2015**, *87* (23), 11847-53.
223. Freeman, R.; Bahshi, L.; Finder, T.; Gill, R.; Willner, I., Competitive analysis of saccharides or dopamine by boronic acid-functionalized CdSe-ZnS quantum dots. *Chem Commun (Camb)* **2009**, (7), 764-6.
224. Mu, Q.; Xu, H.; Li, Y.; Ma, S.; Zhong, X., Adenosine capped QDs based fluorescent sensor for detection of dopamine with high selectivity and sensitivity. *Analyst* **2014**, *139* (1), 93-8.

225. Kim, M. H.; Yoon, H.; Choi, S. H.; Zhao, F.; Kim, J.; Song, K. D.; Lee, U., Miniaturized and Wireless Optical Neurotransmitter Sensor for Real-Time Monitoring of Dopamine in the Brain. *Sensors (Basel)* **2016**, *16* (11).
226. Medintz, I. L.; Stewart, M. H.; Trammell, S. A.; Susumu, K.; Delehanty, J. B.; Mei, B. C.; Melinger, J. S.; Blanco-Canosa, J. B.; Dawson, P. E.; Mattoussi, H., Quantum-dot/dopamine bioconjugates function as redox coupled assemblies for in vitro and intracellular pH sensing. *Nat Mater* **2010**, *9* (8), 676-84.
227. Ji, X.; Palui, G.; Avellini, T.; Na, H. B.; Yi, C.; Knappenberger, K. L., Jr.; Mattoussi, H., On the pH-dependent quenching of quantum dot photoluminescence by redox active dopamine. *J Am Chem Soc* **2012**, *134* (13), 6006-17.
228. Ji, X.; Makarov, N. S.; Wang, W.; Palui, G.; Robel, I.; Mattoussi, H., Tuning the Redox Coupling between Quantum Dots and Dopamine in Hybrid Nanoscale Assemblies. *The Journal of Physical Chemistry C* **2015**, *119* (6), 3388-3399.
229. Liu, Y.; Ai, K.; Lu, L., Polydopamine and its derivative materials: synthesis and promising applications in energy, environmental, and biomedical fields. *Chem Rev* **2014**, *114* (9), 5057-115.
230. Gong, J. L.; Gong, F. C.; Kuang, Y.; Zeng, G. M.; Shen, G. L.; Yu, R. Q., Capacitive chemical sensor for fenvalerate assay based on electropolymerized molecularly imprinted polymer as the sensitive layer. *Anal Bioanal Chem* **2004**, *379* (2), 302-7.
231. Salgado, R.; del Rio, R.; del Valle, M. A.; Armijo, F., Selective electrochemical determination of dopamine, using a poly(3,4-ethylenedioxythiophene)/polydopamine hybrid film modified electrode. *Journal of Electroanalytical Chemistry* **2013**, *704*, 130-136.
232. Lee, H.; Dellatore, S. M.; Miller, W. M.; Messersmith, P. B., Mussel-inspired surface chemistry for multifunctional coatings. *Science* **2007**, *318* (5849), 426-30.
233. Zhang, C.; Ma, M. Q.; Chen, T. T.; Zhang, H.; Hu, D. F.; Wu, B. H.; Ji, J.; Xu, Z. K., Dopamine-Triggered One-Step Polymerization and Codeposition of Acrylate Monomers for Functional Coatings. *ACS Appl Mater Interfaces* **2017**, *9* (39), 34356-34366.
234. Liu, T.; Han, L.-L.; Du, C.-M.; Yu, Z.-Y., Redox potentials of dopamine and its supramolecular complex with aspartic acid. *Russian Journal of Physical Chemistry A* **2014**, *88* (7), 1085-1090.
235. Ball, V., Polydopamine films and particles with catalytic activity. *Catalysis Today* **2018**, *301*, 196-203.
236. Adel, P.; Bloh, J.; Hinrichs, D.; Kodanek, T.; Dorfs, D., Determination of all Dimensions of CdSe Seeded CdS Nanorods Solely via their UV/Vis Spectra. *Zeitschrift für Physikalische Chemie* **2017**, *231* (1), 93-106.
237. Hollett, G.; Roberts, D. S.; Sewell, M.; Wensley, E.; Wagner, J.; Murray, W.; Krotz, A.; Toth, B.; Vijayakumar, V.; Sailor, M. J., Quantum Ensembles of Silicon Nanoparticles:

Discrimination of Static and Dynamic Photoluminescence Quenching Processes. *J Phys Chem C Nanomater Interfaces* **2019**, *123* (29), 17976-17986.

238. Nighswander-Rempel, S. P., Quantum yield calculations for strongly absorbing chromophores. *J Fluoresc* **2006**, *16* (4), 483-5.

Acknowledgement

I want to say thank you to all the people who helped me in the last four years. The long race of a chasing a doctoral degree was not easy at all. I am aware that without the help from others, none of these would be possible.

I truly thank Prof. Benjamin Dietzek for giving me the opportunity to come to Germany and studied in Jena for the last four years. I really appreciate for his guidance, knowledge sharing and discussions. Although I would probably leave the academia, I will never forget you as my PhD supervisor.

I would like to give my thanks to Dr. Maria Waechtler for her help in the direction of all related work in this thesis. Without your pushing, none of this would be possible to be accomplished.

Thanks to Dr. Mathias Micheel for his kind and wise discussion in fs transient absorption spectroscopy and other areas. Thanks to Alex for the discussion on synthesis of quantum dots and NRs. Thanks to Raktim for lots of late nights that we spent in IAAC measuring lab doing measurements. Thanks to Dr. Yusen Luo, Dr. Ying Zhang, Chunyu Li and Tingxiang Yang that we spend lots of time doing discussions.

Thanks to China Scholarship Council (CSC) for financial support of my four years study.

Thanks to my parents, they must be desperate to see me after four years study in Germany.

Thanks to my girlfriend Hua Shao (Hochschule für Musik Karlsruhe) for her company and support. I was so lucky that I run into her in Frankfurt Airport and shared all these years with her.

Appendix

Table A1. Detailed fitting parameters of multi-Gaussian peaks fit of the dot-in-rod and inside-out NRs absorption spectra.

Method	Multi-Gaussian peaks fit				
		Dot-in-rod NRs		Inside-out NRs	
Adj. R-Square		0.99992		0.99998	
		Value	Standard Error	Value	Standard Error
Baseline	y_0	0.001	0.001	0.002	0.000
Peak1	Maxima	2.215	0.004	2.100	0.006
	Area	0.001	0.000	0.003	0.000
	FWHM	0.113	0.011	0.289	0.020
Peak2	Maxima	2.669	0.000	2.612	0.001
	Area	0.020	0.000	0.010	0.000
	FWHM	0.128	0.002	0.137	0.002
Peak3	Maxima	2.843	0.008	2.758	0.005
	Area	0.084	0.025	0.005	0.000
	FWHM	0.345	0.019	0.179	0.010
Peak4	Maxima	3.168	0.061	2.803	0.059
	Area	0.163	0.137	0.168	0.110
	FWHM	0.519	0.144	0.789	0.062
Peak5	Maxima	3.574	0.152	3.476	0.240
	Area	0.144	0.141	0.400	0.894
	FWHM	0.602	0.229	1.082	0.621
Peak6	Maxima	4.462	0.118	4.917	0.918
	Area	1.727	0.236	2.832	4.754
	FWHM	1.435	0.110	1.708	1.945

Table A2. Detailed fitting parameters of multi-Gaussian peaks fit on the emission spectra of the dot-in-rod and inside-out NRs. (–) indicates the missing of this component.

Method	Multi-Gaussian peaks fit				
		Dot-in-rod NRs		Inside-out NRs	
Adj. R-Square		0.9999		0.9994	
		Value	Standard Error	Value	Standard Error
Baseline	y_0	0.002	0.001	-0.059	0.076
Peak1	Maxima	2.094	0.018	1.912	0.001
	Area	0.020	0.007	0.015	0.001
	FWHM	0.170	0.011	0.063	0.002
Peak2	Maxima	2.144	0.001	1.930	0.001
	Area	0.083	0.008	0.129	0.013
	FWHM	0.127	0.002	0.151	0.005
Peak3	Maxima	2.177	0.001	2.089	0.082
	Area	0.034	0.002	0.043	0.075
	FWHM	0.086	0.001	0.398	0.351

Table A3. Fitting results of the absorption spectra of NRs with different surface ligands by seven Gaussians. Indicated are the energetic position of the peak position E_c and FWHM of the Gaussian.

Parameter	TOPO-NR	MUA-NR	HS-PEG-OCH ₃ -NR	DHLA-NRs	DHLA-PEG-NR	PEI-NR
Baseline	0.001 ± 0.001	0.014 ± 0.001	0.019 ± 0.001	0.042 ± 0.001	0.03 ± 0.001	0.016 ± 0.001
$E_{c,1}$ / eV	2.22 ± 0.01	2.24 ± 0.01	2.24 ± 0.01	2.24 ± 0.01	2.24 ± 0.01	2.25 ± 0.01
FWHM ₁ / eV	0.14 ± 0.01	0.19 ± 0.02	0.20 ± 0.02	0.17 ± 0.02	0.19 ± 0.02	0.18 ± 0.02
$E_{c,2}$ / eV	2.46 ± 0.01	2.47 ± 0.01	2.47 ± 0.01	2.46 ± 0.01	2.45 ± 0.01	2.49 ± 0.01
FWHM ₂ / eV	0.12 ± 0.03	0.13 ± 0.02	0.13 ± 0.02	0.14 ± 0.03	0.15 ± 0.02	0.11 ± 0.03
$E_{c,3}$ / eV	2.67 ± 0.01	2.68 ± 0.01	2.67 ± 0.01	2.67 ± 0.01	2.67 ± 0.01	2.70 ± 0.01
FWHM ₃ / eV	0.13 ± 0.01	0.14 ± 0.01	0.14 ± 0.01	0.14 ± 0.01	0.14 ± 0.01	0.14 ± 0.01
$E_{c,4}$ / eV	2.84 ± 0.01	2.91 ± 0.01	2.89 ± 0.01	2.90 ± 0.01	2.90 ± 0.02	2.95 ± 0.06
FWHM ₄ / eV	0.35 ± 0.03	0.40 ± 0.03	0.38 ± 0.02	0.39 ± 0.02	0.40 ± 0.03	0.45 ± 0.09
$E_{c,5}$ / eV	3.15 ± 0.15	3.24 ± 0.03	3.21 ± 0.03	3.23 ± 0.02	3.23 ± 0.02	3.31 ± 0.01
FWHM ₅ / eV	0.50 ± 0.30	0.40 ± 0.13	0.40 ± 0.11	0.37 ± 0.08	0.34 ± 0.06	0.29 ± 0.06
$E_{c,6}$ / eV	3.55 ± 0.11	3.55 ± 0.15	3.54 ± 0.16	3.53 ± 0.18	3.48 ± 0.18	3.51 ± 0.37
FWHM ₆ / eV	0.66 ± 1.11	0.69 ± 0.92	0.72 ± 0.77	0.75 ± 0.79	0.78 ± 0.80	0.76 ± 1.08
$E_{c,7}$ / eV	4.28 ± 0.10	4.34 ± 0.07	4.42 ± 0.28	4.41 ± 0.18	4.43 ± 0.22	4.37 ± 0.15
FWHM ₇ / eV	1.01 ± 1.45	1.11 ± 1.86	1.18 ± 1.89	1.22 ± 1.91	1.29 ± 1.87	1.15 ± 2.52

Table A4. Fitting results of the emission spectra of NRs with different surface ligands by three Gaussians. Indicated are the energetic position of the peak position E_{em} , amplitude A_{em} and FWHM of the Gaussian.

Parameter	TOPO-NR	MUA-NR	HS-PEG-OCH ₃ -NR	DHLA-NRs	DHLA-PEG-NR	PEI-NR
Adj. R-Square	0.99998	0.99995	0.99995	0.99990	0.99891	0.99997
Baseline	0.002 ± 0.001	0.002 ± 0.001	0.002 ± 0.001	0.002 ± 0.001	0.003 ± 0.002	0.002 ± 0.001
$E_{em,1}$ / eV	2.096 ± 0.014	2.121 ± 0.013	2.098 ± 0.051	2.088 ± 0.090	1.990 ± 0.059	2.122 ± 0.012
$A_{em,1}$	0.020 ± 0.005	0.020 ± 0.005	0.020 ± 0.021	0.016 ± 0.028	0.012 ± 0.006	0.024 ± 0.006
FWHM ₁ / eV	0.172 ± 0.008	0.171 ± 0.010	0.162 ± 0.028	0.173 ± 0.052	0.300 ± 0.002	0.185 ± 0.007
$E_{em,2}$ / eV	2.145 ± 0.001	2.162 ± 0.004	2.151 ± 0.002	2.146 ± 0.002	2.112 ± 0.001	2.165 ± 0.005
$A_{em,2}$	0.083 ± 0.007	0.066 ± 0.010	0.082 ± 0.022	0.077 ± 0.030	0.146 ± 0.007	0.060 ± 0.011
FWHM ₂ / eV	0.127 ± 0.002	0.124 ± 0.003	0.127 ± 0.005	0.133 ± 0.008	0.144 ± 0.003	0.132 ± 0.005
$E_{em,3}$ / eV	2.177 ± 0.001	2.192 ± 0.001	2.183 ± 0.001	2.184 ± 0.001	2.187 ± 0.002	2.210 ± 0.001
$A_{em,3}$	0.035 ± 0.002	0.046 ± 0.007	0.034 ± 0.003	0.046 ± 0.004	0.009 ± 0.003	0.059 ± 0.006
FWHM ₃ / eV	0.086 ± 0.001	0.091 ± 0.002	0.085 ± 0.001	0.089 ± 0.001	0.067 ± 0.007	0.094 ± 0.001

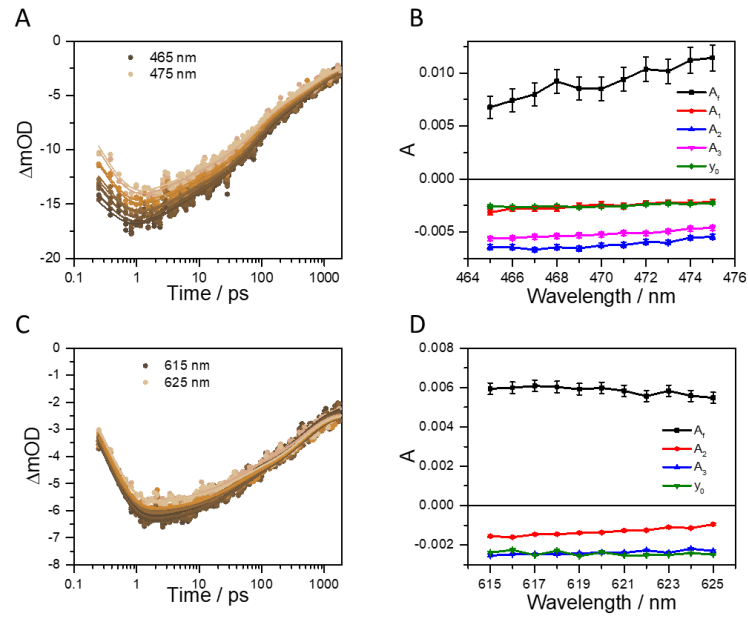


Figure A1. The global fit of the second TA measurement on the inside-out NRs (A) 10 nm scale centered at CdS bleach signal minimum 470 nm and (C) 10 nm scale centered at CdSe bleach signal minimum 620 nm. The DAS of global fit of (B) CdS and (D) CdSe parts, respectively.

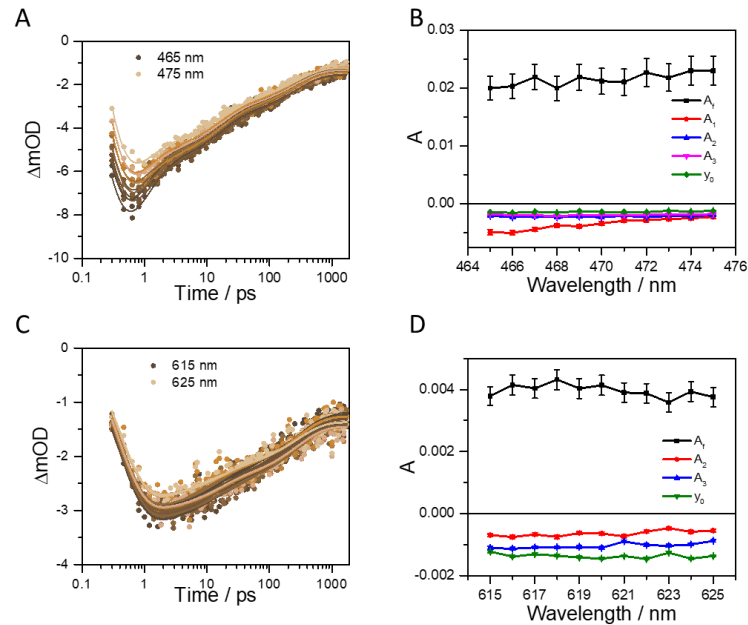


Figure A2. The global fit of the third TA measurement on the inside-out NRs (A) 10 nm scale centered at CdS bleach signal minimum 470 nm and (C) 10 nm scale centered at CdSe bleach signal minimum 620 nm. The DAS of global fit of (B) CdS and (D) CdSe parts, respectively.

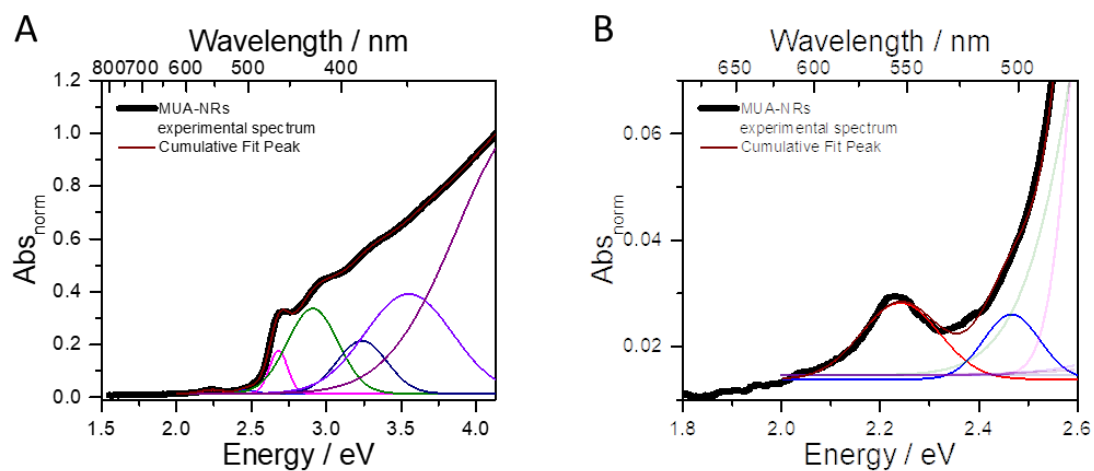


Figure A3. Multi-Gaussian peaks fit of the absorption spectrum of MUA-NRs. (A) Full wavelength range and (B) CdSe related wavelength range absorption spectra recorded in water fitted using seven Gaussians. All spectra were normalized to 1 at 4.13 eV (300 nm).

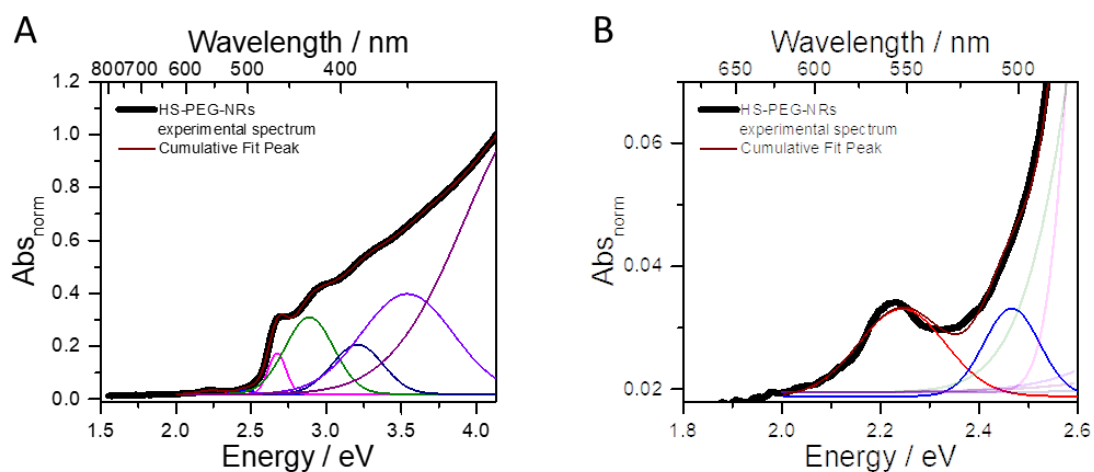


Figure A4. Multi-Gaussian peaks fit of the absorption spectrum of HS-PEG-OCH₃-NRs. (A) Full wavelength range and (B) CdSe related wavelength range absorption spectra recorded in water fitted using seven Gaussians. All spectra were normalized to 1 at 4.13 eV (300 nm).

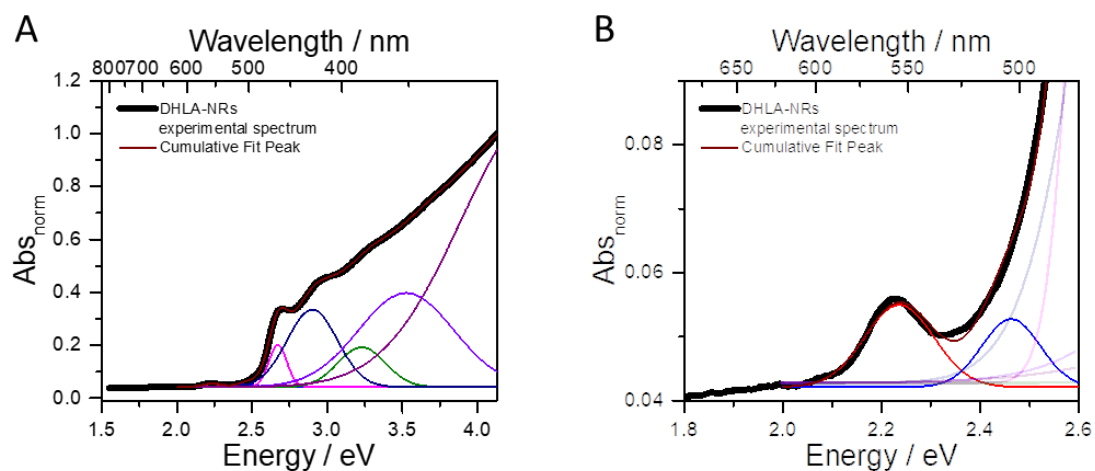


Figure A5. Multi-Gaussian peaks fit of the absorption spectrum of DHLA-NRs. (A) Full wavelength range and (B) CdSe related wavelength range absorption spectra recorded in water fitted using seven Gaussians. All spectra were normalized to 1 at 4.13 eV (300 nm).

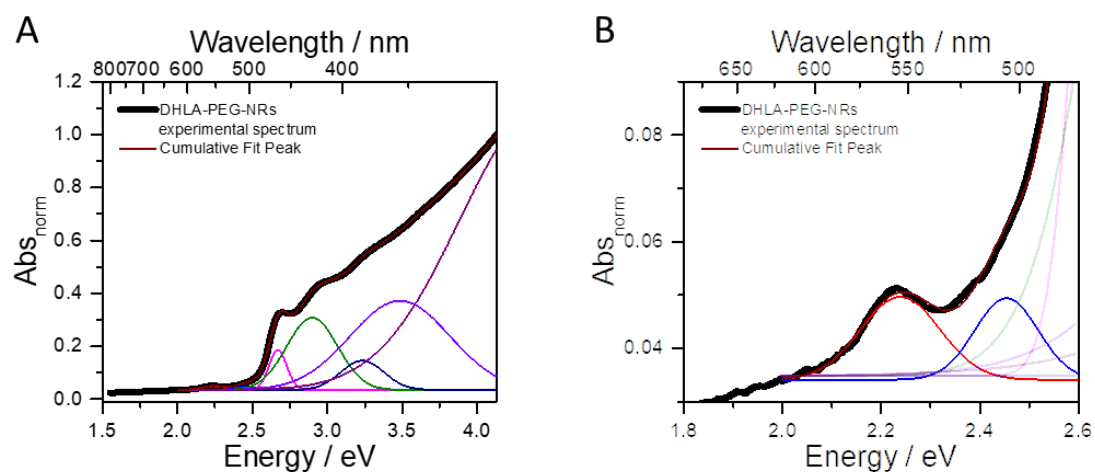


Figure A6. Multi-Gaussian peaks fit of the absorption spectrum of DHLA-PEG-NRs. (A) Full wavelength range and (B) CdSe related wavelength range absorption spectra recorded in water fitted using seven Gaussians. All spectra were normalized to 1 at 4.13 eV (300 nm).

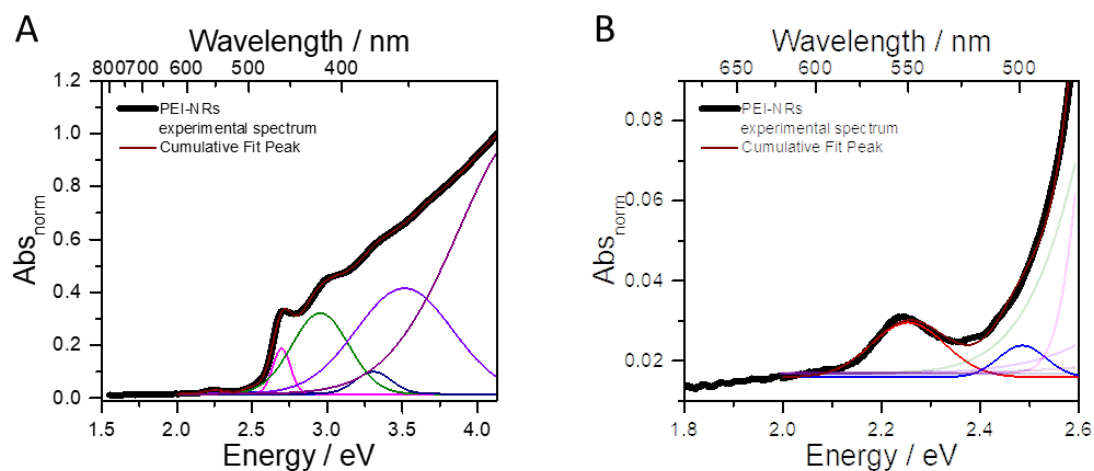


Figure A7. Multi-Gaussian peaks fit of the absorption spectrum of PEI-NRs. (A) Full wavelength range and (B) CdSe related wavelength range absorption spectra recorded in water fitted using seven Gaussians. All spectra were normalized to 1 at 4.13 eV (300 nm).

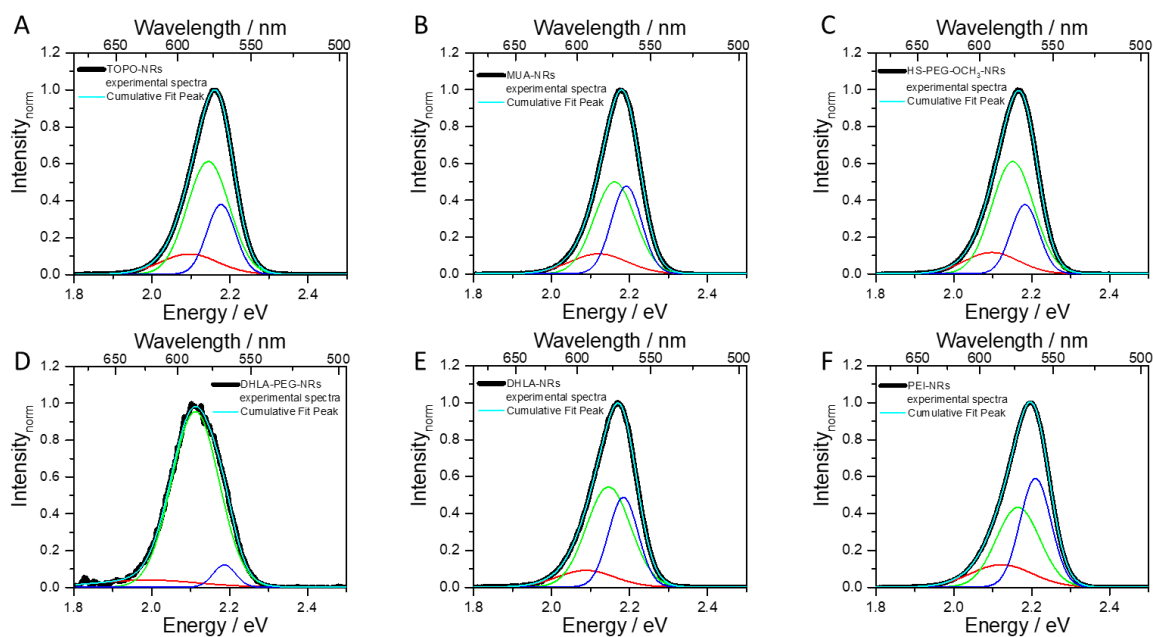


Figure A8. Multi-Gaussian peaks fit of the emission spectra of NRs with different ligands. (A) TOPO-NRs, (B) MUA-NRs, (C) DHLA-NRs, (D) DHLA-PEG-NRs, (E) HS-PEG-OCH₃-NRs and (F) PEI-NRs. Emission spectrum recorded in toluene for TOPO-NRs and in water for the rest of the NRs excited at 400 nm and fitted using three Gaussians.

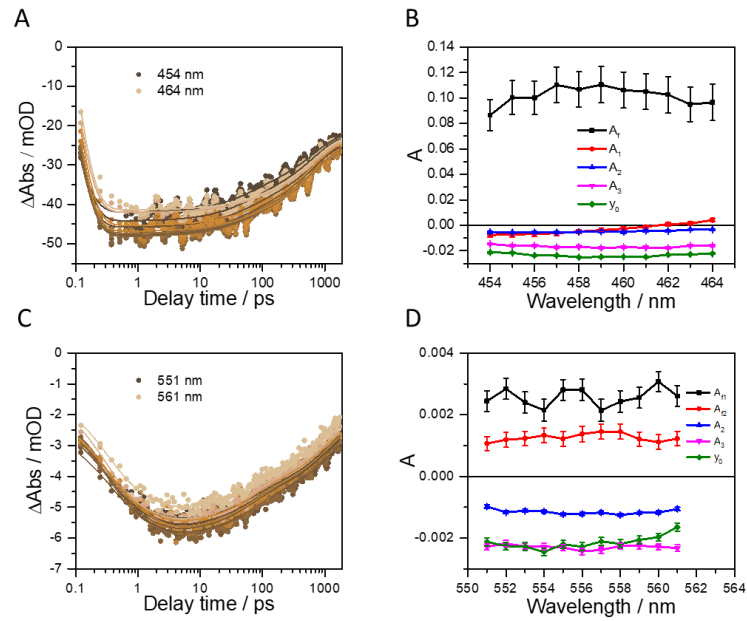


Figure A9. The global fit of MUA-NRs kinetics, (A) 10 nm scale centered at CdS bleach signal minimum 459 nm and (C) 10 nm scale centered at CdSe bleach signal minimum 556 nm. The DAS of global fit of (B) CdS and (D) CdSe parts, respectively.

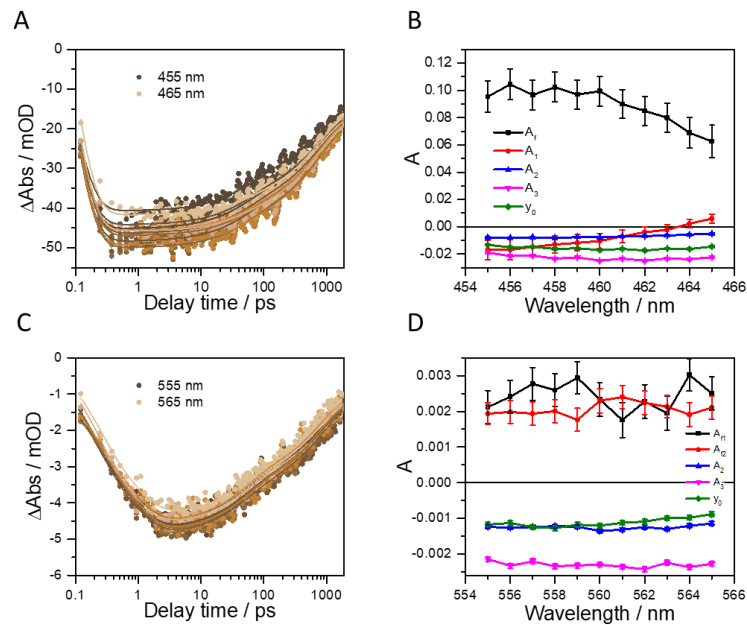


Figure A10. The global fit of HS-PEG-OCH₃-NRs kinetics, (A) 10 nm scale centered at CdS bleach signal minimum 460 nm and (C) 10 nm scale centered at CdSe bleach signal minimum 560 nm. The DAS of global fit of (B) CdS and (D) CdSe parts, respectively.

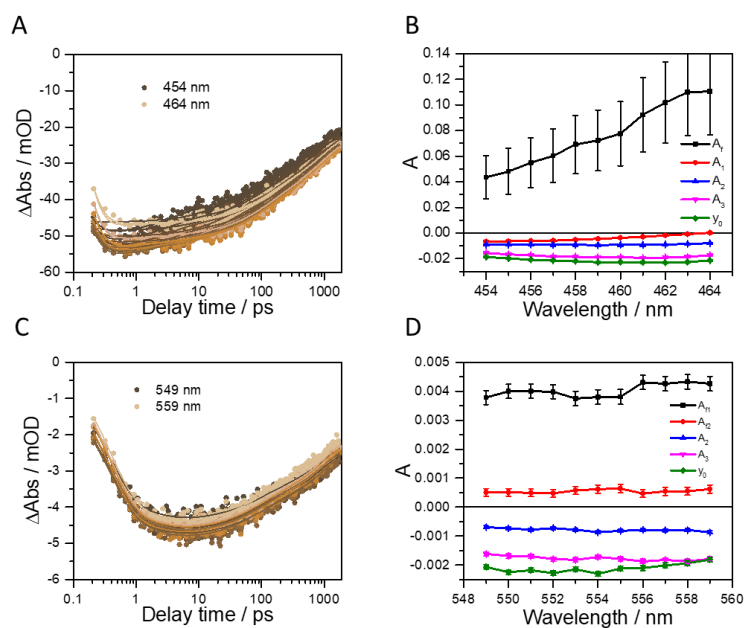


Figure A11. The global fit of DHLA-NRs kinetics, (A) 10 nm scale centered at CdS bleach signal minimum 459 nm and (C) 10 nm scale centered at CdSe bleach signal minimum 554 nm. The DAS of global fit of (B) CdS and (D) CdSe parts, respectively.

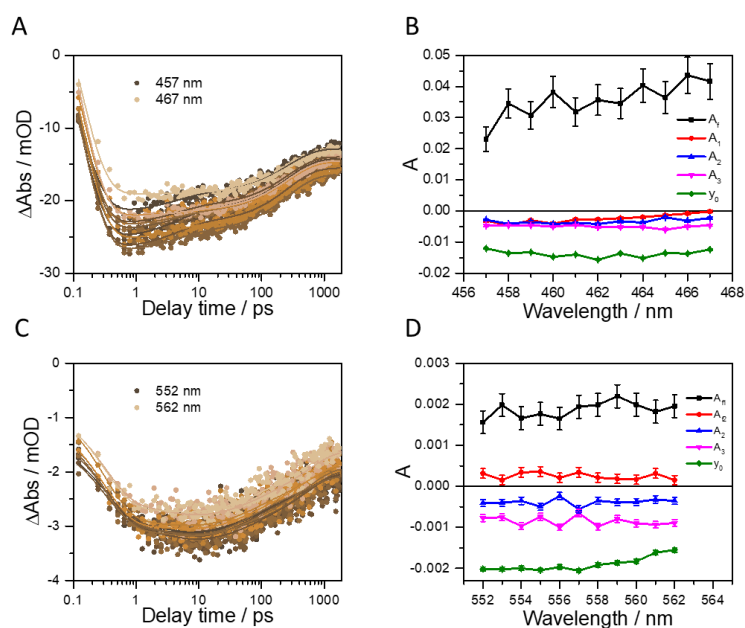


Figure A12. The global fit of DHLA-PEG-NRs kinetics, (A) 10 nm scale centered at CdS bleach signal minimum 460 nm and (C) 10 nm scale centered at CdSe bleach signal minimum 557 nm. The DAS of global fit of (B) CdS and (D) CdSe parts, respectively.

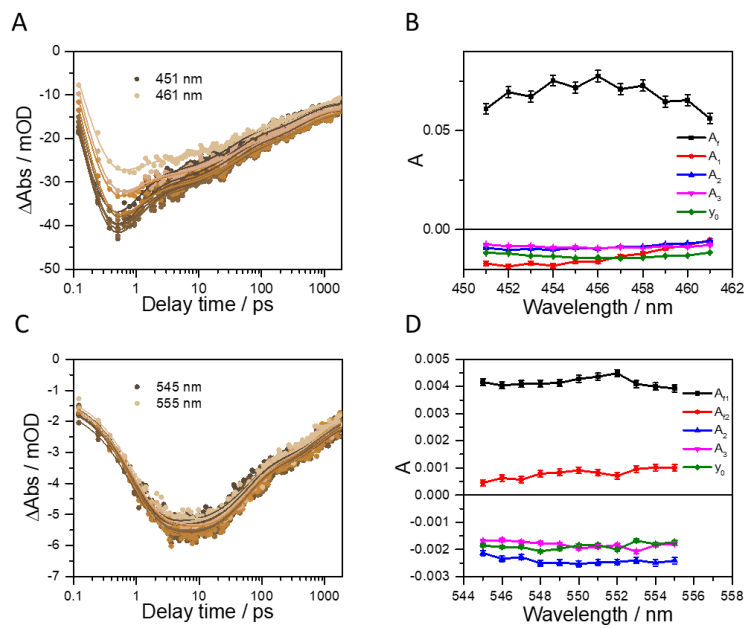


Figure A13. The global fit of PEI-NRs kinetics, (A) 10 nm scale centered at CdS bleach signal minimum 456 nm and (C) 10 nm scale centered at CdSe bleach signal minimum 550 nm. The DAS of global fit of (B) CdS and (D) CdSe parts, respectively.

Selbststaendigkeitserklaerung

Ich erkläre, dass ich die vorliegende Arbeit selbstständig und unter Verwendung der angegebenen Hilfsmittel, persönlichen Mitteilungen und Quellen angefertigt habe.

Declaration of originality

I certify that the work presented here is, to the best of my knowledge and belief, original and the result of my own investigations, except as acknowledged, and has not been submitted, either in part or whole, for a degree at this or any other university.

Bei Liu

28.09.2020

Jena

Additional information

P 63 Figure 4.11B was replaced to match the display range of Figure 4.11A. The original Figure 4.11 is displayed below.

